DOI:10.14753/SE.2023.2742

SEMMELWEIS EGYETEM

DOKTORI ISKOLA

Ph.D. értekezések

2742.

CSÁSZÁR ESZTER

Neuromorfológia és sejtbiológia
című program

Programvezető: Dr. Alpár Alán, egyetemi tanár

Témavezető: Dr. Dénes Ádám, tudományos főmunkatárs

DOI:10.14753/SE.2023.2742

Role of microglia in cerebral blood flow modulation

PhD thesis

Eszter Császár

János Szentágothai Doctoral School of Neurosciences

Semmelweis University

Supervisor: Ádám Dénes, Ph.D.

Official reviewers: Mária Deli, D.Sc.

Zoltán Jakus, Ph.D.

Head of the Complex Examination Committee: Árpád Dobolyi, D.Sc.

Members of the Complex Examination Committee: András Csillag, D.Sc.

Norbert Hájos, D.Sc.

Budapest
2022

DOI:10.14753/SE.2023.2742

Table of Contents

DOI:10.14753/SE.2023.2742

DOI:10.14753/SE.2023.2742

DOI:10.14753/SE.2023.2742

List of Abbreviations

AA	arachidonic acid
ADO	adenosine
ADP	adenosine diphosphate
AQP4	aquaporin-4
ASIC1A	acid-sensing ion channel-1A
ATP	adenosine triphosphate
AUC	area under the curve
BBB	blood-brain barrier
C1q	complement component 1q
C21	Compound 21, DREADD agonist
C3	complement component 3
cAMP	cyclic adenosine monophosphate
CBF	cerebral blood flow
CBV	cerebral blood volume
CCAo	common carotid artery occlusion
CD13	aminopeptidase N
CD200R	cluster of differentiation 200 receptor
CD47	cluster of differentiation 47
cGMP	cyclic guanosine monophosphate
CLSM	confocal laser scanning microscopy
CNS	central nervous system
CO_2	carbon dioxide
CoW	circle of Willis
COX-1	cyclooxygenase-1
CR3	complement receptor 3
CX3CL1	fractalkine
CX3CR1	fractalkine receptor
CSF-1	colony stimulating factor 1

DCZ	deschloroclozapine dihydrochloride, DREADD agonist
DREADD	designer receptor exclusively activated by designer drugs
ECM	extracellular matrix
EET	epoxyeicosatrienoic acid
EM	electron microscopy
FDG	2-deoxy-2-(18F)fluoro-D-glucose
fUS	functional ultrasound
GFAP	glial fibrillary acidic protein
GFP	green fluorescent protein
HIF1	hypoxia-inducible factor 1
hM3Dq	Gq-coupled human M3 muscarinic DREADD
HMPAO	Tc-99m hexamethylpropyleneamine oxime
HPLC	high-performance liquid chromatography
Iba1	ionized calcium binding adapter molecule 1
ICV	intracerebroventricular
IGF-1	insulin like growth factor 1
IL-1	interleukin-1
IL-1R1	interleukin 1 receptor 1
IL-1Ra	interleukin-1 receptor antagonist
IRF8	interferon regulatory factor 8
Kv2.1	potassium voltage-gated channel
L-NAME	N omega-Nitro-L-arginine methyl ester hydrochloride
LSCI	laser speckle contrast imaging
MCAO	middle cerebral artery occlusion
MIP-1	macrophage inflammatory protein-1
MMP	matrix metalloproteinase
NO	nitric oxide
NOS	nitric oxide synthase
NVC	neurovascular coupling
NVU	neurovascular unit

P2Y12	purinergic receptor P2Y12
P2Y13	purinergic receptor P2Y13
PANX1	pannexin-1
pCO_2	partial pressure of arterial carbon dioxide
PDGFR-β	platelet-derived growth factor receptor beta
PECAM-1	platelet endothelial cell adhesion molecule (CD31)
PET	positron emission tomography
PGE2	prostaglandin E2
PI3K-BDNF	phosphoinositide 3-kinase brain-derived neurotrophic factor
PLX5622	CSF1R inhibitor
pO_2	partial pressure of arterial oxygen
PVM	perivascular macrophage
RNA	ribonucleic acid
ROI	region of interest
ROS	reactive oxygen species
SMA	smooth muscle actin
SPECT	single-photon emission computed tomography
SR101	sulforhodamine 101
SUV	standard uptake value
TGF-β	transforming growth factor beta
TMX	Tamoxifen, selective estrogen receptor modulator
TNF-α	tumor necrosis factor alpha
TOM20	translocase of outer mitochondrial membrane 20
TREM2	triggering receptor expressed on myeloid cells 2
VEGF	vascular endothelial growth factor
VIP	vasoactive intestinal polypeptide
VSMC	vascular smooth muscle cell

DOI:10.14753/SE.2023.2742

1. Introduction

The brain is the most energy-demanding organ in the body, which receives about 20% of total cardiac output while it represents only 2% of body weight in adults (1, 2). In line with this, the brain consumes about 25% of whole-body glucose and 20% of whole-body oxygen uptake (2). High metabolic rates are mostly due to energy requirements of constant neural activity. Cerebral blood flow (CBF) is responsible for delivering sufficient amount of oxygen, energy metabolites and nutrients to the neural tissue and removing metabolic waste products. The average CBF is 50 ml blood per 100 g of brain tissue per minute in human adults (2). Maintaining this relatively constant blood perfusion is essential for normal brain function as the brain has no glucose storage and it is very sensitive to oxygen starvation. Hence, disturbance of blood supply lasting just a few seconds can lead to loss of consciousness, while prolonged interruption of cerebral blood flow results in severe brain damage, which occurs under pathological conditions like ischemic stroke (3). Impairment in blood supply of the brain is considered to be a key driver of various neurological conditions. The surveys of World Health Organisation show that stroke has been the second leading cause of deaths and disability worldwide for many years (4). In addition, reduction in blood flow often arises prior to symptom onset in neurodegenerative diseases such as Alzheimer disease, Parkinson's disease or Huntington's disease (5). While neurodegenerative brain diseases are leading causes of disability among elderly people, there is no effective treatment and the underlying mechanisms are still poorly understood.

Thus, it is imperative to explore the mechanisms which regulate CBF under physiological conditions and understand the processes that contribute to the development of brain diseases. My doctoral thesis intends to shed light on the importance of microglia, the main immune cells of the CNS in CBF modulation. These results may facilitate the development of novel diagnostic tools and treatment opportunities in common neurological disorders.

DOI:10.14753/SE.2023.2742

1.1. Anatomy of the cerebral vasculature

As the brain is the most energy-consuming organ in our body, it is not surprising that it is one of the most perfused organs as well. The cerebral vascular system consists of a branched network of vessels that transport blood throughout the brain. It is estimated that nearly every neuron has its own capillary in the human brain (6). The total length of capillaries is over 400 miles and the capillary surface area available for molecular traffic is about 12 m^2 in the adult human brain (7). Humans and mice have very similar vascularization patterns in the brain. Large cerebral arteries arising from the base of the brain carry oxygen-rich blood toward pial arteries on the surface of the brain within the subarachnoid space. Blood flows from pial arteries through penetrating arteries/arterioles down to the capillary level in the parenchyma of the brain (Figure 1.). While deoxygenated blood leaves the capillaries and enters the post-capillary venules, which collect the blood into venules then they travel toward the cortical surface and feed into pial veins (Figure 1.). Pial veins gather blood into large veins which connect to venous sinuses within the dura mater and transport the blood back to the heart (8).

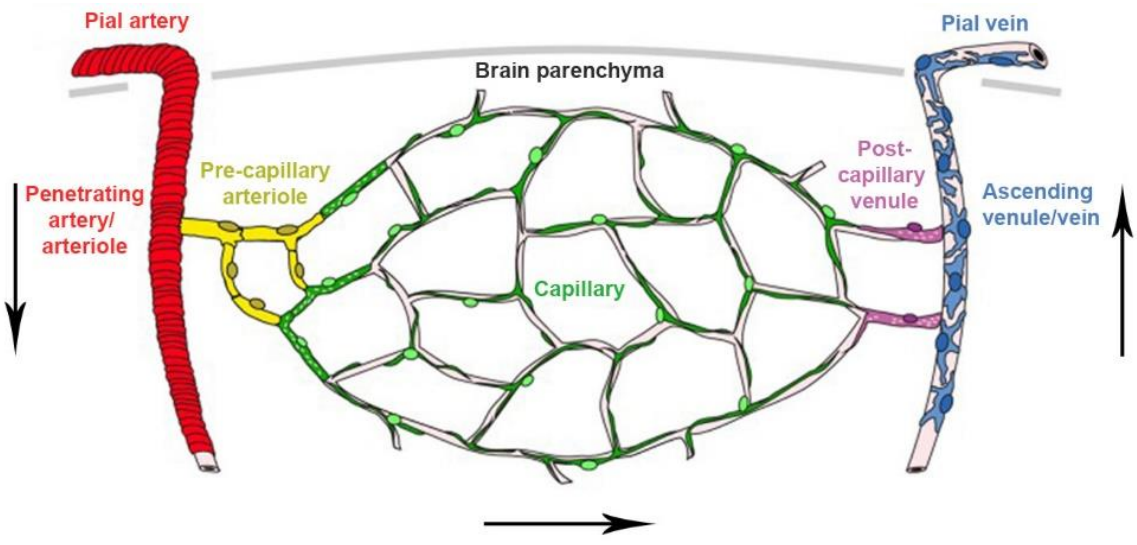

Figure 1. Vascular network of the brain. The brain-feeding arteries carry oxygen-rich blood toward pial arteries on the surface of the brain. The blood flows through penetrating arteries/arterioles down to the capillaries in the brain parenchyma, while postcapillary

venules collect deoxygenated blood into ascending venules which travel toward the cortical surface and feed into pial veins. Arrows show the direction of cerebral blood flow. Figure adopted from (9).

1.1.1. Blood supply of the brain and brain arteries

The cerebral circulation originates from the aorta. The extracranial common carotid arteries (CCAs) arise from the arch of aorta or its major branches on both side of the neck. Then CCAs divide into the external carotid arteries (ECAs) and the internal carotid arteries (ICAs). ECAs deliver blood to the neck and face, while the ICAs enter the skull through carotid canals to supply the brain (Figure 2.a). 80% of cerebral blood flow comes from the ICAs. The ICAs give off further branches responsible for the anterior circulation, these branches are the anterior cerebral artery (ACA), the middle cerebral artery (MCA) and the posterior communicating artery (PCoA). Beside the anterior circulation the brain has another large circulation, which supplies the posterior part of the brain. The posterior circulation is supplied by the vertebrobasilar system. The vertebral artery (VA) arises from the subclavian artery (SA) on each side of the neck, similarly to the ICAs they are paired arteries. The VAs fuse together to form the basilar artery, then the basilar artery divides into the two posterior cerebral arteries (PCAs), which supply the posterior part of the brain (Figure 2.a) (10). The anterior (ICAs and their branches) and the posterior circulation (VAs and their branches) are connected at the base of the skull and form the anastomotic ring termed the circle of Willis (Figure 2.b) (11).

DOI:10.14753/SE.2023.2742

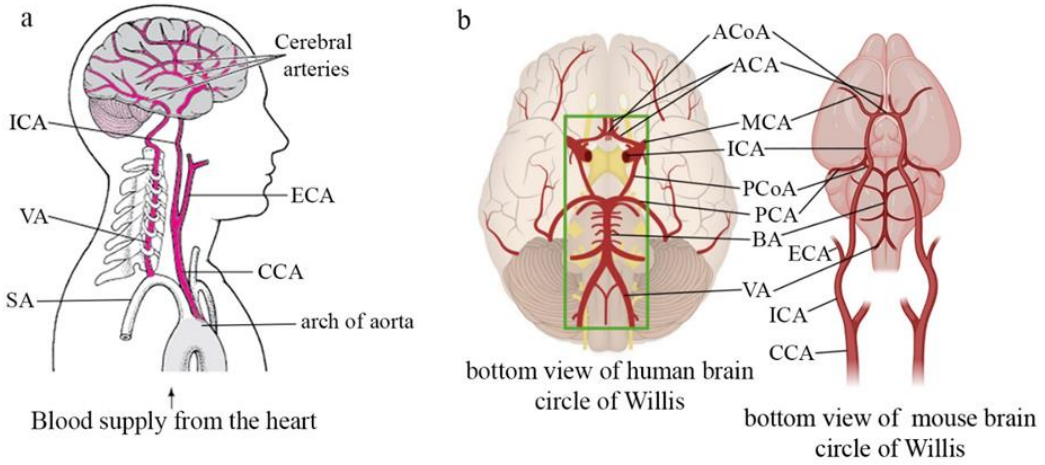

Figure 2. Origin of brain-feeding arteries in the human and the mouse brain. a) The common carotid arteries (CCAs) arising from the arch of aorta, give rise to the internal carotid arteries (ICAs) and the vertebral arteries (VAs) branching from the subclavian arteries (SAs) on both sides of the neck, supplying blood to the brain. ECA - external carotid artery. Image was adapted from (12). **b)** Circle of Willis (CoW) in human (left) and mouse (right). The components of the CoW are left and right ICAs, left and right anterior cerebral arteries (ACAs), the anterior communicating artery (ACoA), left and right posterior cerebral arteries (PCAs), left and right posterior communicating arteries (PCoAs) and the basilar artery (BA). Image on the right adapted from (13) and (14).

The circle of Willis (CoW) is the main collateral system of the brain, at first it was anatomically described by the physician Thomas Willis in Trusted Source this part of the anatomy in 1664 (15). Until 1912 there was no physiological study about the CoW. In 1912, Kramen described which brain areas are supplied by the main cerebral arteries arised from CoW by injecting methylene blue directly into the carotid or vertebral arteries and gave information about the collateral function of CoW (16).

The ACA, MCA and PCA arising from CoW responsible for the blood perfusion of the cerebrum, they supply different regions. The ACAs cover mainly the frontal and parietal lobes, the MCAs supply the majority of the lateral side of the hemispheres and the PCAs the medial and lateral parts of the temporal and occipital lobes (Figure 3.) (17).

DOI:10.14753/SE.2023.2742

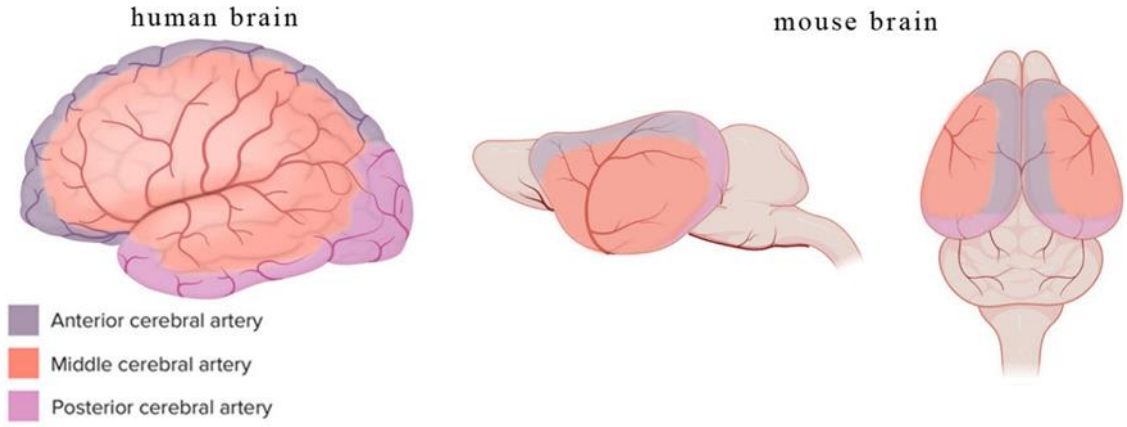

Figure 3. Arterial blood supply of the human and mouse cerebral cortex. Orange shading shows the lateral side of the brain supplied by middle cerebral artery (MCA), grey shading shows the midline area of cortex supplied by anterior cerebral artery (ACA) and purple shows the posterior part of the brain supplied by posterior cerebral artery (PCA). Images adapted from (13), (18) and (19).

The CoW is responsible for redirecting blood flow through its anterior (ACoA) and posterior communicating arteries (PCoA) from the posterior or the anterior circulation respectively, in case any of the extracranial or intracranial large arteries are blocked or constricted (10).
The branches of the ACA, MCA and PCA are connected by small pial vessels known as leptomeningeal anastomoses or pial collaterals. Pial collaterals are responsible for the redistribution of blood flow when constriction or occlusion of an artery occurs distal to the CoW (10). Although the anatomy of the collateral circulation is highly variable among individuals, it is generally effective to compensate for reduced blood flow (20).

1.1.2. The cerebral venous system

The cerebral venous system is responsible for draining deoxygenated blood from the capillary bed and transporting toward the cortical pial surface. The venules and veins of the brain run separately from the arteries and empty into the dural venous sinuses located within the subarachnoid space (21).

DOI:10.14753/SE.2023.2742

The cerebral veins can be divided into superficial and deep cerebral veins, depending on whether they drain the superficial or deep structures of the brain. The superficial venous system consists of cortical veins and empties into sagittal sinuses (Figure 4.). This system primarily drains the cerebral cortex. While the deep venous system comprises deeper cerebral veins, which feed into the transverse sinus, the straight sinus and the sigmoid sinus (Figure 4.), it drains the thalamus, hypothalamus, internal capsule, septum pellucidum, choroid plexuses, corpus striatum, and the white matter (21, 22).

The dural venous sinuses feed into the internal jugular veins as they leave the cranium and run along with the common carotid and internal carotid arteries on both sides of the neck (Figure 4.). The internal jugular vein and subclavian vein on each side of the neck join to form the brachiocephalic vein. The superior vena cava drains from the left and right brachiocephalic veins into the right atrium of the heart (23).

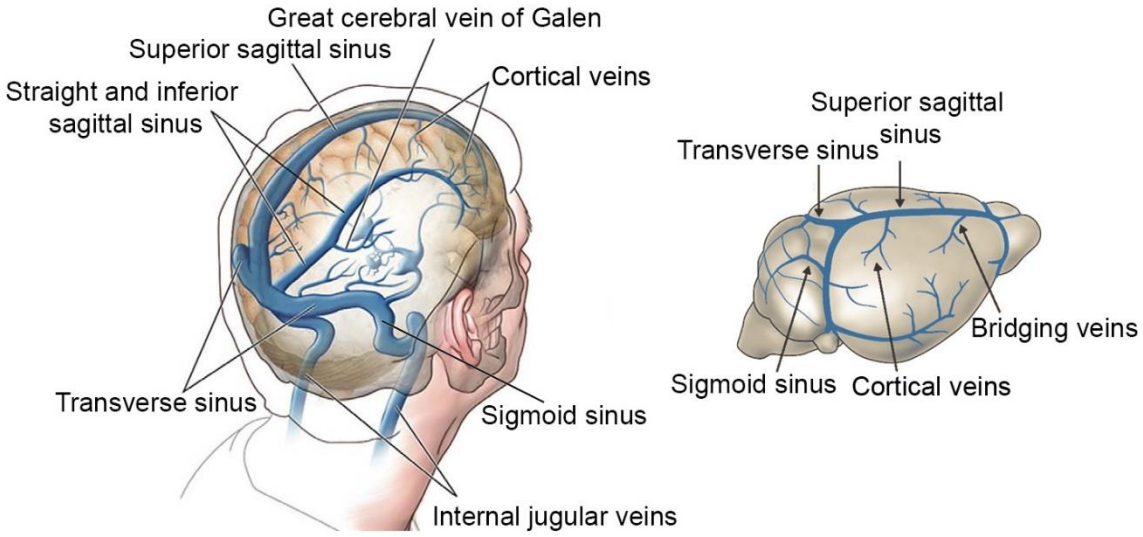

Figure 4. Venous drainage of the human and mouse brain. The superficial cerebral veins drain into the sagittal sinuses, while the deep cerebral veins feed into the transverse sinus, the straight sinus and the sigmoid sinus. The dural venous sinuses empty into the internal jugular veins on both sides of the neck. Image on the left adapted from (24) and the right image adapted from (25).

1.1.3. The neurovascular unit

The neurovascular unit (NVU) is considered as a complex anatomical and functional structure, consists of vascular cells (endothelial cells, vascular smooth muscle cells (VSMCs), pericytes), glial cells (astrocytes, microglia and other glial elements), perivascular macrophages (PVMs) and neurons. The cellular structure of the NVU changes across the cerebrovascular tree (Figure 5.) (5).

Endothelial cells form the inner monolayer of the vessel wall surrounded by the endothelial basement membrane (BM) on the abluminal side of the cells at all levels of the cerebrovascular tree. Beyond the endothelial monolayer, vascular structures differ in their cellular composition depending on their size and function. Within the subarachnoid space, the large pial arteries are covered by multiple layers of contractile VSMCs that form concentric rings around the endothelial cells. Whereas at the level of penetrating arteries/arterioles the endothelial cells are enveloped by only a single layer of contractile VSMCs. VSMCs are covered by the vascular BM and densely innervated by perivascular nerves (5). The penetrating arteries/arterioles are surrounded by a cerebrospinal fluid-filled perivascular space (Virchow-Robin space), which is a continuation of the subarachnoid space, where PVMs and other cells (fibroblasts, mast cells) are present (26). The brain parenchyma is separated from the Virchow-Robin space by the glial membrane (glia limitans), which is composed of astrocytic endfeet and the parenchymal basal lamina (27).

As penetrating arteries/arterioles reach deeper in the brain the glial membrane and the vascular BM (VSMC BM) fuse together, resulting in the disappearance of the Virchow-Robin space, thereby astrocytic endfeet come in close apposition to the VSMCs layer of arterioles. These intraparenchymal arterioles are covered by nerve terminals originating from local neurons and subcortical pathways (5).

At the capillary level, VSMCs are replaced by pericytes which are embedded into the endothelial BM ensheathing the endothelial cells. Pericytes are surrounded by astrocytic endfeet, as pericytes incompletely cover the endothelial cells, a single basement membrane is shared between astrocytes and endothelial cells named glio-endothelial BM (Figure 5.) (27). Capillaries get neuronal projections as well (5).

DOI:10.14753/SE.2023.2742

On the venous side between the glial and endothelial BM the perivascular space reappears where immune cells (PVMs, mast cells) can reside (28). Postcapillary venules are covered by mesh pericytes which are embedded into the endothelial BM, while ascending venules and veins are endowed with longitudinally oriented stellate VSMCs. Compared to arteries, veins are covered with fewer VSMCs, thus they have thinner vessel wall. Venous VSMCs morphologically, functionally and molecularly differ from arterial VSMCs (29, 30).

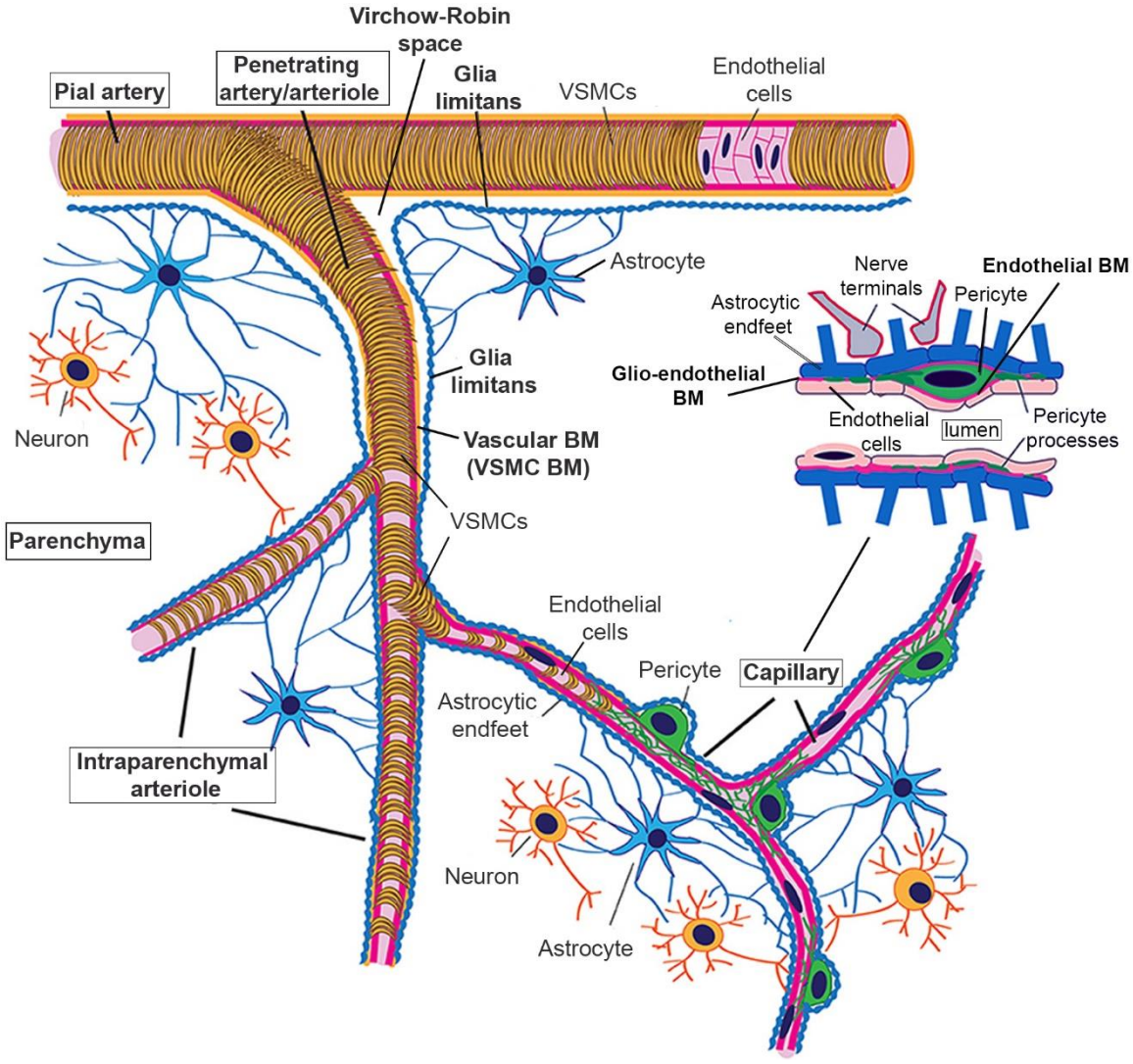

Figure 5. Simplified representation of the cerebrovascular tree showing cellular components of neurovascular unit (NVU). Large pial arteries within the subarachnoid space are enveloped by multiple layers of ring-shaped vascular smooth muscle cells

(VSMCs) which are covered by the vascular basement mebrane (BM). While penetrating arteries originating from pial arteries are endowed only one layer of VSMCs and their BM. They take place in the perivascular space (Virchow-Robin space), where perivascular macrophages (PVMs) and other immune cells reside. The brain parenchyma is disconnected from the Virchow-Robin space by the glia limitans. As penetrating arterioles dive into the brain parenchyma the glial membrane (glia limitans) and the vascular basement membrane (BM) fuse together resulting in the disappearance of the Virchow-Robin space, making the vessel wall adjacent to the astrocytic endfeet. At the level of capillaries the VSMCs are replaced by pericytes, which are embedded into the endothelial BM. Pericytes are covered by astrocytic endfeet, as the pericyte coverage of the endothelial cells is lacking, a single basement membrane is shared between astrocytes and endothelial cells named glio-endothelial basement membrane (BM). Both intraparenchymal arterioles and capillaries get neuronal projections from local neurons and subcortical pathways. Image adopted from (31).

1.2. Basic mechanisms of CBF regulation

Considering the dynamic and regionally varying energy requirements of the brain, maintenance of constant blood supply and precise, local regulation of CBF in an activity-dependent manner have to take place simultaneously. These mechanisms ensure relatively constant cerebral perfusion and compensate for fluctuations at the same time.

Control of CBF involves a wide range of complementary regulatory mechanisms including autoregulation (blood pressure), neurogenic regulation, chemical regulation (arterial blood gases (pO_2, pCO_2)) and neurovascular coupling (NVC). Besides their individual influence, there are powerful interactions between these mechanisms (32).

Since any alteration in CBF is directly, whereas resistance to CBF is inversely proportional to the fourth power of radius of blood vessels (Poiseuille's law), even small changes in vessel diameter have significant influence on CBF. Hence, acute regulation of CBF is done primarily by changing the diameter of blood vessels and thus the resistance to CBF (10). Each cerebrovascular segment has its contribution to regulating vascular resistance in the cerebral circulation. Pial arteries, penetrating arteries/arterioles and intraparenchymal

arterioles are responsible for approximately the 40% of the resistance and capillaries for about 60%, which represent their potential for CBF regulation (33).

All arterial and venous blood vessels show some degree of contraction which is relative to their maximally delated state. This phenomenon is termed vascular tone. Vascular tone is established by the balance of various vasodilator and vasonconstrictor effects acting on contractile VSMCs of arterial blood vessels thus on vessel diameter and resistance therefore CBF (34, 35).

Basal cerebrovascular tone is generated mostly by the mechanisms of cerebrovascular autoregulation, including blood pressure-induced and flow-induced myogenic (originating from contractile VSMC) responses (34). Besides that endothelial cells take part in regulation of cerebrovascular tone as well by producing vasoactive agents like nitric oxide (NO), prostaglandins, endothelium-derived hyperpolarizing factor and endothelins, which affect adjacent VSMCs (36). Furthermore, astrocytes participate in the maintanance of basal vascular tone through mediators such as adenosine triphosphate (ATP) and prostaglandins too (37). Several other factors, including neurogenic signals (38), circulating peptides or homones contribute to regulation of vascular tone (32).

In spite of these regulatory mechanisms of basal cerebrovascular tone, and owing to the lack of energy storage in the brain, increases in neuronal activity require additional increase in energy supply which is transported by a precise and highly localized increase in CBF (39). This coupling between neuronal activity and CBF, termed neurovascular coupling (NVC) or functional hyperaemia (i.e. activity-dependent increases in CBF). Besides metabolic byproducts of neuronal activity, such as adenosine, carbon dioxide (CO_2), H^+ and K^+, are able to induce vasodilation or constriction locally as well depending on the needs of the brain tissue (5). While changes in arterial blood gas tensions (pCO_2, pO_2) induce rapid CBF responses globally in the brain (40). The degree of CBF changes in response to metabolic influences is relative to the basal cerebrovascular tone.

1.2.1. Cerebrovascular autoregulation

Cerebral autoregulation is the ability of the cerebral vasculature to stabilize CBF during changes in cerebral perfusion pressure. Cerebral perfusion pressure is the difference between the mean arterial pressure and the intracranial pressure. The autoregulatory range of cerebral perfusion pressure is between 50-150 mmHg in healthy adults, within this range autoregulation is very effective and minimizes variations in CBF when perfusion pressure changes. Outside the autoregulatory range, CBF passively follows the changes of perfusion pressure, i.e. pressure-driven passive vasodilation or constriction occurs (32, 41).

The main process, which contributes to autoregulation is the myogenic reactivity of VSMCs in the vessel wall. When intravascular pressure increases, VSMCs induce vasoconstriction thus increasing vascular tone and resistance. In case intravascular pressure decreases, VSMCs cause vasodilation, decreasing vascular tone and resistance. This myogenic response is considered intrinsic to VSMCs. Since large arteries and arterioles are covered by contractile VSMCs, they account for a greater proportion of vascular resistance and contribute to maintain constant CBF (32, 41).

Autoregulation protects the brain during every day activity when changes in blood pressure occur, like physical activity and changes in posture (influence of gravity) or under pathological conditions like chronically elevated blood pressure (32).

1.2.2. Neurogenic regulation

The central nervous system can influence directly the vascular tone of cerebral vessels to control CBF. Direct interactions between nerve fibers and cerebral vessels occur both in the perivascular space and in the brain parenchyma. In addition, astrocytes often transfer signals from neurons to contractile VSMCs or pericytes (38).

Pial arteries and arterioles are abundantly innervated extrinsicly by sympathetic (42), parasympathetic and sensory (trigeminal) nerves. Within the sympathetic system, adrenergic fibers innervate large arteries releasing vasoactive neurotransmitters like epinephrine, norepinephrine, dopamine, and neuropeptide Y. In the parasympathetic system, cholinergic

fibers innervate the pial arteries producing vasodilator acetylcholine and vasoactive intestinal polypeptide (VIP), whereas the sensory nerves affect CBF through neurotransmitters like vasodilator calcitonin gene-related peptide (CGRP), substance P, and pituitary adenylate cyclase-activity peptide (PACAP). These nerves originate mainly from the superior cervical ganglia (sympathetic nerves), sphenopalatine ganglia (parasympathetic nerves) and the trigeminal ganglion (sensory nerves) (38).

In the brain tissue, intrinsic nerves also terminate on parenchymal arterioles and capillaries. These neuronal processes originate from local neurons or projections of subcortical pathways arising from the locus coeruleus, raphe, and basal forebrain (adrenergic, serotoninergic, and cholinergic projections) (38).

1.2.3. Chemical regulation

1.2.3.1. Hypoxia

Since the brain has very high metabolic demand for oxygen compared to other organs, the cerebrovasculature is very sensitive to alterations in the partial pressure of arterial O_2 (pO_2). A decrease in pO_2 (hypoxia, <50 mmHg pO_2) leads to global vasodilation in the brain, decreases in cerebrovascular resistance and increases in CBF, whereas increase in pO_2 (hyperoxia) causes vasoconstriction, increases in cerebrovascular resistance and decreases in CBF (10).

During acute hypoxia, carotid body chemoreceptors, located at the bifurcations of the CCAs on both sides of the neck and in the wall of the aortic arch, rapidly sense and respond to changes in pO_2. These chemoreceptors release neurotransmitters, which activate via the nerve of Hering the IX cranial nerve, the glossopharyngeal and sensory vagal afferents which send information to the medulla in the brainstem. Brainstem stimulus modulates sympathetic efferents to generate cardio-respiratory responses to hypoxia, such as increased respiratory rate, elevation in heart rate and regulation of CBF (43).

In the vessel lumen, red blood cells are oxygen sensors as well (40, 44). Red blood cells produce ATP in response to hypoxia (45, 46). ATP acts through signaling cascades, which

produce both neuronal and endothelial NO, adenosine and epoxyeicosatrienoic acids (EETs) (40), which induce vasodilation.

At the cellular level the transcription factor hypoxia-inducible factor 1 (HIF1) has an important role in hypoxia sensing. In the brain neurons, astrocytes, endothelial cells and myeloid cells express HIF1 in response to sustained hypoxia (lasting hours to days). HIF1 consists of two subunits HIF1α and HIF1β. HIF1β is expressed constitutively, whereas HIF1α is produced continously and accumulates in hypoxic cells but is rapidly broken down in normoxic cells. HIF1 modulates the expression of genes, which code molecules that take part in vasomotor control, angiogenesis, erythropoiesis, cell proliferation and energy metabolism (43).

Several complex mechanisms are suggested to play a role in CBF increase in response to hypoxia. The potential mechanisms of vasodilation likely vary depending on the degree and duration of exposure to hypoxia, involve interactions of physiological, metabolic and biochemical processes. Acute hypoxia increases metabolic rate, which contributes to increased CO_2 formation, elevated H^+ and lactate concentration leading to acidosis that causes cerebral vasodilation (40, 47). Both animal and human data confirm that NO is an important regulator of cerebral vasodilation in response to hypoxia (48, 49). Besides several studies have observed that hypoxia rapidly increases adenosine production locally in the brain, leading to CBF increase (50, 51).

1.2.3.2. Hypercapnia

CBF is highly sensitive to changes in pCO_2, even 1 Hgmm change in pCO_2 leading to 4% CBF alteration. An increase in the partial pressure of arterial CO_2 (pCO_2, hypercapnia) produces vasodilation, decreases cerebrovascular resistance and increases CBF, whereas decrease in pCO_2 (hypocapnia) increases cerebrovascular resistance and reduces CBF (52, 53). Sensitivity to alterations in pCO_2 can be observed at all levels of the cerebrovascular tree from large arteries, pial arteries, arterioles and intraparenchymal arterioles (32, 54, 55).

pCO_2 largely exerts its effects via changes in pH, which modulates cerebral perfusion by relaxation or constriction of smooth muscle cells in the vessel wall (56, 57). CO_2 diffusing

across the blood brain barrier (BBB) and inducing pH reduction (acidosis) in the extracellular space results in relaxation of VSMCs (57). Beside pH changes, there are other pathways involved in mechanisms of hypercapnic vasodilation. Cerebral vasodilation in response to hypercapnia is mediated partly by NO, evidenced by findings which show that in adult rats inhibition of NO synthase decreases the CBF response to hypercapnia (58, 59) and extracellular pH reduction mediated cerebral vasodilation (60). NO can be released by vascular endothelial cells, neurons and glia cells, these cell types potentially contribute to hypercapnic vasodilation (61-63). NO activates guanylate cyclase in the VSMC, leading to an increase in cyclic guanosine monophosphate (cGMP) levels, which decrease intracellular Ca^{2+} concentration in VSMCs resulting in vasodilation (61, 64, 65). A recent *in vivo* study suggested that activation of neuronal acid-sensing ion channel-1A (ASIC1A) contributes to hypercapnia-induced NO release and vasorelaxation (66).

Other *in vivo* studies revealed that cyclooxygenase-1 (COX-1) is involved in CBF increase elicited by hypercapnia (67). COX-1 is expressed continuously in most brain cells and involved in the physiological synthesis of prostanoids (68). Furthermore, astrocytic prostaglandin E_2 plays an important role in hypercapnia-evoked CBF response through COX-1 activity as well, increased pCO_2 elicit an increase in astrocytic intracellular Ca^{2+} and stimulates COX-1 which synthesizes vasodilator prostaglandin E_2 *in vivo* (69).

Adenosine, a naturally occuring purine nucleoside derived from the breakdown of ATP also takes part in controlling cerebral vasodilation in response to hypercapnia as well (64, 70).

1.2.4. Neurovascular coupling

More than a century ago, in 1890, Charles S. Roy and Charles S. Sherrington indicated the possibility, that neuronal activity causes cerebral blood flow increase (71). In the late 1970s Niels A. Lassen and his team developed methods for regional CBF measurements using radioactive tracers in the human brain demonstrating that neuronal activity causes local CBF increase (72). In the mammalian brain, CBF is tightly coupled to neuronal activity, which phenomenon is called neurovascular coupling (NVC or functional hyperaemia). NVC ensures a rapid increase in the rate of CBF and delivery of energy substrates to activated

brain areas, while clearing toxic by-products like CO_2 and heat (73). NVC can be evoked by feedback and feedforward mechanisms (Figure 6.) (5). The feedback model refers to that active neurons cause energy deficit (decreased oxygen and glucose level), which in turn induces local CBF increase in seconds (74), so the feedback mechanism driven by the metabolic state of the brain tissue (75). During neuronal activity vasoactive metabolic-byproducts are produced (adenosine, H^+, lactate, CO_2), which induce vasodilation, thus CBF increase (76-78). The feedforward mechanism concerns local CBF increase initiated by neuronal activity, which stimulates complex neurovascular signaling pathways resulting in the release of vasoactive mediators (NO, prostanoids, neurotransmitters, neuropeptides) (5, 75, 79).

The exact pathways and mechanisms which control NVC are still not fully elucidated. In the next part of my thesis I give a brief summary about the role of NVU cells in the regulation of CBF, focusing on NVC.

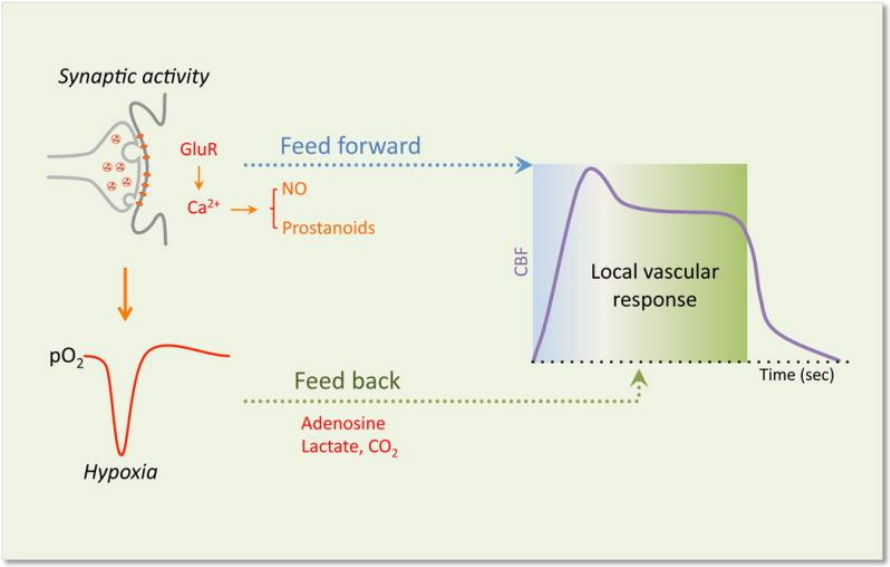

Figure 6. Neurovascular coupling (NVC) is regulated by complex feedback and feedforward mechanisms in the brain. Glutamatergic synaptic activity activates post-synaptic N-methyl-D-aspartate (NMDA) and a-amino-3-hydroxy-5- methyl-4-isoxazol epropionic acid (AMPA) receptors inducing intracellular Ca^{2+} increase resulted in nitric

oxide (NO) and prostanoid release (feedforward mechanism). Beside increased energy consumption causes releasing vasoactive metabolic-byproducts. Image adapted from (5).

1.3. The role of NVU cells in activity-dependent CBF regulation

The main cell types of the NVU known to have pivotal roles in the regulation of CBF at the level of arterioles and capillaries are endothelial cells, VSMCs, pericytes, astrocytes and neurons (Figure 7.). These cells work in concert to maintain CBF and vascular function.

It is generally accepted that NVC is initiated largely by mediators released directly by principal or interneurons in the brain parenchyma (see Neurogenic regulation and Neurovascular coupling chapter). Astrocytic endfeet directly touch arterioles and capillaries in the substance of the brain, making them well-positioned to transfer signals from neurons to the vessels, as they respond to neurotransmitters released from neurons like glutamate (80). Activation of astrocytes leads to the stimulation of various signaling pathways (Figure 7.). Astrocytic intracellular Ca^{2+} increase can activate B_K channels, producing vasodilator K^+ (81). Besides this, elevation of astrocytic intracellular Ca^{2+} leads to the release of arachinoid acid (AA) metabolites such as dilator epoxyeicosatrienoic acids (EETs) (82) and (prostaglandin E_2) PGE_2 (80) or the vasoconstrictor 20-hydroxyeicosatetraenoic acid (20-HETE) (39, 75). These mediators are known to be involved in the NVC-evoked CBF response (39, 75, 83). Astrocytes produce adenosine triphosphate (ATP), which directly causes vasoconstriction, while ATP can be metabolised by ectonucleotidases to vasodilator adenosine (84).

Mural cells of the NVU, namely VSMCs and pericytes are the executors of the dilation or constriction of blood vessels through which increase or decrease in CBF occurs. The contractile state of VSMCs and precapillary pericytes (vessel tone and resistance) depends on the changes of their membrane potential and their intracellular Ca^{2+} concentration, which are determined partly by the ion waves propagating from astrocytic endfeet (85). VSMCs around penetrating arteries/arterioles express the contractile protein α-smooth muscle actin (α-SMA), which is activated by the increase of intracellular Ca^{2+} concentrations. VSMCs clearly control CBF during neurovascular coupling and they are responsible for the

maintenance of basal vascular tone (see Cerebral autoregulation chapter) (86). At the precapillary arteriole level, α-SMA positive VSMCs are replaced by contractile pericytes, whereas at the capillary level, the expression of α-SMA abruptly decreases in pericytes (87). These capillary pericytes morphologically and transcriptionally also differ from upstream mural cells (29, 87). Many studies have not discriminated precapillary and capillary pericytes, thus the hypothesis that capillary pericytes have autonomous, active role in CBF regulation in response to increased neural activity (NVC) is highly controversial (86, 88, 89). A recent *in vivo* study, which took into consideration the heterogeneity of brain mural cells shows that capillary pericytes are contractile as well, but with much slower dynamics than upstream mural cells, suggesting that they have a role in regulation of resting, basal blood flow rather than fast NVC responses (90).

During the NVC response, endothelial cells are thought to be responsible for propragating neurovascular signals retrogradely along the vascular tree, thus controlling the spread of vasodilation or vasoconstriction (5, 91). At the capillary level, neuronal activity could directly contribute to vasodilation through the release of glutamate, acetylcholine and other neurotransmitters, or indirectly via astrocytes, VSMCs and pericytes induce a large increase in endothelial intracellular Ca^{2+} concentration. It is accomplished via opening Ca^{2+}-dependent K^+ channels, which initiate endothelial hyperpolarization (vasodilating signal) (85). Endothelial hyperpolarization can spread rapidly to neighboring endothelial cells through connexin-based gap junctions or to adjacent VSMCs via myoendothelial gap junctions (92, 93). Other endothelium-derived hyperpolarizing factors such as K^+ efflux drives signal propragation as well. VSMC hyperpolarization leads to vasorelaxation by closure of voltage-dependent calcium channels (85).

Besides, there is a slower, more spatially restricted NO/prostanoid-dependent form of propragated vasodilation (94, 95). Similarly to the fast component of signal propragation, the initial signal is the endothelial intracellular Ca^{2+} increase but with a different treshold, which induces endothelial NO/prostanoid release. These molecules diffuse to adjacent VSMCs to promote cGMP/cAMP production, which drives vasorelaxation (96).

At the level of arterioles, endothelial hyperpolarization can be initiated through activation of G-protein coupled receptors on the luminal side of vessel wall, which are sensitive to

DOI:10.14753/SE.2023.2742

neurotransmitters such as acetylcholine, adenosine, ATP, ADP, UTP, K^+ ions, and bradykinin (97). The role of these signaling pathways could be the precise control of vasodilation in upstream arterioles and arteries to generate highly localized CBF response to neuronal activity without „flow steal" from interconnected vascular areas. Overall, neuronal activity initiates the CBF increase, but the coordinated interaction of other NVU cells through the whole cerebrovascular network is essential for the implementation of the optimal CBF response.

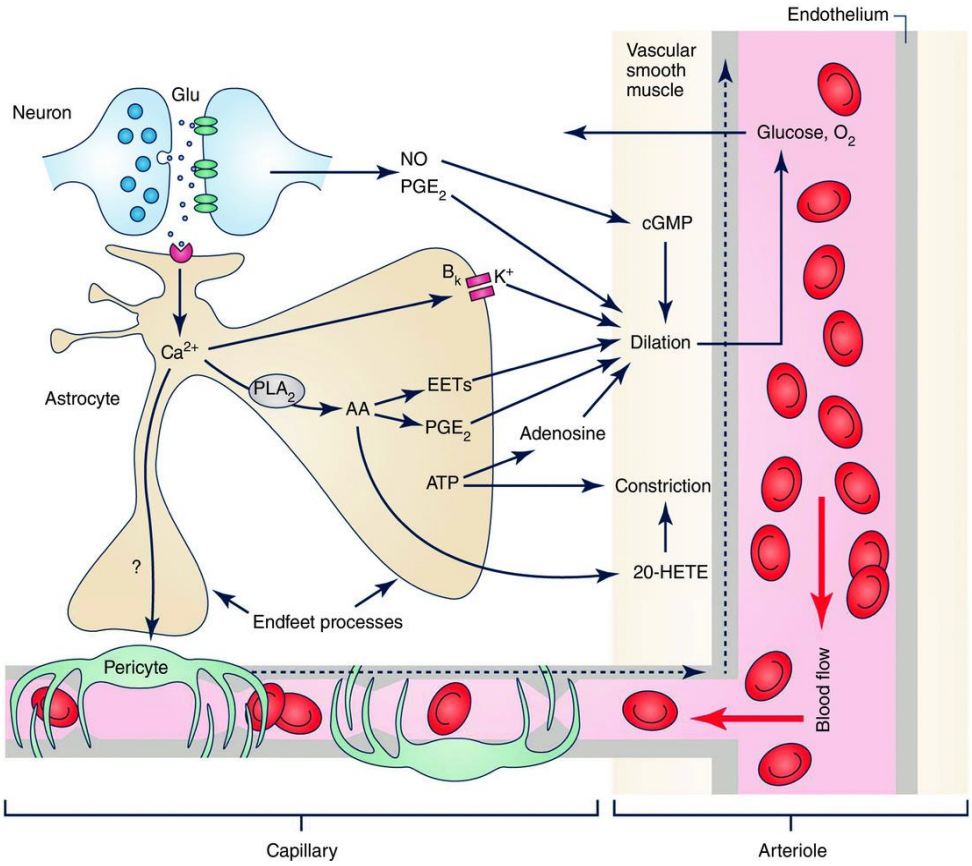

Figure 7. The main signaling pathways mediating neurovascular coupling (NVC). Neuronal activity causes the release of neurotransmitters such as glutamate, which induces the secretion of neuronal and astrocytic vasoactive mediators. Neuronal mediators like nitric oxide (NO) and prostaglandin E2 (PGE2) directly dilate cerebral arterioles, whereas astrocytes initiate a cascade of Ca^{2+}-dependent signalling pathways. Increase in astrocytic intracellular Ca^{2+} concentration results in phospholipase A2 activation, which induces the release of arachidonic acid (AA) and its metabolits including the vasodilator

epoxyeicosatrienoic acids (EETs) and PGE2. Astrocytic Ca^{2+} increase activates BK channels as well, which leads to vasodilator K^+ release. Furthermore, AA is metabolised to the vasoconstrictor 20-hydroxyeicosatetraenoic acid (20-HETE) in vascular smooth muscle cells (VSMCs) and astrocyte-derived adenosine triphosphate (ATP) can cause vasoconstriction, or its metabolite, adenosine has vasodilator effect. The release of these vasoactive mediators are leading to changes in the vascular diameter via acting on vascular smooth musle cells (VSMCs) and pericytes at the level of capillaries and arterioles, whereas endothelial cells are responsible for propagating signals along the vascular tree (dashed arrows). Image adopted from (39).

Beyond the mechanism presented above, different myeloid cell populations have also be assumed to contribute to CBF regulation. In particular, perivascular macrophages and microglia are key immunocompetent cell types of the NVU, whose roles in CBF regulation remained enigmatic to date. Therefore, the next chapters will focus on the origin and functions of brain myeloid cell types, particularly microglia, before discussing their roles in vascular processes and CBF regulation.

1.4. Origin of CNS myeolid cells and their roles in shaping vascular function and responses

The internal milieu of the central nervous system (CNS) is largely separated from the periphery by the blood-brain barrier (BBB), which protects against pathogens and circulating plasma proteins among others, while also helps to maintain precisely controlled ion gradients that are required for the operation of complex neuronal networks. Because the BBB also represents an immunological barrier preventing excessive immune surveillance by white blood cells, the brain has its own guardians, which are represented by different populations of CNS myeolid cells that occupy different parenchymal, perivascular and meningeal compartments. Non-parenchymal myeloid cells of the CNS are perivascular macrophages (PVMs), meningeal macrophages (MGMs) and choroid plexus macrophages (CPMs) that reside in the perivascular (Virchow-Robin) space along arteries and veins, in the

leptomeninges and within the choroid plexus, respectively (98). In the CNS parenchyma, microglia cells are the only resident myeloid cell population that have unique origin and roles, as discussed below (Figure 8.).

The origin of CNS myeloid cells during development have long been controversial concerning their embryonic (yolk sac) and postnatal (bone marrow) origin. Recent studies have shown that microglia originate exclusively from erythromyeloid progenitors in the embryonic yolk sac (99-101), and are not replaced by bone marrow–derived macrophages from the pheriphery, but comprise a long-lived, self-renewing population maintained by low rate clonal expansion throughout life (102-105). As such, microglial precursors reach the developing CNS in the first trimester and the number of microglia cells are stable from late postnatal stages into adulthood, which is maintained by spatial and temporal balance of proliferation and apoptosis (106).

PVMs and MGMs are also derived from embryonic yolk sac precursors like microglia, but differ from microglia in their transcriptional and proteomic fingerprints (99, 101), whereas CPMs originate partly from embryonic yolk sac precursors with constant input from developing or adult haematopoietic niches (fetal liver or bone marrow) as well (107, 108). Similarly to microglia, PVMs and MGMs are long-lived, self-renewing cells without major replacement by circulating haemopoietic stem cell-derived progenitors from the pheriphery (107), whereas CPMs are replenished via circulating progenitors mainly by monocytes rather than by-self-renewal (107, 109). The generation of both microglia and non-parenchymal macrophages (PVMs, MGMs, CPMs) is dependent on the transcription factor PU.1 and IRF8 (101, 107, 109).

Non-parenchymal macrophages are well-placed to monitor both the CNS and periheral homeostasis. Thus, these cells are involved in supporting and maintaining of BBB integrity, controling metabolic exchange with the CNS, and act as antigen presenting cells, perform phagocytosis, as well as respond to CNS and peripheral inflammation (108). PVMs surrounding penetrating arteries and veins in the perivascular space are also known to promote vascular anastomoses after occuring microlesions on cerebral vessels (110).

DOI:10.14753/SE.2023.2742

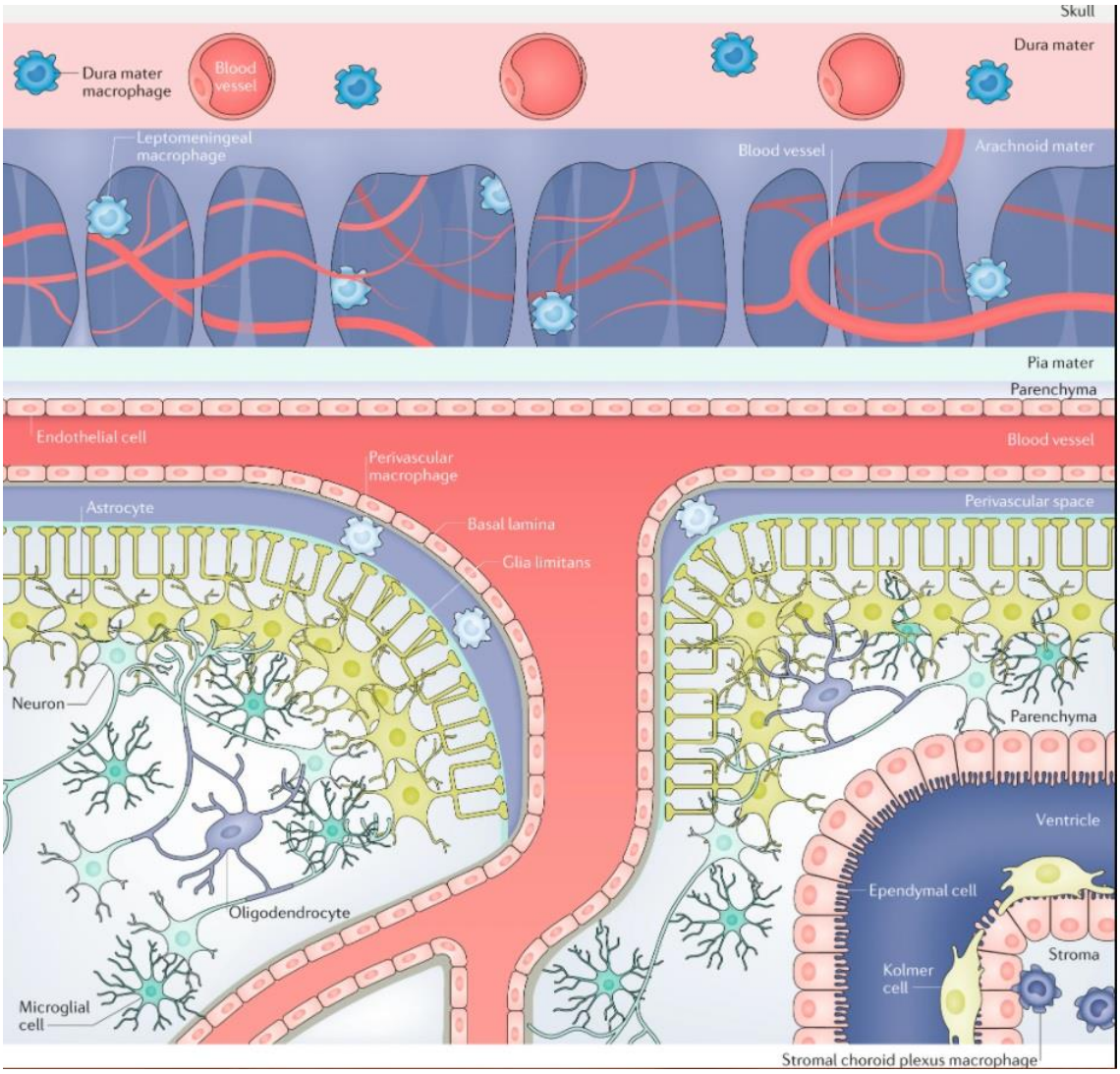

Figure 8. Myeloid guardians of the CNS. Non-parenchymal CNS myeloid cells reside at the interface of CNS as well as perivascular macrophages (PVMs) in the perivascular space (Virchow-Robin space), meningeal macrophages (MGMs) in the subdural meninges and choroid plexus macrophages (CPMs) in the choroid plexus. Whereas in the brain parenchyma the resident immune cells microglia take place. Image adopted from (98).

DOI:10.14753/SE.2023.2742

1.5. The role of microglia in the CNS

1.5.1. The role of microglia during development

During development, microglial progenitors migrate into the brain rudiment at approximately E9 in mice and from 5th gestational week in humans (99, 111). This colonization happens simultaneously with the formation of neuronal networks but before the differentation of other nervous system cells, such as astrocytes and oligodendrocytes (112). Thus, microglia are present at the right time and place to regulate neuro-, glio- and angiogenesis.

CSF-1 receptor signaling is essential for the maintenance of microglial population (113), which receptor is expressed exclusively by microglia cells in the CNS (114). Previous studies have demonstrated that CSF-1 receptor deficient mice, in which microglia are absent, show severe structural malformations in the brain, including reduced brain size, olfactory bulb atrophy, enlargement of ventricles and altered density of brain cells (114, 115). In addition, in a few cases homozygous CSF-1 receptor mutations were observed in humans. One individual showed severe developmental regression, epilepsy and leukodystrophy between 12-24 years of age. Whereas a child, who was born without microglia in his brain, developed structural abnormalities such as deformed ventricles and agenesis of corpus callosum and he died before 1 year of age (116). The developmental deficits, which occur in the absence of well-functioning microglia in the brain prove that microglia cells are crucial during CNS maturation.

Increasing evidence shows that microglia take part in coordinating the patterning and wiring of the developing CNS. Microglia have important roles in embryonic neurogenesis (117, 118), mediating axon growth (119, 120), synapse shaping (121), synapse elimination in an activity-dependent manner (122, 123), or development of cortical layers (124). Moreover, microglia are able to regulate neuronal cell numbers in the developing CNS by inducing programmed cell death and removing apoptotic neurons (108).

Besides neurons, microglia contribute to the development of other resident CNS cell types such as astrocytes, oligodendrocytes and endothelial cells of the vasculature by providing trophic support (125).

Together, these data suggest an important role for microglia in formation of new cells in the CNS during development.

1.5.2. The role of microglia in adulthood

For many years it was believed that microglia are static immune cells in the brain and become active cells only in response to brain damage or infection to defend the CNS. Since then, advanced *in vivo* imaging methods have exposed that microglia are highly active in the healthy brain, and they constantly monitor their enviroment by extending their fine processes toward cells of the CNS and cerebral vasculature (105, 126). In addition, it has been discovered that microglial cell bodies (127) migrate as well in the cerebral cortex and cerebellum (128) in healthy adult mice, although at a several orders of magnitude slower speed than seen in the case of motile processes (about 1 μm/hour and 1,5 μm/min, respectively) (126). During their surveillance, microglia are able to sense any changes or disruptions in brain homeostasis and respond to them within a short time with targeted recruitment of processes, which depending on the extent of injury, may be followed by the dislocation of their cell bodies. The migration of microglia cells is mediated mainly by extracellular ATP and its derivatives. Microglial processes are rapidly attracted towards the site of ATP release in the intact and injured brain as well (126, 129). In the healthy brain, each microglia occupies its own terrority, which does not overlap with the area of neighboring microglia cells (106), although in response to injury they often leave their terrority. There is increasing evidence that microglia play an important role in the maintenance of brain homeostasis and regulate numerous processes in the adult CNS. Microglia communicate with neurons through direct physical contact with the involvement of a variety of receptors and signaling pathways (130), which processes are crucial for the maintenance of brain homeostasis.

First of all, microglia are involved in the regulation of neurogenesis, not only during early development of the CNS but in adulthood. Adult neurogenesis (generation and integration of new neurons) is essential for the maintenance of well-functioning cognitive and memory processes in the brain (131). It has been shown that newborn neurons pass through tight

control in the healthy adult mouse brain, many of them go through apoptosis in a few hours. These dying neurons are rapidly phagocytosed by microglia, which process contributes to sustaining a well-functioning neurogenic cascade (132). Several studies have revealed that various microglial receptors are involved in the regulation of adult neurogenesis in the hippocampus, such as P2Y13 and the fractalkine receptor (CX3CR1). Disruption of P2Y13 receptor signaling pathway increases the formation of new neurons (133), whereas the pharmacological blockade of CX3CL1–CX3CR1 signaling impairs adult neurogenesis (134, 135). These findings suggest that microglia cells are highly implicated in the control of adult hippocampal neurogenesis.

In addition, microglia are able to recognise unnecessary synapses and eliminate them (122, 136). This process is termed synaptic pruning, which begins during development and occurs throughout adulthood (36, 137). Synaptic pruning supports the refinement of neuronal circuitry and increases neuronal network efficiency (138). Microglia are able to enhance or inhibit synaptic pruning through specific signaling pathways. „Eat me" signals promote microglial engulfment of inactive or injured synapses, whereas „Don't eat me" signals prevent the phagocytosis of strong and active synapses, which can contribute to learning and memory processes. Microglia express receptors which recognise these signals. Some studies demonstrated that the complement system takes part in synaptic pruning in the healthy brain, the complement proteins, C3 and C1q bind to weak synapses, which is sensed by microglial complement receptor CR3, mediating the phagocytosis of synapses (139, 140). Besides, „Eat me" signal is the CX3CR1-CX3CL1 pathway, microglial fractalkine receptor (CX3CR1) senses neuronal fractalkine (CX3CL1) molecules that recruit microglia to the synapse to eliminate it (141). Microglial TREM2 receptor is involved in synaptic pruning as well, via TREM2 receptor microglia identifies phosphatidylserine release from injured dendrites, which attract microglia to the site of the injury to engulf it (142). In contrast, neuronal CD200 and CD47 proteins are „Don't eat me" signals to microglia suggesting which synapses need to be maintained (143, 144). These studies have revealed that synaptic pruning is tightly regulated by microglia in the brain, which process is important for the regulation of neuronal activity and synaptic plasticity as well. Synaptic plasticity is the ability of CNS to strengthen or weaken synapses and neuronal connections in response to changes in synaptic activity.

Microglia are highly implicated in the modulation of synaptic plasticity (145, 146). Several mechanisms are involved in this process including CX3CR1-CX3CL1 signaling pathway (122, 145), purinergic signaling via microglial P2Y12 receptor (146), CD200R-CD200 pathway (147, 148), microglial TNF-α release (149) and microglial PI3K-BDNF signaling (150, 151), among others.

Synaptic plasticity is important for learning and memory encoding in the neuronal circuit. Involvement of microglia in learning and memory processes, including the modulation of memory strength and quality have been reported in multiple studies (140, 146, 152, 153). Overall, these above findings support important role of microglia in brain homeostasis.

1.5.3. The role of microglia in inflammation and brain diseases

Our increasing knowledge about the vital physiological roles of microglia in the developing and mature CNS proposes that disturbances in microglial functions may contribute to development of CNS diseases. In the last two decades it has become evident that microglia are highly implicated in several CNS diseases such as acute brain injuries (stroke, acute brain trauma), brain infections (causative pathogens: virus, bacteria, parasite, fungus or prion), chronic neurodegenerative disorders (Alzheimer's disease, Parkinson's disease, Huntington's disease, multiple sclerosis) and psychiatric diseases like schizophrenia, bipolar disorders and depression (154-159). Increasing evidence demonstrates that inflammation in the CNS typically occurs in all major brain diseases (159-161). However it has remained largely controversial to what extent inflammation is causative or a consequence of the diseases progression in given disorders. It has been revealed that microglia, the resident immune cells of the brain, are key players in the regulation of central inflammatory responses to acute and chronic brain disorders. In response to acute neuronal injury or infection, microglia become activated within a few minutes, which rapidly triggers changes in microglial morphology, phenotype and function. Microglial activation is complex and dynamic, microglia can adopt various phenotypes that may be characterized with the dominance of pro- or anti-inflammatory states, which affect the outcomes of CNS inflammation (162, 163). Microglial responses may include changes in the expression of cell

surface activity markers, the process of pathogen recognition, phagocytosis of pathogens and dying cells, recruiting other immune cells from the blood, releasing a large array of pro-inflammatory mediators such as cytokines (IL-6, IL-23, IL-1, TNF-α), chemokines (MIP-1, CX3CL1), proteases (matrix metalloproteases, MMPs), and free radicals (164, 165) among others. When the pro-inflammatory response to the injury or infection is sufficient, microglia may transform into a less proinflammatory state, during which microglia support tissue repair, engulf apoptopic debris, suppress inflammatory responses and release anti-inflammatory mediators such as TGF-β and IL-10 (166).

In several brain diseases chronic microglial activation occurs, which leads to constantly elevated inflammatory burden. Primed microglia may produce an exaggerated inflammatory response to a second neuronal injury, which results in development of cognitive deficits, impaired synaptic plasticity and accelerated neurodegeneration (165, 167). In addition, microglial activation has been demonstrated in the developing brain in response to maternal inflammation, which influences the process of neurogenesis, neuronal patterning, synaptic pruning thereby contribute to the development of brain disorders such as autism, Rett syndrome and schizophrenia (168, 169).

Besides, a large number of systemic and other factors including sex, genetic background, microbiome composition, enviromental exposures, systemic inflammation, infections and aging also affect the function and transcriptional profiles of microglia. Each of these factors contribute to generate diverse microglia states, which affect the course of brain diseases and response to theraphy (170).

Microglia have different pro- and anti-inflammatory profiles in various brain diseases, each of which is regulated by a unique set of transcriptional factors and express partially distinct cell surface markers. The precise phenotypic characterization of disease-specific microglia states is key in understanding their contribution to brain disorders. Developing technologies further such as single-cell RNA sequencing and GWAS (Genome-wide association studies) can allow a more detailed charaterization of microglia states, supporting the development of novel diagnostic and therapeutic approches, to eventually target specific subgroup(s) of microglia (171-173).

1.6. Interactions between microglia and blood vessels, BBB function and other vascular processes

It has been long recognized that microglia directly interact with the cerebral vasculature in the healthy adult brain (105, 174-176), however the precise role of these microglia-vascular interactions have not been elucidated yet. More research has been done to understand the function of these interactions in the developing brain and in the context of various brain diseases such as brain tumors, acute brain injuries (ischemic stroke, traumatic brain injury) and chronic neurodegenerative diseases (Alzheimer's disease, Parkinson's disease and multiple sclerosis) (105, 175).

During development, microglia reside in the close vicinity of blood vessels (177), moreover it was noticed that microglia migrate along cerebral blood vessels while they are colonizing the brain (105, 178, 179). Although, the precise function of this migration along blood vessels is not clear. Increasing evidence reveals that microglia play an important role in angiogenesis. *In vitro* and *in vivo* data has suggested that microglia are essential for vascular branching in the embryonic retina and hindbrain (180-182). Moreover, in mice and zebrafish a decrease in microglia number leads to reduction in the number of vascular branching points (182). In addition, it has been shown that microglia guide the sprouting vessel tip mainly via vascular endothelial growth factor (VEGF) dependent mechanisms in fetal brain (182). Furthermore, damaged PU.1 signaling in microglia causes disrupted vasculature in the CNS (182). Both disrupted VEGF and PU.1 signaling in microglia lead to embryonic lethality (182-184).

In the last two decades it has been revealed that cerebrovascular inflammation along with BBB dysfunction are major contributors to brain diseases. Microglia-mediated processes are highly implicated in regulation of vascular inflammation and BBB function (185). During their surveillance activity, microglia continuously communicate with the cells that regulate BBB function, thus microglia are assumed to rapidly initiate changes in BBB function and respond to BBB dysruption. It has been shown that microglial processes are recruited to sites of BBB leakage within minutes to restore vascular integrity (186-188). In addition, our *in vivo* two-photon imaging study has shown that microglia migrate to the vessel wall even before the BBB disruption (176).

In acute brain disorders like ischemic stroke, disruption of the BBB is secondary to the initial brain damage. In response to injury, microglia become more reactive and may contribute to vascular inflammation and BBB disruption by releasing inflammatory molecules such as MMPs, IL-1, TNF-α and ROS (189-192). Microglial IL-1β, the most studied member of the IL-1 family, is the main inducer of inflammation and BBB disruption. IL-1β activates endothelial IL-1R1 (IL-1 receptor 1) which leads to increased BBB permeability (193). *In vitro* data suggest that microglia-derived TNF-α has similar effect on BBB, it binds to its endothelial receptor inducing downregulation of tight junction proteins, which results in leaky BBB (194, 195). It has been revealed that microglia-derived MMP9 contributes to BBB damage in Alzheimer's disease (196). During the later stages of brain injury, microglia may take part in BBB repair and postinjury angiogenesis through the release of mediators such as IGF-1, ephrin and IL-1α (102, 197, 198).

In several brain disorders, BBB disruption occurs before the onset of neuronal injury and microglia activation. Based on our present knowledge, endothelial cells are highly implicated in inducing changes microglial reactivity by releasing various mediators under pathological condition. For expamle, endothelium-derived mediators MMP3, CX3CL1, NO and CD200 molecules are known to influence microglial activity (110, 199-201). Besides, it has been demonstrated that VEGF release from endothelial cells attracts microglia to perivascular amyloid-β deposits in Alzheimer's disease (202). In addition, pericytes are involved in regulation of microglia activation as well by releasing inflammatory mediators such as IL-6 and MIP-1α (192). Furthermore, the extracellular matrix (ECM), which is the major component of the BBB basement membranes, has important role in regulation of microglial function. As the result of BBB damage, ECM proteins such as fibronectin, vitronectin become free in several acute neuropathologies like cerebral ischemia (203), and may induce additional microglial inflammatory responses.

Overall, the above findings support the important role of microglia-vascular interactions in the brain. Thus, understanding their function under physiological and pathological conditions is crucial, which may provide novel treatment opportunities in common cerebrovascular diseases.

DOI:10.14753/SE.2023.2742

2. Objectives

Microglia are the main immune cells of the brain, which play an important role in various physiological and pathological processes. Microglia-mediated actions are highly implicated in the regulation of vascular inflammation and BBB function, which occur in common brain diseases, such as stroke, acute brain injury and chronic neurodegenerative diseases. Beside inflammation, impairment in blood supply of the brain is considered as a key driver of common brain diseases. The underlying mechanisms, which contribute to the development and progression of brain disorders, are still poorly understood. Therefore, it is crucial to explore the mechanisms, which regulate CBF under physiological and pathological conditions. Thus, the main goal of my work is to elucidate the importance of microglia in CBF regulation under physiological conditions and in the context of hypoperfusion, focusing on the following four main topic:

1) To identify the role of microglia in activity-dependent CBF regulation.

2) To study the role of microglia in regulation of CBF response to hypercapnia.

3) To explore the microglial actions in cerebrovascular adaptation to reduced cortical perfusion after common carotid artery occlusion.

4) To identify the mechanisms through which microglia mediate alterations in CBF.

3. Materials and methods

3.1. Mice

Experiments were performed on 11-17 weeks old male C57BL/6J (RRID:IMSR_JAX:000664), P2Y12R$^{-/-}$ (B6;129-P2ry12^{tm1Dgen}/H P2Y12R KO), CX3CR1$^{GFP/+}$ (RRID:IMSR_JAX:005582), CX3CR1$^{GFP/+}$/P2Y12$^{-/-}$, CX3CR1$^{GFP/GFP}$, CX3CR1^{tdTomato}, and Thy1-GCaMP6s (C57BL/6J-Tg(Thy1-GCaMP6s)GP4.12Dkim/J, RRID:IMSR_JAX:025776) (204), MicroDREADD^{Dq}, CX3CR1$^{CGaMP5g\text{-}tdTomato}$ (RRID:IMSR_JAX:024477), MicroDREADD^{Dq} x CGaMP5g-tdTomato mice, IL-1R1$^{fl/fl}$ and IL-1R1$^{fl/fl\ \Delta\ Slco1c1}$ (all on C57BL/6J background). Mice were kept in a 12h dark/light cycle environment, under controlled temperature and humidity with food and water ad libitum. All experimental procedures were in accordance with the guidelines set by the European Communities Council Directive (86/609 EEC) and the Hungarian Act of Animal Care and Experimentation (1998; XXVIII, Sect. 243/1998), approved by the Animal Care and Experimentation Committee of the Institute of Experimental Medicine and the Government Office of Pest County Department of Food Chain Safety, Veterinary Office, Plant Protection and Soil Conservation Budapest, Hungary under the numbers PE/EA/1021- 7/2019, PE/EA/673-7/2019 and Department of Food Chain Safety and Animal Health Directorate of Csongrád Country, Hungary. Experiments were performed according to the EU Directive 2010/63/EU on the protection of animals used for scientific purposes, and reported in compliance with the ARRIVE guidelines.

Generation of CX3CR1^{tdTomato}, MicroDREADD^{Dq}, MicroDREADD^{Dq} x CGaMP5g-tdTomato and CX3CR1$^{CGaMP5g\text{-}tdTomato}$ mice

CX3CR1^{tdTomato}, MicroDREADD^{Dq}, CX3CR1$^{CGaMP5g\text{-}tdTomato}$ and MicroDREADD^{Dq} x CGaMP5g-tdTomato mice were generated by crossing tamoxifen-inducible CX3CR1^{CreERT2} mice (B6.129P2(C)-CX3CR1$^{tm2.1(cre/ERT2)Jung/J}$, RRID:IMSR_JAX:020940 (205) either with a cre-dependent tdTomato (B6;129S6-Gt(ROSA)26Sortm9(CAG-tdTomato)Hze/J, RRID:IMSR_JAX:007905), or with a hM3Dq DREADD (B6N;129-Tg(CAG-CHRM3*,-mCitrine)1Ute/J (206), RRID:IMSR_JAX:026220), or with a CGaMP5g-tdTomato-expressing mouse line (B6;129S6-*Polr2a*$^{Tn(pb\text{-}CAG\text{-}GCaMP5g,\text{-}tdTomato)Tvrd}$/J (207),

RRID:IMSR_JAX:024477). To induce tdTomato, hM3Dq DREADD or CGaMP5g-tdTomato expression in microglia, Cre recombinase activity was induced by two intraperitoneal injections of tamoxifen (TMX, 2mg/100µl, #T5648, Sigma, dissolved in corn oil), 48h apart in 3-4 weeks old male mice, shortly after weaning. Four weeks after TMX induction, 95.3% of microglia expressed hM3Dq receptors as confirmed by anti-GFP (goat anti-GFP antibody, 1:300, #600-101-215, Rockland) and anti-P2Y12R immunostaining, to detect mCitrine and microglia, respectively (206). Using CX3CR1^{CreERT2} mice, microglia show constant cre-dependent expression, while most peripheral macrophages/monocytes expressing CX3CR1 are replaced by the end of the 4th week after TMX induction, due to their rapid turnover (205). Therefore all experiments were carried out between the 11th and the 12th weeks of age. Microglial responses were modulated in real time either by intraperitoneal clozapine-N-oxide (CNO, i.p. 0.5 mg/kg, #4936, Bio-Techne Corp.) or deschloroclozapine (DCZ, i.p. 1µg/kg #HB9126, HelloBio) administration, via the activation of hM3Dq DREADD (208).

Generation and characterization of CX3CR1^{tdTomato} microglia reporter mice

CX3CR1^{tdTomato} mice were generated by crossing tamoxifen-inducible CX3CR1^{CreERT2} mice (B6.129P2(C)-CX3CR1$^{tm2.1(cre/ERT2)Jung/J}$, RRID:IMSR_JAX:020940 (205) with a cre-dependent tdTomato-expressing line (B6;129S6-Gt(ROSA)26Sortm9(CAG-tdTomato)Hze/J, RRID:IMSR_JAX:007905). To induce tdTomato expression in microglia, Cre recombinase activity was induced by two intraperitoneal injections of tamoxifen (TMX, 2mg/100µl, #T5648, Sigma, dissolved in corn oil), 48h apart in 3-4 weeks old male mice, shortly after weaning. Four weeks after TMX induction, virtually 100% of tdTomato expressing cells were identified as microglia, as assessed by P2Y12 and Iba1 immunostaining - tdTomato-positive cell bodies and processes were analyzed in the somatosensory cortex on high-resolution CLSM stacks (CFI Plan Apochromat VC 60XH oil immersion objective, 0.1µm/pixel, Z-step: 2 µm) with homogenous sampling (209).

Generation of IL-1R1$^{fl/fl\,\Delta\,Slco1c1}$ mouse line

Brain endothelial-specific IL-1R1 knockout (KO) mice were generated by crossing mice in which exon 5 of the *Il1r1* gene is flanked with loxP sites [IL-1R1 floxed ($^{fl/fl}$)] (86) with mice expressing Cre recombinase under the promoter of the thyroxine transporter (Slco1c1) that is specifically expressed in brain endothelial cells (210) (thereafter named IL-1R1$^{fl/fl\,\Delta\,Slco1c1}$). Brain endothelial IL-1R1 deletion was achieved by injection of tamoxifen (2 mg/100 µl in corn oil, Sigma-Aldrich) for five consecutive days in 6–9 week old male mice. Controls were IL-1R1$^{fl/fl}$ male mice injected with tamoxifen. Mice allocated for the detection of IL-1R1 expression were culled 0, 7 and 14 days after tamoxifen administration (211), whilst mice allocated for experimental stroke underwent surgery at 21 days after the start of tamoxifen administration. n=11 IL-1R1$^{fl/fl\,\Delta\,Slco1c1}$ animals injected with tamoxifen and n=11 IL-1R1$^{fl/fl}$ animals injected with tamoxifen, were used in this study to determine the effect of brain endothelial cell IL-1R1 deletion.

3.2. *In vivo* experiments

***In vivo* two-photon imaging**

CX3CR1$^{GFP/+}$, CX3CR1^{tdTomato}, CX3CR1$^{GFP/+}$ x P2Y12$^{-/-}$ or Thy1-GCaMP6s mice were anaesthesized using 1,8% isoflurane or fentanyl (0.05mg/kg) and a 3 mm diameter cranial window was opened on the left hemisphere, above the primary somatosensory or the barrel cortex without damaging the dura mater. After removal of the skull bone, double circular glass coverslip was fixed with 3M^{TM} Vetbond^{TM}. Above the dual coverslip, a custom-made metal headpiece (Femtonics Ltd., Budapest, Hungary) was fixed with dental cement. Three weeks after cranial window surgery, microglia-vascular interactions in response to 3x CCAo or hypercapnia (ketamine-medetomidine anesthesia, i.p. 30mg/kg-0.1mg/kg), and neuronal $[Ca^{2+}]_i$ in response to whisker stimulations (in ketamine-medetomidine anaesthesia) were imaged in body-temperature controlled animals. To image microglia vascular interaction, blood vessels were labeled either with Rhodamine B-Dextran (70000 mol wt, neutral, #D1841, Molecular Probes) or with FITC-Dextran (70000 mol wt, #53471, Sigma) injected into the retro-orbital sinus or into to the tail vein. Two-photon imaging was performed with a Femto2D-DualScanhead microscope (Femtonics Ltd., Budapest, Hungary) coupled with

Chameleon Discovery laser (Coherent, Santa Clara, USA). The measurements were done either with the 920 nm tunable or with 1040 nm fixed wavelength laser excitation to simultaneously record GFP and Rhodamine B-Dextran signal as well as tdTomato and FITC-Dextran signal *in vivo* in real time. For microglia process motility measurements in response to 3x CCAo, the galvo-scanning light path with 16x water immersion objective (Nikon CFI75 LWD 16x W, NA 0.8) was used to acquire 4 images Z-stacks with 8.5 μm step size, 150-200 μm below the dura, at 500 x 500 pixel resolution. For measuring vascular responses to hypercapnia, a mild ketamine-medetomidine sedation (i.p. 30 mg/kg-0.1 mg/kg) was used. After obtaining 1 min baseline, a 2 min hypercapnic episode (inhaling a 10 % CO_2-containing air mixture) and 1 min post-hypercapnic period were imaged with the resonant light path at 32.7521 Hz. For *in vivo* $[Ca^{2+}]_i$ imaging in control and microglia-depleted Thy1-GCaMP6s mice, three weeks after cranial window surgery the right whiskers were stimulated with a bending actuator (#PL112-PL140 PICMA Bender) connected to a piezo amplifier (#E-650 Amplifier, Physik Instrumente (PI) GmbH, Karlsruhe, Germany), and neuronal $[Ca^{2+}]_i$ transients were imaged in the left barrel cortex, at 180-250 μm depth below the dura, under ketamine-medetomidine sedation. The stimulation protocol consisted of 5Hz square pulses for 15 seconds that was repeated 6 times with 40 seconds intervals. Measurements to detect the GCaMP6s signal were performed at 920 nm wavelength, using the resonant scanner at 32.48 Hz and a Nikon 16x water immersion objective. Data acquisition was performed by MESc software (v.3.5.6.9395SLE, Femtonics Ltd.) and data analysed by MES software (v.5.3560, Femtonics Ltd.).

Tissue processing and immunostaining

Under terminal (ketamine-xylazine) anaesthesia mice were transcardially perfused with 4% paraformaldehyde (PFA) and brains were dissected. Brain samples were post-fixed, cryoprotected for 24h and 25 μm thick coronal sections were cut, using a sledge microtome (Leica, Germany). Immunostaining was performed on free-floating brain sections, blocked with 5% normal donkey serum (Jackson ImmunoResearch Europe Ltd, Ely, Cambridgeshire, UK). The following primary antibodies were used: rabbit anti-P2Y12R (1:500, #55043AS AnaSpec), chicken anti-GFP-tag (1:500, #A10262 Invitrogen), rat anti-CD206 (1:200,

#MCA2235, AbD Serotec) and biotinylated tomato lectin (1:100, #B-1175, Vectorlabs). After washing, sections were incubated with the corresponding secondary antibodies: donkey-anti chicken A488 (1:500, #703-546-155, Jackson Immunoresearch), streptavidin DyL405 (1:500, #016-470-084, Jackson ImmunoResearch), donkey anti-rabbit A647 (1:500, #711-605-152, Jackson ImmunoResearch) and donkey anti-rat A594 (1:500, #A21209, Invitrogen). Slices were mounted with Fluoromount-G (SouthernBiotech) or Aqua-Poly/Mount (Polysciences). For high resolution confocal laser scanning microscopy (CLSM) and electron microscopic assessments, 50 µm thick vibratome sections were washed in PB and TBS, followed by blocking with 1% human serum albumin (HSA). Sections were then incubated in different mixtures of primary antibodies: rabbit anti-P2Y12R (1:500, #55043AS AnaSpec), chicken anti-GFAP (1:500, #173 006 Synaptic Systems), goat anti-PDGFR-β (1:500, #AF1042 R&D Systems), rat anti-CD206 (1:200, #MCA2235, AbD Serotec), rat anti-PECAM-1 (1:500 , #102 501, BioLegend), mouse anti-αSMA (1:250, #ab7817, Abcam), guinea pig anti-Aquaporin-4 (1:500, #429 004, Synaptic Systems), mouse anti-TOM20 (1:500, #H00009804-M01, Abnova), guinea pig anti-Iba1 (1:500, #234 004, Synaptic Systems), mouse anti-Kv2.1 (1:500, #75-014, NeuroMab) and biotinylated tomato lectin (1:100, #B-1175, Vectorlabs). After washing in TBS, sections were incubated in the corresponding mixtures of secondary antibodies: donkey anti-chicken DyLight405 (1:500, #703-474-155, Jackson ImmunoResearch), donkey-anti chicken A488 (1:500, #703-546-155, Jackson ImmunoResearch), donkey anti-chicken A647 (1:500, #703-606-155, Jackson ImmunoResearch), donkey anti-rabbit A647 (1:500, #711-605-152, Jackson ImmunoResearch), donkey anti-rabbit A488 (1:500, #A21206, Invitrogen), donkey anti-rat A594 (1:500, #A21209, Invitrogen), donkey anti-rat A647 (1:500, #712-606-153, Jackson ImmunoResearch), donkey anti-mouse A594 (1:500, #A21203, Invitrogen), donkey anti-mouse A647 (1:500, #715-605-150, Jackson ImmunoResearch), donkey anti-guinea pig DyLight405 (1:500, #706-476-148, Jackson ImmunoResearch), donkey anti-guinea pig A594 (1:500, #706-586-148, Jackson ImmunoResearch), donkey anti-guinea pig A647 (1:500, #706-606-148, Jackson ImmunoResearch), streptavidin DyL405 (1:500, #016-470-084, Jackson ImmunoResearch), streptavidin A594 (1:500, #S11227, Invitrogen). Incubation was followed by washing in TBS and PB, then sections were mounted on glass slides with

Aqua-Poly/Mount (Polysciences). Immunofluorescence was analyzed using a Nikon Eclipse Ti-E inverted microscope (Nikon Instruments Europe B.V., Amsterdam, The Netherlands), with a CFI Plan Apochromat VC 60X oil immersion objective (NA 1.4) or a Plan Apochromat VC 20X objective (NA 0.75) and an A1R laser confocal system. The following lasers were used: 405, 488, 561 and 647 nm (CVI Melles Griot). Scanning was done in line serial mode. Image stacks were obtained with NIS-Elements AR 5.00.00 software.

Pre-embedding immunoelectron microscopy

After extensive washes in PB and TBS (pH 7.4), vibratome sections were blocked in 1 % HSA. Then, they were incubated with rabbit anti-P2Y12R (1:500, #55043AS AnaSpec) alone or mixed with mouse anti-GFAP (1:1000, #G3893 Sigma) in TBS for 2-3 days. After several washes, sections were incubated in blocking solution (Gel-BS) containing 0.2% cold water fish skin gelatine and 0.5 % HSA for 1 h. Next, sections were incubated with 1.4 nm gold-conjugated goat anti-rabbit Fab-fragment (1:200, #2004 Nanoprobes) alone or mixed with biotinylated donkey anti-mouse (1:500, #715-065-150 Jackson Immunoresearch) antibodies diluted in Gel-BS overnight. After extensive washes, sections were treated with 2 % glutaraldehyde for 15 min to fix the gold particles into the tissue. For the combined immunogold-immunoperoxidease reactions, this was followed by an incubation in avidin–biotinylated horseradish peroxidase complex (Vectastain Elite ABC kit; 1:300; Vector Laboratories) for 3 h at room temperature (RT) or overnight at 4°C. The immunoperoxidase reaction was developed using 3,3-diaminobenzidine (DAB; Sigma-Aldrich) as chromogen. To develop the immunogold reaction, sections were incubated in silver enhancement solution (SE-EM; Aurion) for 40-60 min at RT. The sections were then treated with 0.5 % OsO_4 in PB, at RT, dehydrated in ascending alcohol series and in acetonitrile, and were embedded in Durcupan (ACM; Fluka). During dehydration, sections were treated with 1 % uranyl acetate in 70 % ethanol for 20 min. For electron microscopic analysis, tissue samples from the somatosensory cortex (S1) were glued onto Durcupan blocks. Consecutive 70 nm-thick (for conventional electron microscopic analysis) or 150 nm-thick (for electron tomography) sections were cut using an ultramicrotome (Leica EM UC6) and picked up on Formvar-coated single-slot grids. Ultrathin sections for conventional electron microscopic analysis

were examined in a Hitachi H-7100 electron microscope equipped with a Veleta CCD camera (Olympus Soft Imaging Solutions, Germany). 150 nm-thick electron tomography sections were examined in FEI Tecnai Spirit G2 BioTwin TEM equipped with an Eagle 4k camera.

Electron tomography, analysis

Before electron tomography, serial sections on single-slot copper grids were photographed with a Hitachi H-7100 electron microscope and a Veleta CCD camera. Serial sections were examined at lower magnification, and P2Y12R-positive microglial processes contacting the vasculature were selected. After this, grids were put on drops of 10 % HSA in TBS for 10 minutes, dipped in distilled water (DW), put on drops of 10 nm gold conjugated Protein-A (Cytodiagnostics #AC-10-05) in DW (1:3), and washed in DW. Electron tomography was performed using a Tecnai T12 BioTwin electron microscope equipped with a computer-controlled precision stage (CompuStage, FEI). Acquisition was controlled via the Xplore3D software (FEI). Regions of interest were pre-illuminated for 4-6 minutes to prevent further shrinkage. Dual-axis tilt series were collected at 2 degree increment steps between -65 and +65 degrees at 120 kV acceleration voltage and 23000x magnification with -1.6 – -2 μm objective lens defocus. Reconstruction was performed using the IMOD software package. Isotropic voxel size was 0.49 nm in the reconstructed volumes. After combining the reconstructed tomograms from the two axes, the nonlinear anisotropic diffusion (NAD) filtering algorithm was applied to the volumes. Segmentation of different profiles has been performed on the virtual sections using the 3Dmod software.

Post mortem human brain samples

Post mortem human brain tissue was obtained from one 60-years-old female, one 73-years-old male and one 27-years-old male patient without any known neurological disease as also confirmed by neuropathological examination (ETT TUKEB 31443/2011/EKU [518/PI/11]). Informed consent was obtained for the use of brain tissue and for access to medical records for research purposes. Tissue was obtained and used in a manner compliant with the Declaration of Helsinki. Brains of patients who died in non-neurological diseases were removed 4-5 h after death (Table 1). The internal carotid and the vertebral arteries were

DOI:10.14753/SE.2023.2742

cannulated, and the brain was perfused first with heparin containing physiological saline, followed by a fixative solution containing 4% PFA, 0.05% glutaraldehyde and 0.2% picric acid (vol/vol) in PB. The hippocampus was removed from the brain after perfusion, and was postfixed overnight in the same fixative solution, except for glutaraldehyde, which was excluded. Blocks were dissected, and 50 μm thick sections were prepared on a vibratome (VT1200S, Leica, Germany).

DOI:10.14753/SE.2023.2742

Table 1. Patient data and processing of post-mortem human brain tissues.

Subject	Code	Gender	Age (years)	Health status	Comorbidities	Cause of death	Tissue sample type
Control subject	SKO13	female	60	normal	chronic bronchitis	respiratory arrest	free floating and paraffin sections
Control subject	SKO16	male	73	normal	Unspec. atherosclerosis, pneumonia	respiratory arrest	free floating and paraffin sections
Control subject	SKO20	male	27	normal	unspec. jaundice, malignant pancreatic neoplasm.	pulmonary embolism	free floating sections

Laser Speckle Contrast Imaging (LSCI)

CBF was measured by a PeriCam PSI High Resolution LSCI system (Perimed AB, Järfälla-Stockholm, Sweden). Before CBF measurements, the head of the mouse was secured in a stereotaxic head holder, and after a midline incision, the skull was exposed by retracting the scalp. Imaging was performed through the intact skull bone. The cerebrocortical microcirculation was imaged at 21 frames/sec frequency in a 10x10 mm field of view. Perfusion responses were expressed as a percentage of baseline CBF. Uniformly, a 1 min

long baseline was set in all experiments, registered at the beginning of the measurements. Three adjacent ROIs were placed (denoted as MCA1-3) over the middle cerebral artery (MCA) territory both to the ipsilateral and to the contralateral hemispheres to assess microglia-mediated effects on gradual perfusion changes ranging from the MCA core region to the midline. CCA occlusion experiments were performed under ketamine-xylazine (i.p. 100mg/kg - 10mg/kg) anaesthesia. The whisker stimulation protocol was performed under mild ketamine-medetomidine (i.p. 30mg/kg – 0.1mg/kg) sedation (212) with ROIs placed over the contralateral barrel cortex. The hypercapnic challenge was done under mild ketamine-medetomidine (i.p. 30mg/kg – 0.1mg/kg) sedation and ROIs were placed over the left and right hemispheres excluding venous sinuses.

Selective elimination of microglia from the brain

C57BL/6J mice were fed a chow diet containing the CSF1R inhibitor, PLX5622 (Plexxikon Inc., 1200 mg PLX5622 in 1 kg chow) to eliminate microglia from the brain (176), or with control diet for 3 weeks.

Cisterna magna injection for drug delivery into the brain and intraperitoneal drug administration

To block P2Y12 receptor (P2Y12R)-mediated microglial actions, a P2Y12R antagonist, PSB0739 (dissolved in 0.9% saline, 40 mg/kg in 5 μl volume, #3983, Bio-Techne Corp., Minneapolis, USA) was injected into the cisterna magna 35 min prior imaging, while vehicle (0.9% saline) injection was used as control. Cisterna magna injections were done under 1-1.5% isoflurane anaesthesia. L-NAME, a non-selective Nitric Oxide Synthase (NOS) inhibitor (Tocris, Cat. No. 0665**)** was injected intraperitoneally (30 mg/kg dissolved in 0.9% saline) 5 minutes before imaging.

SPECT and PET imaging

Single photon emission computed tomography (SPECT) and positron emission tomography (PET) studies were carried out on mice anaesthetized with 2% isoflurane (213, 214). SPECT measurements were performed using the [^{99m}Tc]-HMPAO ligand (Hexamethylpropylene amine oxime, Medi-Radiopharma Co Ltd., Hungary). The acquisition started 3 minutes after the i.v. injection of the radiotracer via the tail vein (injected activity: 99.22 ± 9.33 MBq). The measurements were performed on a NanoSPECT/CT PLUS device (Mediso Ltd, Hungary) equipped with multi-pinhole mouse collimators. Measurements were reconstructed with 0.25 mm isovoxels and the results were quantified as units of radioactivity (MBq/ml). After SPECT acquisition, [^{18}F]-FDG (2-deoxy-2-(18F)fluoro-D-glucose) PET measurements were performed. PET acquisition started 20 minutes after i.v. [^{18}F]-FDG injection (Pozitron-Diagnosztika Ltd, Hungary; injected activity: 12.05 ± 1.93 MBq) with an acquisition time of 10 minutes using a microPET P4 (Concorde Microsystems Inc, USA). A maximum a posteriori algorithm was used to reconstruct the data with 0.3 mm isovoxels. After reconstruction, manual coregistration and atlas-based region of interest (ROI) measurements were done using VivoQuant software (InviCRO, USA) in the cerebellum, cerebral cortex and the whole brain. For microglia-depleted and control groups, mean [18F]-FDG and [99mTc]-HMPAO standardized uptake values (SUV) were analyzed by using two-way ANOVA followed by Sidak's post-hoc test (GraphPad Prism 7.0) and a permutation t-test in R 3.5.1 (R Foundation for statistical computing, Austria).

Whisker stimulation protocol

Whisker stimulation was performed manually and electromechanically (with a bending actuator #PL112-PL140, PICMA, Bender connected to a piezo amplifier #E-650 Amplifier, Physik Instrumente (PI) GmbH, Karlsruhe, Germany). For manual stimulation an earpick was used (at 4-5 Hz frequency) according to the following protocol: left whiskers were stimulated for 30 sec, repeated 6 times, 60 sec apart. During electromechanically controlled stimulation (5 Hz) whiskers were stimulated for 15 sec, repeated 10 times with 40 sec intervals. Stimulation-evoked CBF responses in the contralateral barrel cortex were recorded. CBF measurements were carried out under ketamine-medetomidine sedation (30 mg/kg - 0.1

mg/kg dissolved in 0.9% saline, i.p.). All coupling experiments performed were time-matched from the time of anesthetic injection to ensure comparable results across different experiments.

Functional ultrasound (fUS)

The acquisition was done with a 15 MHz probe of 128 elements (Vermon SA, France) connected to a prototype ultrafast research ultrasound scanner (hardware and software functionally analogous to the Iconeus One system, Iconeus, Paris, France). Recordings were performed through the skull while the animal was anaesthetised with ketamine-medetomidine (i.p. 30mg/kg - 0.1mg/kg). The head of the animal was shaven and fixed into a stereotactic frame. The probe was positioned using a built-in software based registration to the 3D Allen Brain Atlas (2015 Allen Institute for Brain Science, Allen Brain Atlas API, available from: brain-map.org/api/index.html). The Doppler Images were obtained as described earlier (215). 11 tilted planes were insonificating the medium at 5500 Hz pulse repetition frequency to compute one compounded image every 2 ms. Out of a block of 200 images a Power Doppler image was obtained by removing the 60 first modes of SVD decomposition to extract the blood signal (216) from tissue clutter at a 2.5 Hz sampling rate. Acquisition started and ended with a 5 min baseline followed by 10 phases of 30 s manual stimulation of the whiskers (217) with 1 min of resting in between. A fourth order polynomial detrending of the data was applied to remove drifts of baseline (218).

In vivo electrophysiology

Surgical procedures, microdrive construction and implantation have been described previously (219). Briefly, custom-built microdrives with eight nichrome tetrodes (diameter, 12.7 μm, Sandvik, Sandviken, Sweden) and a 50-μm core optic fiber (outer diameter, 65± 2 μm, Laser Components GmbH, Olching, Germany) were implanted into the right barrel cortex AP: -1.4; ML: 3.0 DV 0.75−2.0 mm. Although photostimulation was not applied here, the optic fiber is part of our typical drive design as it also provides mechanical support for the tetrodes. The microdrive contained a moveable shuttle allowing more precise targeting. The custom-built microdrives were implanted under deep anaesthesia using an

intraperitoneal injection of ketamine - xylazine (125 mg/kg - 25 mg/kg in 0.9% NaCl). Lidocain spray was used on the skin of the scalp to achieve local analgesia. The skin was incised, the skull was cleaned and leveled, and a cranial window was opened above the target area. Fluorescent dye (DiI, #LSV22885, Invitrogen) was applied on the tip of the tetrodes for later histological localization. Implants were secured by dentil adhesive (C&B Metabond, Parkell, Edgewood, NY, USA) and acrylic resin (Jet Denture, Lang Dental, Wheeling, USA). Buprenorphine was used for post-operative analgesia (Bupaq, 0.3 mg/ml, Richter Pharma AG, Wels, Austria). The stereotaxical surgery was followed by a 3 day-long resting period. During electrophysiological recordings animals were anesthetized using an intraperitoneal injection of a ketamine – medetomidine (3mg/kg – 0.1 mg/kg). The experiment was repeated twice or three times, with a two days gap between sessions. Tetrodes were lowered (40-120 μm based on the estimated electrode positions and the presence of single units) between recording sessions to collect neuronal activity from different dorsoventral position. Every session started with a 5min recording without stimulation, defined as basal activity. Automated whisker stimulation epochs lasted for 15 seconds with 5 Hz frequency, followed by a 40-second-long interstimulus period. During the stimulation, 5Hz frequency was generated with a TTL pulse generator, where the pulse duration and the interpulse interval was 0.1- 0.1 second. In every 0.2 seconds the whisker stimulator moved forward, and after 0.1 second it passively moved backward to the starting position. This pattern resulted in a bidirectional 10Hz stimulation. Stimulation was repeated 10 times. The entire protocol was repeated with the stimulator positioned close to the whiskers without touching them, to provide a sham stimulation condition that allowed us to exclude possible contaminations from electric noise from the stimulator circuit in our recordings. Next, manual whisker stimulation was applied (15 seconds stimulation with 40 seconds interstimulus period, repeated two times). Finally, changes in neuronal firing were measured during a 2 minutes long hypercapnic challenge, by inhalation of a 10% CO_2 containing air mixture (21.1% O_2 and N_2 ad 100%) under normoxic conditions. After the last experiment, animals were terminally anesthetized and were transcardially perfused with 0.1 M PBS for 1 min, then with 4% PFA in PBS. After perfusion, brains were post-fixed and sections (50 μm coronal sections, Vibratome VT1200S, Leica) were imaged by fluorescence microscope (Nikon

Eclipse Ni microscope, Nikon Instruments). Images were aligned to coronal sections of the Paxinos and Franklin atlas to accurately reconstruct the recording locations. Data acquisition was conducted with an Open Ephys (open source data acquisition system, hiv4) board, synchronized with the electromechanical whisker stimulator through a pulse generator (PulsePal 1102, Sanworks) (220). Data analysis was performed in Matlab R2016a (Mathwoks, Natick, US). Spike sorting was carried out using MClust 3.5 (A.D. Redish). Only neurons with isolation distance > 20 and L-ratio < 0.15 (a cluster quality measure based on Mahalanobis-distance (221) were included.

Induction of hypercapnia in vivo

Under mild ketamine-medetomidine (i.p. 30 mg/kg - 0.1 mg/kg) sedation, baseline cortical blood flow was recorded with LSCI for 5 minutes, then hypercapnia was induced by inhalation of a 10% CO_2-containing air mixture (21.1% O_2 and N_2 ad 100%) for 2 minutes under normoxic conditions, followed by a 2 minutes long post-hypercapnic imaging period. In a group of control and microglia-depleted mice, before the hypercapnic challenge, 0.01 µg/g atipamezole (CP-Pharma, Revertor, 5mg/ml) was administered i.p. to withdraw α-2-agonistic effects of medetomidine. Three to five minutes were allowed to get the effect of atipamezole established, before recording baseline CBF and induction of hypercapnia.

Blood gas analysis

Under ketamine-medetomidine anaesthesia (30mg/kg – 0.1mg/kg ± 0.1µg/g atipamezole), the left femoral artery was exposed and cannulated for arterial puncture. Arterial blood (45-75µl) was sampled to glass capillaries before and after 2min hypercapnic challenge (induced by inhalation of a 10% CO_2 containing air mixture [21.1% O_2 and N_2 ad 100%] under normoxic conditions with 2L/min flow rate), and samples were measured with a blood gas analyzer (ABL90 FLEX PLUS, Radiometer Medical, Brønshøj, Denmark) to determine arterial blood gas tensions (pO_2, pCO_2) and pH.

Acute slice hypercapnia experiment and cGMP immunolabeling

Mice were deeply anesthetized with isoflurane (n=3) and decapitated, the brains were removed, and 300 μm thick horizontal hippocampal slices were cut on vibratome (Leica; VT1200S). Slices were placed into an interface-type incubation chamber which contained standard ACSF at 35°C that gradually cooled down to room temperature. Slices were preincubated for 20 minutes with 1 ml of modified ACSF (mACSF) containing 1 mM IBMX, 10μM BAY 73-6691 phosphodiesterase inhibitors (PDEInhs; to avoid cGMP hydrolysis) and 0.2mM L-arginine (the substrate of NOS). L-Arginine (0.2 mM) alone had no effect on NOS activity and cGMP levels (222). For selective blockade of the microglial P2Y12R, 2 μM PSB0739 (in mACSF) was used. After preincubation in mACSF or mACSF+PSB0739, slices were gradually subjected to hypercapnia by elevating the CO_2 level from 5% to 14.6% with bubbling. 200 μM SNP (NO donor) was used as a positive control. After 15 minutes hypercapnia, the slices were immediately fixed with ice-cold 4% paraformaldehyde for 48 h at 4°C. After washing with 0.1 M PB, slice were embedded to 4% agar and 50 μm thick vibratome (Leica; VT1200S) sections were cut followed by an immunfluorescent labeling. Sections were incubated in the following primary antibody mixture: sheep anti-cGMP (1:4000, from J. de Vente, Maastricht), rat anti-CD13 (1:500, Biorad MCA2183EL), biotinylated tomato Lectin (1:500, Vectorlabs B-1175) and rabbit anti-P2Y12 receptor (1:2000, AnaSpec 55043A) diluted in PBS for 48h at 4°C. After subsequent washes in PBS, sections were incubated in a mixture of corresponding secondary antibodies (all from Jackson ImmunoResearch): donkey anti-sheep Alexa488 (1:500, 713-546-147), donkey anti-rat Alexa647 (1:500, 712-606-153), streptavidin Dylight405 (1:500, 016-470-084) and donkey anti-rabbit Alexa594 (1:500, 711-586-152) diluted in PBS. Sections were mounted onto glass slides, coverslipped with Slowfade Diamond antifade mountant (Invitrogen, S36972, RI: 1.52) and Menzel-Glaser coverslip (#1). All steps have been performed below 4°C. Fluorescent images were acquired using a Nikon Eclipse Ti-E inverted microscope (Nikon Instruments Europe B.V.), with a Plan Apochromat VC 20X objective (numerical aperture: 0.75) and an A1R laser confocal system, scanning was done in line serial mode, pixel size was 0.31μm. Image stacks were obtained with NIS-Elements AR. IBMX (3-Isobutyl-1-methylxanthine), BAY 73-6691 (1-(2-chlorophenyl)-6-[(2R)-3,3,3-trifluoro-2-

methylpropyl]-1,5-dihydro-4H-pyrazolo[3,4-d]pyrimidine-4-one), L-arginine and SNP (sodium nitroprusside) were purchased from Sigma-Aldrich and PSB0739 from Tocris.

Simultaneous measurement of CBF and brain pH during hypercapnia

Electrophysiological variables (DC potential, brain pH) and local CBF (by lased Doppler) were simulatenously monitored after craniotomy using ion-sensitive microelectrodes connected to a custom-made dual-channel high input impedance electrometer (including AD549LH, Analog Devices, Norwood, MA, USA) via Ag/AgCl leads and associated filter modules (NL106 and NL125, NeuroLog System, Digitimer Ltd., United Kingdom). Ion-sensitive microelectrodes were prepared according to Voipio and Kaila (223). In each experiment, a pH-sensitive microelectrode was lowered into the cortex with a micromanipulator, together with another glass capillary microelectrode (tip diameter = 20 μm) filled with saline to serve as reference. The tips of the two electrodes were positioned as near as possible. The reference electrode acquired slow cortical or DC potential. An Ag/AgCl electrode was implanted under the skin of the animal's neck to be used as common ground. The voltage signal recorded by the reference electrode was subtracted from that of the pH-sensitive microelectrode by dedicated differential amplifiers and associated filter modules (NL106 and NL125, NeuroLog System, Digitimer Ltd., United Kingdom), which yielded potential variations related to changes in H^+ ion concentration. The recorded signals were then forwarded to an analogue-to-digital converter (MP 150, Biopac Systems, Inc). Electric signals were continuously acquired at a sampling frequency of 1 kHz using the software AcqKnowledge 4.2.0 (Biopac Systems Inc., USA). Extracellular pH changes were expressed in mV to be translated into pH units offline, using least squares linear regression. The laser-Doppler flow (LDF) signal was digitized and displayed together with the DC potential and pH signals (MP 150 and AcqKnowledge 4.2.0, Biopac Systems, Inc.). Surgical preparations were done under 1.5–2% isoflurane, while pH and LDF measurements were performed under medetomidine anesthesia (initiation: i.p. 0.5 mg/kg, repeated 5 min later for maintenance) in a Faraday cage. After 15 min baseline acquisition, 2min hypercapnia was imposed by CO_2-enriched gas inhalation (9.7 % CO_2, 21 % O_2 in N_2, Messer, Hungary) at spontaneous respiration, which was repeated after a 5 min resting period.

DOI:10.14753/SE.2023.2742

Repeated, transient CCA occlusion

Transient, repeated unilateral common carotid artery (CCA) occlusion was performed to induce hypoperfusion without causing ischemia or cellular injury to the brain. The CCA was temporarily pulled away with a silk suture for 5 min, followed by a 5 min-long reperfusion period. The protocol consisted of repeating these steps three times (3x CCAo) on anesthetised (ketamine-xylazine, i.p. 100mg/kg - 10mg/kg dissolved in 0.9% saline) mice. During CBF measurements, the core temperature of mice was maintained at 37 ± 0.5°C using a homeothermic blanket.

Elimination of perivascular macrophages

Perivascular macrophages (PVMs) were depleted by a single dose of clodronate-containing liposomes (70µg/mouse in 10µl volume, #F70101C-N-2, FormuMax Scientific, Inc.) injected into the left ventricle (ICV) as described earlier (224). Three days later, at maximal efficacy of depletion, laser speckle contrast imaging (LSCI) was carried out.

Focal cerebral ischemia

Anaesthesia was induced by inhalation of 4% isoflurane (30% oxygen and 70% nitrous oxide gas mix, AbbVie Ltd, UK or Linde Ltd, Hungary) and was maintained at 1.75%. Body temperature was monitored throughout surgery (via rectal probe) and maintained at 37 °C ± 0.5 °C using a heating blanket (Harvard Apparatus, Edenbridge, Kent, UK). A laser Doppler blood flow monitor (Oxford Optronix, Abingdon, UK) was used to monitor cerebral blood flow (CBF). Focal cerebral ischaemia was induced by MCAo based on a previously described protocol (225). Briefly, a hole was made into the temporalis muscle (6 mm lateral and 2 mm posterior from bregma) to allow a 0.5 mm diameter flexible laser-Doppler probe to be fixed onto the skull and secured in place by tissue adhesive (Vetbond, UK). A midline incision was made on the ventral surface of the neck and the right common carotid artery isolated and ligated. Topical anaesthetic (EMLA, 5% prilocaine and lidocaine, AstraZeneca, UK) was applied to skin incision sites prior to incision. The internal carotid artery and the pterygopalatine artery were temporarily ligated. A 6-0 monofilament (Doccol, Sharon, MA,

USA) was introduced into the internal carotid artery via an incision in the common carotid artery. The filament was advanced approximately 10 mm distal to the carotid bifurcation, beyond the origin of the middle cerebral artery. Relative CBF was monitored for the first 30–45 min following MCAo, during which time relative CBF had to reduce by at least 70% of pre-ischaemic values for inclusion. After 45 min of occlusion the filament was withdrawn back into the common carotid artery to allow reperfusion to take place. The wound was sutured and mice received a subcutaneous bolus dose of saline for hydration (500 µl) and a general analgesic (Buprenorphine, 0.05 mg/kg injected subcutaneously, Vetergesic, UK). Animals were kept at 26–28 °C until they recovered from anaesthesia and surgery, before being transferred back to ventilated cages suspended over a heating pad with free access to mashed food and water in normal housing conditions.

Laser Speckle Contrast imaging for stroke experiments

At the end of the MCAo surgery, mice were transferred to the stereotaxic frame and LSCI measurements performed 30 min after reperfusion under isoflurane anaesthesia, using a PeriCam PSI High Resolution system (Perimed AB, Järfälla-Stockholm, Sweden). To assess CBF changes in different groups of mice in a uniform manner, tamoxifen-treated IL-1R1$^{fl/fl}$ $^{\Delta\ Slco1c1}$ mice and tamoxifen-treated control IL-1R1$^{fl/fl}$ mice were subjected to MCAo for 45 min (left side occluded). LSCI measurements were performed 30 min after reperfusion. The skin on the top of the skull was opened and imaging performed through the intact skull bone to visualize cortical perfusion changes for 10 min at 16 frames/sec in 20 µm/pixel resolution, using a 10 × 10 mm field of view. To evaluate recovery of blood flow in the penumbra after stroke, perfusion changes were assessed in three adjacent regions of interest (ROI) in the primary MCA area (Figure 31. a) LSCI is particularly sensitive to assess perfusion changes in the microcirculation. The area of cortical sinusoids have been excluded from ROIs and only measurements without motion artefacts have been analysed to minimize bias (226, 227). Area under the curve (AUC) values over the 10 min imaging period for each ROI were determined and data expressed as percentage values of the corresponding contralateral ROI.

3.3. *In vitro* experiments

Primary endothelial cells

Primary endothelial cultures were prepared from 6-8 weeks old C57BL/6J mouse brains as described earlier (228), now performed with modifications (229). In brief, mouse forebrains were collected to PBS and the meninges were removed using sterile chromatography paper. The tissue was cut into small pieces by scalpels and was enzymatically digested in a mixture of Collagenase II (CLS2, 1mg/ml, #C6885, Sigma) and DNase I (0.025mg/ml, ~50U, #D4513, Sigma) in DMEM-F12 (#10-103-CV, Corning) for 55 min at 37C°. Using a 20% BSA (#A7906, Sigma, in DMEM-F12) gradient (1000x g, 20 min, three times), microvessels were separated from the myelin. The collected microvessels were further digested using a mixture of Collagenase/Dispase (1mg/ml, #11097113001, Sigma) and DNase I (0.038mg/ml, ~75U, #D4513, Sigma) for 35 min at 37C°. Digested cerebral microvessels were washed three times with DMEM-F12, then seeded to Collagen type I (#354236, Corning) coated plates. During the first four days, puromycin (230, 231) (4µg/ml, #P7255, Sigma) selection was applied in the primary medium (15% PDS [#60-00-850, First Link] for seeding, 10% for cultivation, 1ng/ml bFGF [#F0291, Sigma], 100µg/ml heparin [#H3149, Sigma], 100x ITS [#41400045, Gibco], 4µg/ml puromycin in DMEM-F12) to selectively eliminate P-gp non-expressing cells. After reaching confluency in 5-6 days, the cells were passaged to Collagen type IV (100µg/ml, #C5533, Sigma) and fibronectin (25µg/ml, #F1141, Sigma) coated 48-well plates at a cell density of 15.000 cells/well, and used for *in vitro* hypoxia or hypercapnia experiments in P1.

Primary astroglia and microglia cells

Primary cultures of astroglial cells were prepared from neonatal mouse brains, as described earlier (232). In brief, meninges were removed from P0-P2 whole brains and tissues were chopped. The tissue pieces were digested with 0.05% w/v trypsin and 0.5mg/ml DNAse I (both from Sigma, #T4549, #DN25) in phosphate-buffered saline for 10min, at RT. Cells were then plated onto poly-L-lysine (#P1524, Sigma) coated plastic surfaces at a cell density of 3–4 × 10^5 cell/cm^2. The cultures were grown in Minimal Essential Medium (#21090022, ThermoFisher) supplemented with 10% fetal bovine serum (#FB-1090, BioSera), 4 mM

glutamine (#G3126, Sigma), and 40 μg/ml gentamycin (Sandoz). The culture medium was changed twice a week. For the hypoxia/hypercapnia experiments, the primary cultures were passaged and plated in $1{,}5 \times 10^5$ cell/cm^2 density into poly-L-lysine coated 48 well plates and used within 96hrs. Astrocytes no older than 6-8 days *in vitro* were used. Primary microglia cells were isolated from astroglia/microglia mixed cultures derived from the whole brains of C57BL/6J newborn mouse pups. Microglia isolation was performed between days 21 and 28 of culture maintenance, by mild trypsinization (233). For the *in vitro* hypoxia and hypercapnia experiments the isolated cells were seeded in a $1{,}5 \times 10^5$ cell/cm^2 density into poly-L-lysine coated 48 well plates and used within 48hrs.

In vitro hypoxia and hypercapnia

Cytation 5 Cell Imaging Multi-Mode Reader (BioTek) equipped with $O2/CO_2$ gas controllers was used to maintain 1% O2/5% CO2/94% N2 (Hypoxia) or 15% CO2/85% air (Hypercapnia) levels at 37^{o}C. Endothelial or astroglial cells grown in 48 well plates to confluency, or microglia were placed into the reading chamber of the instrument for 5 (Hypercapnia) or 10 minutes (Hypoxia), after taking the lids off. In order to avoid medium-change induced release events, cell culture medium was replaced with 400ul complete fresh medium 16hrs before the onset of the experiments. To follow the build-up of hypoxia at the cellular level some cultures were loaded with 5μM Image-iT™ Green Hypoxia Reagent (#I14834, Invitrogen) for 30min at 37^{o}C. The Hypoxia Reagent begins to fluoresce when atmospheric oxygen levels drop below 5%. Fluorescent images taken with Cytation5 (10x magnification) at 0/10minutes were analyzed with FIJI software (v1.53, NIH), measuring mean gray values in 10x10 pixel ROIs of n=50 individual cells from 3 independent experiments. Changes in medium pH during hypercapnia were measured by Phenol Red absorbance at 415 and 560 nm using the Cytation 5 Multi-Mode Reader (BioTek) (234). Measurements were taken from 400 μL complete cell culture media in 48-well plates at 37 °C (n=10). The ratios of the 415 nm and 560 nm peaks were analyzed against a calibration curve obtained from 10mg/L phenol red and 10% FBS containing phosphate buffer solutions at different pH, in the range of pH=5,5-8. Changes in the intracellular pH during hypercapnia were determined by fluorescence intensity readings of pHrodo Green AM (#P35373,

Invitrogen) labeled glial cells with Cytation 5 Multi-Mode Reader (n=4). Intracellular pH calibration was performed by incubating the pHrodo Green AM labeled cells in ACSF set to different pH values between pH=5,5-7,5 and supplemented with 10μM Nigericin and 10μM Valinomycin (#431, Nigericin; #3373 Valinomycin, Bio-Techne Corp.), for 5 minutes.

Quantification of nucleotides and nucleoside

Released concentrations of adenine nucleotides (ATP, ADP, AMP) and adenosine (Ado) from culture media and tissue homogenates were determined using HPLC by Shimadzu LC-20 AD Analytical System using UV (Agilent 1100 VW set at 253 nm) detection. Concentrations were calculated by a two-point calibration curve using internal standard method. The data (n=4 or 5 in each group) are expressed as nmol per mL. Briefly, the medium (400 μl) was transferred into a cold Eppendorf tube which contained 50 μl of 0.1 M perchloric acid with 10 μM theophylline (as an internal standard) solution, then samples were centrifuged (at 3510 × g for 10 min at 0-4^{o}C) and the supernatants were kept at -20^{o}C until analysis. The weighed frozen tissue was homogenized in the same solution as the media and the precipitated protein content was removed by centrifugation at 3510 × g for 10 minutes at 4 ° C. The pellet was saved for protein measurement according to Lowry (235). A 4 M K_2HPO_4 solution was used to neutralize the supernatant and the centrifugation step was repeated. The extracted purines were kept at -20^{o}C until analysis. Online Solid Phase Extraction coupled to the column-switching technique was applied to quantification of the nucleotide content of samples. HPLC separation was performed by Shimadzu LC-20 AD Analytical System using UV (Agilent 1100 VW set at 253 nm) detection. The phenyl-hexyl packed (7.5 x 2.1 mm) column was used for online sample enrichment and the separation was completed by coupling the analytical C-18 (150 × 2.1 mm) column. The flow rate of the mobile phases [“A” 10 mM potassium phosphate buffer with 0.25 mM EDTA and phase “B” contained additional components such as 0.45 mM octane sulphonyl acid sodium salt, 8% acetonitrile (v/v), 2% methanol (v/v), and the pH 5.55] was 350 or 450 μl/min, respectively in a step gradient application (236). The sample enrichment flow rate of buffer “A” was 300 μl/min during 4 min and the total runtime was 55 min. Concentrations of the homogenates

were calculated by a two-point calibration curve using internal standard method. The data (n=4 or 5 in each group) are expressed as pmol per mg protein or nmol per mg.

3.4. Quantitative analysis

All quantitative analyses were done in a blinded manner. To analyse microglial process coverage of endothelial surface or pericytes, microglial process coverage was measured on confocal Z-stacks acquired with a step size of 300 nm. On single-channel images, lectin-positive vessels were selected randomly. The surface of these vessels was calculated by measuring their circumference on every section multiplied by section thickness. The length of microglial process contacts was measured likewise. Continuous capillary segments (shorter than 6 μm) were also randomly chosen, and the presence of microglial process contacts was examined. All labeled and identified pericytes (PDGFRβ-positive) were counted when the whole cell body was located within the Z-stack. 3-dimensional reconstruction of CLSM and 2-photon imaging stacks was performed using the IMOD software package (237). TOM20 fluorescent intensity profiles were analyzed using a semi-automatic method (Figure 9. j). Confocal stacks with triple immunofluorescent labeling (P2Y12R, TOM20 and Lectin) were collected. The image planes containing the largest diameter of longitudinal or cross-cut vessels were used to trace the outer membrane of endothelial cells based on the Lectin-labeling. This contour was then expanded and narrowed by 0.5 μm to get an extracellular and an intracellular line, respectively. The intensity of fluorescent labeling was analyzed along these lines (TOM20 intensity along the intracellular, P2Y12R-labeling along the extracellular line). After normalizing and scaling, microglial contacts were identified along the membrane of the endothelial cell, where microglial fluorescent intensity was over 20% of the maximal value, for at least along a 500 nm long continuous segment. Then the contact area was extended with 500-500 nm on both sides, and TOM20 fluorescent intensity within these areas was measured for “contact” value. TOM20 fluorescent intensity outside these identified contacts was considered “non-contact”. For the analysis of $GFAP^+$ astroglial cell body contact frequency, CLSM stacks with double immunofluorescent labeling (GFAP and P2Y12R) were acquired from mouse cerebral cortex. All labeled and identified astrocytes were counted when the whole cell body was

located within the Z-stack. To assess microglia process motility, baseline (28 min) and after 3x CCAo (49 min) two-photon image sequences were exported from MES software v.5.3560 (Femtonics Ltd., Budapest, Hungary) and analysed using FIJI (version 2.0.0, NIH, USA). The acquired hyperstacks were motion corrected using the StackReg plugin, then individual perivascular microglia processes (30 processes/image/plane) were tracked using the Manual Tracking plugin of FIJI. Based on the obtained XYZ coordinates, process motility speed was calculated. To study the effects of 3xCCAo on microglial morphology, 3-3 C57BL/6J mice were randomized into two groups: CCAo, or sham surgery. 24 hours after 3x CCAo, mice were transcardially perfused and processed for automated microglial morphology analysis. In both cases, 100µm thick sections with microglia (Iba1) and cell nuclei (DAPI) labeling were imaged with CLSM (0.2µm/pixel, Z-step of 0.4µm). Obtained confocal stacks were processed with the Microglia Morphology Quantification Tool (238). For LSCI recordings, venous sinuses were excluded from the analysis. LSCI generates relative perfusion values (arbitrary units) therefore CBF was expressed as percentage change over baseline values in the 3x CCAo experiments. For the CCA occlusion experiments, a 1 min long period (typically 250 datapoints), recorded at the beginning of the imaging session, was averaged and considered as baseline. Then, every occlusion and reperfusion event was normalized to baseline. To assess the plasticity of the cerebrovasculature in response to repeated hypoperfusion, normalized occlusion or reperfusion events were averaged and compared between experimental groups. To demonstrate the CBF kinetics of individual animals, every 20th image was extracted and CBF values presented on a scatter plot (Figure 27. b). Quantification of P2Y12R immunostaining in control and microglia depleted tissues or P2Y12R and CD206 immunostaining in control and clodronate-treated mice were performed in at least three, randomly selected fields of view within the cortex, on three different coronal planes in each mouse. Data obtained from every mouse brains were averaged and compared between experimental groups. To investigate microglial actions on hypercapnic vasodilation, two photon image sequences were exported from the MESc software v.3.5.6.9395 (Femtonics Ltd.). After motion correction using the StackReg plugin of FIJI, the extent of vasodilation was measured and expressed as percentage of baseline at maximal vasodilation using FIJI. Obtained data were averaged and compared between control and microglia

depleted or between CX3CR1$^{GFP/+}$ and CX3CR1$^{GFP/+}$ x P2Y12R KO mice. The hypercapnia-evoked CBF responses (2 min long) were normalized to the baseline, then maximum values of individual responses were averaged per animal and compared between control and microglia depleted groups. For the analysis of cGMP fluorescence, a systematic random sampling of parenchymal vessels based on the Lectin staining was performed. These vessel segments were numbered and their lumen diameter was measured. This was followed by masking the CD13+ profiles of these vessels and automated cGMP intensity measurement was performed within these masks. Measurements were done using ImageJ software. Concentrations of released cellular purine nucleotides in response to hypoxia or hypercapnia were calculated by a two-point calibration curve, using internal standard method. The obtained values were averaged and compared to baseline ones. For neurovascular coupling experiments (manual and electromechanical whisker stimulations) the stimulus-evoked responses were normalized to baseline and were expressed as CBF increase (% change). The evoked CBF responses were averaged per mouse. The magnitude of evoked CBF responses was compared between experimental groups. Before and after L-NAME injection whiskers were stimulated, the difference between the two sets of stimulations was analyzed and compared between the experimental groups. GCaMP6s signals of individual neurons were collected with MESc software v.3.5.6.9395 (Femtonics Ltd.) and imported into the MES software v.5.3560 (Femtonics Ltd.) curve analysis module. The individual cellular $[Ca^{2+}]_i$ traces were normalized to the baseline GCaMP6s signal and data were derivated to relative fluorescence intensity change ($\Delta F/F$). Then area under the curve (AUC) was calculated for each response, and AUC values were compared between experimental groups. During electrophysiological assessment, the baseline frequency of individual units was determined by averaging a 5min long period at the beginning of registration, when whisker stimulation was not applied. Only those units were selected for further analysis, which responded to electromechanical stimulations. Then the stimulus-evoked responses were corrected to baseline frequencies (called as baseline corrected response frequency) and the magnitude of responses was compared between experimental groups. Signal extraction from the microglial $[Ca^{2+}]_i$ time-lapse series in response to ATP treatment was computed on FIJI (ImageJ, NIH). In brief, the mean fluorescence intensity values were determined in 10μmx10μm ROIs (each

representing an individual cell), and were used to calculate dF/F values (dF/F = (F-F0)/F0; where F0 is the average baseline fluorescence within a 300sec time window before drug application and F is the background corrected fluorescence intensity value at a given time point). The data were further analyzed with Clampfit software (pClamp10 suite; Molecular Devices), manually determining the peak time and amplitude parameters and using the built in functions to calculate peak amplitude, half width and peak area.

3.5. Statistical Analysis

Animals were randomized for *in vivo* experiments using GraphPad Random Number Generator. Sample size was determined by a priori power calculation using G*Power 3.1.9.2 with mean differences and 20-25% standard deviations based on pilot studies (power 80%, α=0.05). Data were analyzed by GraphPad Prism 7.0 software, unless stated otherwise. Data were assessed for normal distribution using the D'Agostino-Pearson normality test or the Shapiro-Wilk W-test in order to determine parametric or non-parametric analysis. For comparing two or more groups with normal distribution the unpaired t-test with Welch's correction either one-way ANOVA with Dunett's multiple comparison test or two-way ANOVA with Tukey's or Sidak's multiple comparison test was used. For unevenly distributed data, the Mann-Whitney test either one-way ANOVA with Dunett's multiple comparison test or two-way ANOVA with Tukey's or Sidak's multiple comparison test was used. Please, refer to the figure legends and the results section concerning the actual study design.

DOI:10.14753/SE.2023.2742

4. Results

4.1. Microglia establish direct, purinergic contacts with cells of the neurovascular unit that shape CBF at all levels of the cerebrovascular tree

We first studied the anatomy of microglia-vascular interactions using high-resolution microscopic techniques. To examine which segments of the cerebrovascular tree microglia contact, we injected FITC-Dextran into CX3CR1^{tdTomato} microglia reporter mice, which allowed 3D reconstruction of penetrating arterioles in the cerebral cortex down to 600 μm below the dura mater (Figure 9. a). We observed that microglia cover arterial bifurcations at the level of first, second and third order vessels and identified contacting microglial processes at all levels of the cerebrovascular tree (Figure 9. b). The average lifetime of contacts ranged between 5 to 15 min and microglial processes frequently re-contacted the same sites at both arterioles and microvessels, suggesting that specific sites for microglia-vascular interactions may exist in the brain. Next we examined the formation of physical contact between microglia and other cells in the NVU. For this purpose, we used the specific microglial marker P2Y12 receptor (P2Y12R), which is expressed only by microglia in the brain parenchyma (97, 239, 240). Interestingly, we discovered that processes of parenchymal microglia extend beyond glial fibrillary acidic protein (GFAP)-positive astrocytic endfeet at the level of penetrating arterioles directly contacting smooth muscle actin (SMA)-positive VSMCs (Figure 9. c) and endothelial cells in both large vessels and microvessels shown by both confocal laser scanning microscopy (CLSM) and electron microscopy (Figure 9. d-e). 3D analysis of Z-stacks imaged by CLSM demonstrated that 85% of blood vessel segments are contacted by microglial processes and 15% of the endothelial cell surface is covered by microglial processes (Figure 9. f). Besides, electron microscopy revealed that microglial processes directly contact about 83% of pericytes at the level of micovessels (Figure 9. g-h). It's well-known that ATP and ADP represent an important chemotactic signal for microglia sensed by microglial P2Y12R (241). In addition, it has been evidenced that purinergic signaling in endothelial cells and pericytes markedly influences CBF (242). Our previous study revealed that clustering of microglial P2Y12R occurs at sites of somatic ATP release in neurons, through which microglia are able to sense and influence neuronal activity and

DOI:10.14753/SE.2023.2742

mitochondrial function (239). Hence, we investigated whether ATP released at the perivascular compartment could also act as a chemotactic signal for microglial processes. Importantly, our 3D electron tomography analysis revealed that contacting P2Y12R-positive microglial processes are close apposition with endothelial mitochondria while immunogold particles were enriched at the interface (Figure 9. i). Besides, unbiased immunfluorescent analysis showed that the immunfluorescence intensity of TOM20 (mitochondrial marker) is about 214% higher in endothelial cells at microglial contact sites than at the non-contact sites (Figure 9. j-k). Importantly, immunoelectron microscopy also confirmed the direct contact between P2Y12R-positive microglial processes and endothelial cells in the human cerebral cortex (Figure 9. l).

DOI:10.14753/SE.2023.2742

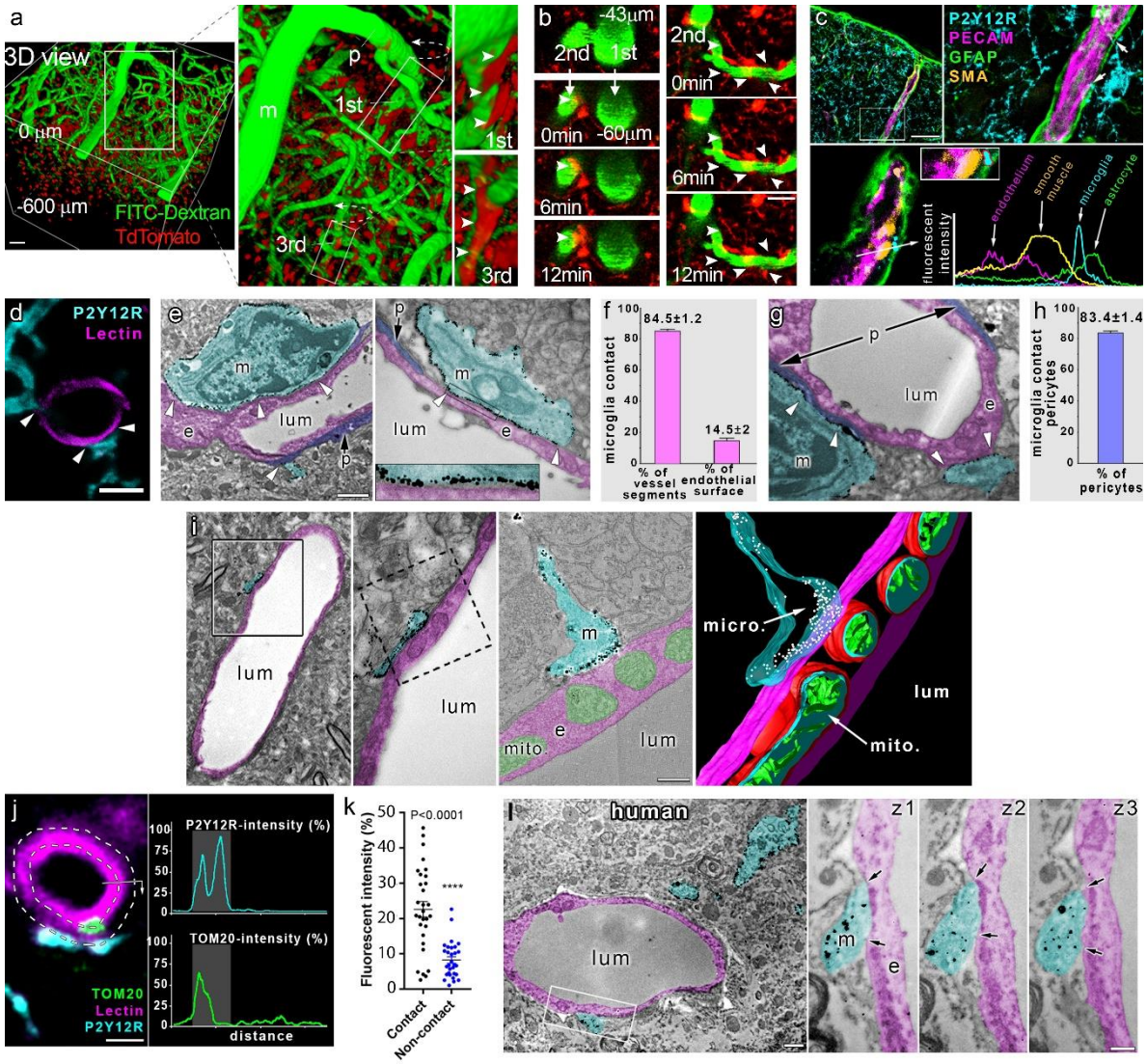

Figure 9. Microglia form dynamic purinergic contacts with the cells of the cerebral vasculature. a) 3D reconstruction of *in vivo* two-photon Z-stacks down to 600 µm below the dura mater shows the cerebral vasculature labeled by i.v. FITC-dextran in the cortex of CX3CR1^{tdTomato} mice. Meningeal (m), penetrating (p), and 1st, 2nd and 3rd order capillaries have been identified for *in vivo* time-lapse imaging. Arrowheads show contacting microglia at different vascular segments. Scale bar.: 50 µm. **b)** *In vivo* two-photon imaging demonstrates that microglial processes (arrowheads) dinamically contact different segments of the cerebrovascular tree (labeled by i.v. FITC-Dextran). Scale bar: 20 µm. **c)** Microglial processes (P2Y12R, cyan) are extended beyond the perivascular astrocytic endfeet (GFAP,

green) and directly contact vascular smooth muscle cells (SMA, yellow) (arrows) at the level of penetrating arteries. Magenta color labels the endothelial cells. Scale bar: 50 μm. **d)** Confocal laser scanning microscopy (CLSM) image shows microglia (P2Y12R, cyan) contact endothelial cells (Tomato lectin, magenta) in the cerebral cortex. Scale bar: 3 μm. **e)** Electron microscopy (EM) images reveal microglia (m, P2Y12R-immunogold labeling, cyan) directly contact endothelial cells (e, magenta) and pericytes (p, purple). (Lum-lumen.) Scale bar: 2 μm. **f)** Frequency of vessels receiving microglial contact, and microglial process coverage of endothelial cell surface. **g)** EM image demonstrates microglia (m, P2Y12R-immunogold labeling, cyan) directly contact pericytes (p, purple). (Lum-lumen.) **h)** 83.4 ± 1.4% of pericytic cell bodies are contacted by microglial processes. **i)** 3D reconstruction of electron tomogram reveales that clustering of anti-P2Y12R-immunogold on microglial processes (m, cyan) directly contacting the endothelium (e, magenta) of an arteriole / post-capillary venule. Left two panels are conventional EM images of the same area on the adjacent ultrathin section. The right panels show tomographic virtual section and 3D reconstruction of the direct contact. (mito.-mitochondria, green; lum-lumen.) Scale bar.: 200 nm. **j)** The process of semi-automated unbiased analysis of fluorescent intensity area for the graph presented in Fig.1k is shown. White dashed lines show the outer and the inner profiles, based on the outline of the endothelial cell. P2Y12R intensity was measured along the outer, TOM20 intensity along the inner profile, starting from the arrow. The intensity values are plotted (right) along the perimeter of the vessel. Contact site (marked by the grey column in the plots) was defined automatically. Scale bar: 2 μm. **k)** Unbiased anatomical analysis demonstrates an enrichment of endothelial mitochondria (TOM20+, green), at sites of microglial contacts (P2Y12R+, cyan). Scale bar.: 2 μm. **l)** EM images show microglia (m, P2Y12R-immunogold, cyan) directly contact endothelial cells (e, magenta) in human neocortex. z1-z3 panels show the contact on three consecutive ultrathin sections, arrows mark the edges of direct membrane contact. Scale bar.: 1 μm on the left panel and 400 nm on z3 (209).

Furthermore, we found that 93% of astrocytes are contacted by P2Y12R-positive microglial processes, whereas microglial cell bodies contact directly only 18% of astrocytes (Figure 10.

DOI:10.14753/SE.2023.2742

a). 3D reconstruction of CLSM image shows microglial processes directly interact with GFAP-positive astrocytic endfoot (arrowheads) and cell body (arrow) (Figure 10. b), and CX3CR1-positive microglial cell body directly contact GFAP-positive astrocyte (Figure 10. c). We used Aquaporin-4 (AQP4) immunostaining to visualize perivascular astrocytic endfeet, surprisingly we observed that microglial processes directly contact endothelial cells at sites where AQP4 signal is missing (Figure 10. d.) or by extending through astrocytic endfeet layer (Figure 10. e). Combined immunogold-immunoperoxidase labeling and electron microscopy confirmed that microglial processes directly contact parenchymal astrocytes and perivascular astrocytic endfeet (Figure 10. f). Importantly, we found similar contacts in the human cerebral cortex from both aged and middle-aged patients who died in non-neurological conditions: P2Y12R-positive microglial processes directly contact both perivascular astrocytic endfeet and endothelial monolayer of small arterioles and capillaries (Figure 10. g-i). Interestingly, we noticed that individual microglia cells contact multiple microvessels and nearby neurons simultaneously in the brain (Figure 10. j). Overall, microglial processes not only directly contact all cells of the NVU along the cerebrovascular tree, which cells are highly implicated in modulation of CBF (5, 75, 89), but simultaneously contact neurons and vascular structures. Hence, microglia are ideally positioned to influence neurovascular responses in the brain.

DOI:10.14753/SE.2023.2742

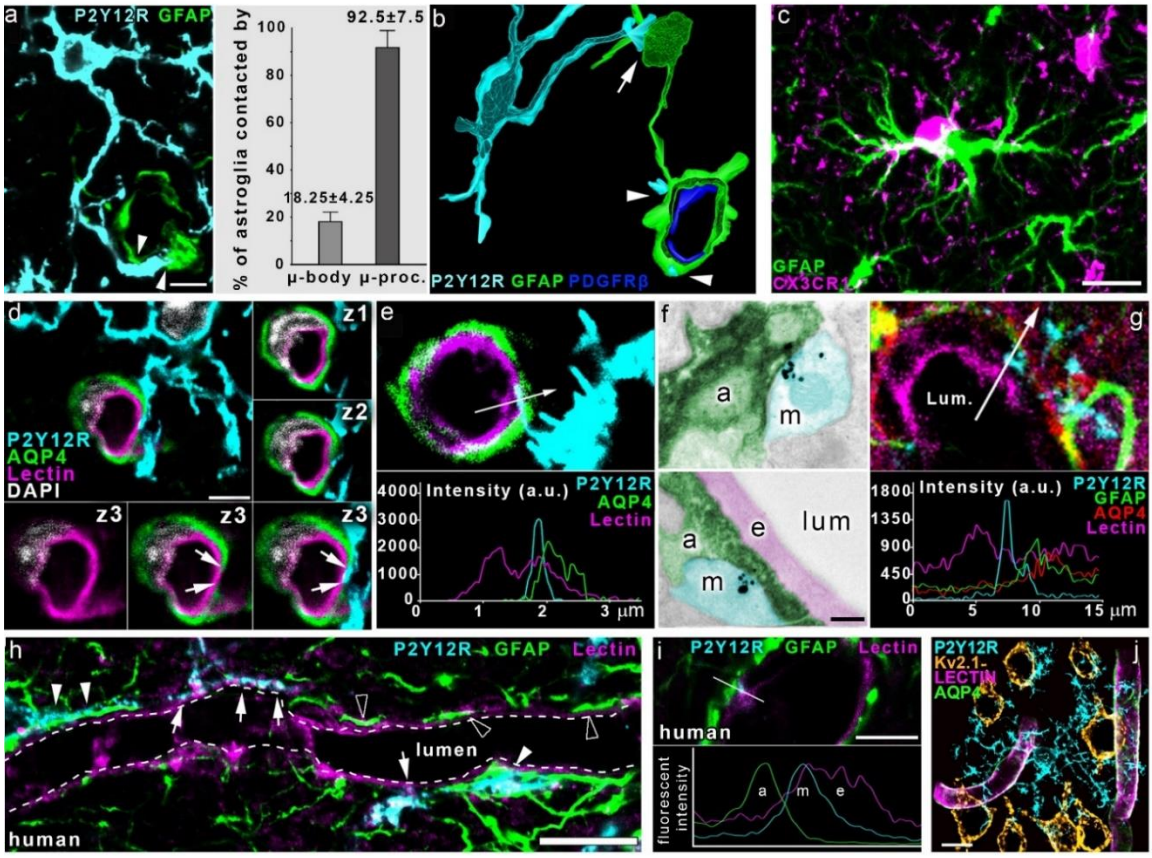

Figure 10. Microglia form direct purinergic contacts with the cells of the neurovascular unit which regulate CBF. a) CLSM image shows microglia (P2Y12R, cyan) contact the cell body of an astrocyte (GFAP labeling, green; arrows) and astrocytic endfeet (arrowheads). 18.25±4.25% of astrocytes contacted by microglial cell body and 92.5±7.5% of astrocytes are touched by microglial processes. Scale bar: 10 μm. **b)** 3D reconstruction of a high resolution CLSM Z-stack shows that microglia (P2Y12R, cyan) contact both astrocytic cell body (GFAP labeling, green, arrow) and astrocytic endfeet (arrowheads) ensheating a capillary. Pericytes are visualized by anti-PDGFRβ labeling (blue). **c)** Microglia (CX3CR1, magenta) are capable to form direct contact by their cell body with astrocytes (GFAP labeling, green) in the cerebral cortex. Scale bar: 10 μm. **d)** CLSM image demonstrates that P2Y12R-positive microglial process (cyan) directly contact perivascular aquaporin-4 (AQP4)-positive astrocyte endfeet (green) and also extends to the endothelial layer (Lectin, magenta) where astrocytic coverage is not present (arrows). z1-z3 panels show the contact area on three consecutive confocal sections. Scale bar: 3 μm. **e)** CLSM image and fluorescent

intensity plots show microglial process extending beyond perivascular astrocytic endfeet to interact with the endothelium. The fluorescent intensity profile plot (measured along the 3.5 um long white arrow) clearly demonstrates the presence of the microglial process under astrocytic endfeet. **f)** EM images show direct contact between microglial (m, cyan) and astrocytic (a, green) processes. (e-endothelial cell, magenta; lum-lumen). Scale bar: 200 nm. **g)** CLSM image and fluorescent intensity plots show microglial processes interacting with GFAP- and AQP4-positive astrocytes in the human brain. The fluorescent intensity profile plot (measured along the 15 μm long white arrow) clearly shows the presence of the microglial process between the endothelium and the perivascular astrocytic endfeet. **h)** CLSM images in human neocortex reveal P2Y12R-positive microglial processes (cyan) contacting perivascular astrocytic endfeet (GFAP, green; white arrowheads) and endothelial cells (tomato-lectin, magenta, white arrows), and astrocytic endfeet directly touching the endothelial monolayer (empty arrowheads). Scale bar: 10 μm. **i)** CLSM image and fluorescent intensity plots show that microglial process (m) directly contact the endothelial layer (e) within the astrocytic layer (a). Scale bar: 5 μm. **j)** CLSM maximal intensity plot demonstrates individual microglial cells (cyan) contacting several microvessels (lectin-magenta, GFAP-green) and neurons (ochre) simultaneously. Scale bar: 10 μm (209).

4.2. Microglia modulate neurovascular coupling via P2Y12R-mediated processes

In our previous studies, we did not find major alterations in the number or morphology of endothelial cells, astrocytes or pericytes after elimination of microglia by CSF1R blockade (176). To study whether the elimination of microglia from the brain by using CSF1 receptor inhibitor, PLX5622 (243) could influence vascular architecture and cerebral metabolism, we have done HMPAO-SPECT and FDG-PET measurements (213, 214). [^{99m}Tc]-HMPAO SPECT and [^{18}F]-FDG PET are non-invasive methods, which assess regional CBF and glucose metabolism changes, respectively. We did not find significant difference between control and microglia-depleted mice regarding HMPAO and FDG uptake in any brain areas (Figure 11. a-c).

DOI:10.14753/SE.2023.2742

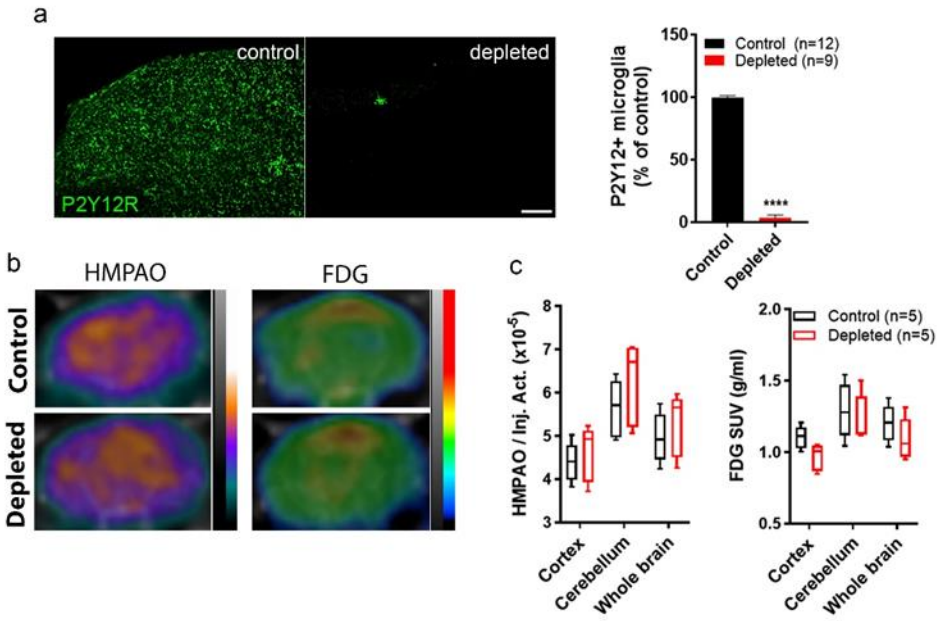

Figure 11. Microglia depletion does not disrupt cerebal perfusion or metabolism. a) Feeding male C57BL/6J mice with a chow diet containing PLX5622, a specific CSF1R inhibitor leads to an almost complete (97%) elimination of resident microglia as evidenced by the numbers of P2Y12R-positive cells in the cerebral cortex. Data are expressed as mean ± SEM. n=12 control and n=9 depleted mice per group, ****p<0.0001 control versus depleted, unpaired t-test with Welch's correction. Scale bar: 100 μm. **b-c)** Representative [99mTc]-HMPAO SPECT and [18F]-FDG PET images of control and microglia-depleted mice. Proportion of measured and injected HMPAO activity and standard uptake values (SUV) of FDG are shown. Atlas-based region of interest analysis (b) shows no significant differences between the normalized regional uptake values (c) of the two groups. Data are expressed as mean ± SEM. n=5 control and n=5 depleted mice, two-way ANOVA followed by Sidak's multiple comparison test (209).

DOI:10.14753/SE.2023.2742

4.2.1. Selective elimination of microglia or P2Y12R blockade leads to decreased neurovascular coupling response

To investigate the role of microglia in CBF response to physiological stimuli, we turned to the commonly used whisker-stimulation model to study the mechanisms of neurovascular coupling (244). To this end, we measured CBF changes in response to a series of whisker stimulations in the barrel cortex using laser speckle contrast imaging (LSCI), optimized to assess changes in the microcirculation through the intact skull bone in real-time in mice (226). Whiskers on the left side were stimulated under mild ketamine-medetomidine sedation, allowing stable and reproducible CBF responses to be observed (Figure 12. a). Interestingly, we found that in the absence of microglia NVC is impaired evidenced by that CBF responses to whisker stimulations are significantly decreased in depleted-mice compared to that seen in controls (10 series of stimulations for 15s each). (Figure 12. b). Besides, to test whether the microglial P2Y12R could be involved in modulating NVC, we measured CBF responses to whisker stimulation in P2Y12R KO mice. We found decreased CBF response to whisker stimulation in P2Y12R KO mice compared to control mice (Figure 12. b). To confirm the role of microglia in neurovascular coupling with an alternative approach, we repeated measurements of CBF changes to whisker stimulation in the barrel cortex using functional ultrasound (fUS), which detects hemodynamic changes in the brain based on cerebral blood volume (CBV) (245). This technique combines high spatiotemporal resolution with deep tissue penetration, which enables non-invasive whole-brain imaging through the skull in mice. We found that in the absence of microglia CBV increases in response to whisker stimulation in the contralateral barrel cortex are significantly smaller compared to that seen in control mice (Figure 12. c-e).

DOI:10.14753/SE.2023.2742

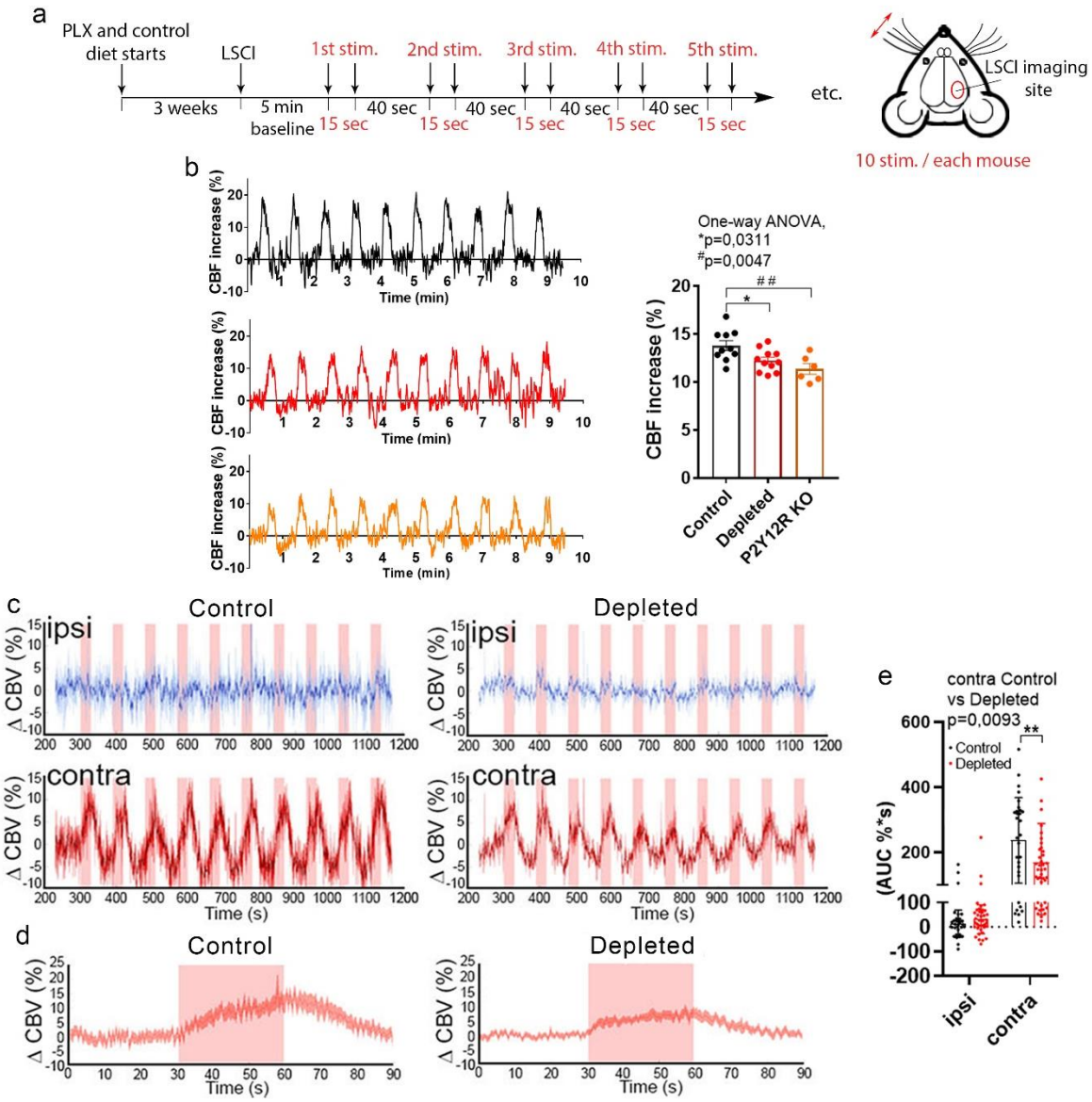

Figure 12. The absence of microglia or microglial P2Y12R leads to impaired NVC response. a) Protocol of electromechanically controlled whisker stimulation. Male C57BL/6J mice were fed with PLX5622 for 3 weeks to eliminate microglia from the brain. **b)** Representative CBF traces and quantification show significantly decreased CBF response to whisker stimulation in the absence of microglia and in P2Y12R KO mice compared to control ones. n=10 control, n=11 depleted and n=6 P2Y12R KO mice, one-way ANOVA followed by Dunnett's multiple comparison test *p=0.0311 control vs depleted, **p=0.0047 control vs P2Y12R KO. **c**) Functional ultrasound (fUS) imaging also show reduced CBV

responses in microglia-depleted mice as compared to controls in the ipsilateral (ipsi) and contralateral (contra) barrel cortex. Representative traces of 10 subsequent stimulations (30s each) are shown for control and microglia-depleted mice. **d**) Peak trace averages of the contralateral hemisphere in control and depleted mice, with 95% confidence intervals. **e**) Averaged area under the curve (AUC) distribution for each group, as presented in pink window on panel d). n=30 and n=40 stimulations from 3 control and 4 depleted mice, respectively, **p=0.0093, two-way ANOVA followed by Sidak's multiple comparisons test. Data are presented as mean ± SEM (209).

To exclude the possible compensatory mechanisms of genetic manipulation, we blocked microglial P2Y12R selectively in the brain by injecting a specific P2Y12R inhibitor, PSB0739 into the cisterna magna 40 minutes prior to LSCI measurements (Figure 13. a). Effective blockade of microglial P2Y12R by PSB0739 injected into the cisterna magna has also been characterized in detail in our previous study (239). We found markedly smaller CBF response to whisker stimulation in PSB0739-injected mice compared to control ones (Figure 13. b-c). In the brain only microglia express P2Y12R (239, 240), this way we could also validate the specificity of microglial actions on CBF responses.

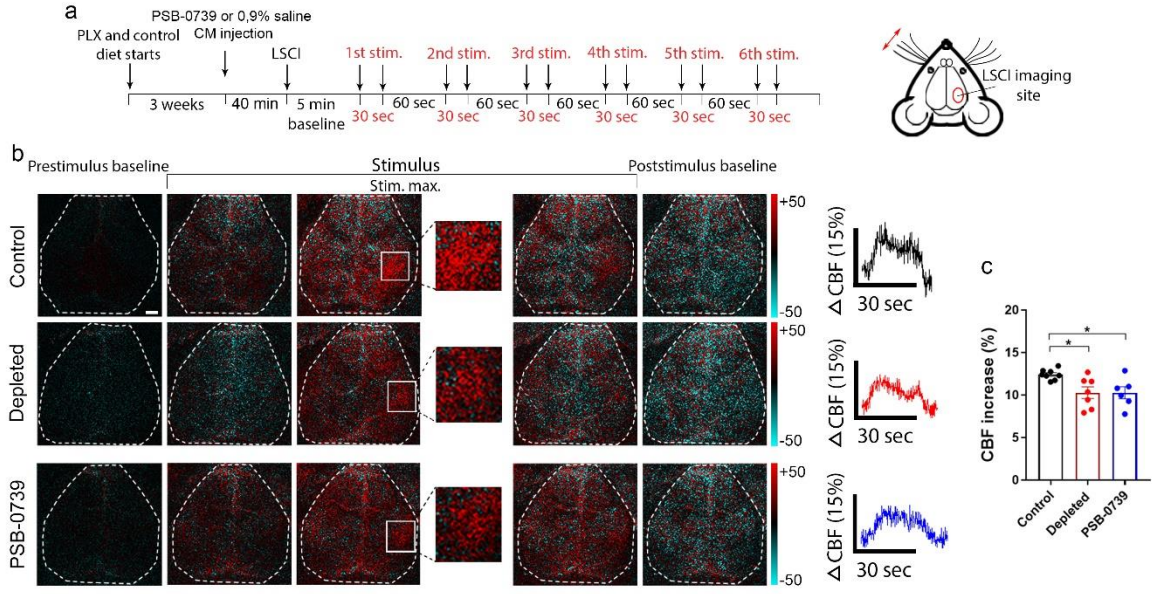

Figure 13. Acute blockade of microglial P2Y12R results in reduced NVC response. a) The schematic of the experimental protocol. Mice were injected either with saline (control

and depleted) or with PSB0739 into the cisterna magna 40 min before LSCI measurements. CBF changes to whisker stimulation were examined in the contralateral barrel cortex. **b)** Representative difference images demonstrate CBF changes in the contralateral barrel cortex relative to baseline in response to whisker stimulation before, during and after stimulus (white rectangle shows the contralateral barrel cortex). Time course of stimulus-evoked CBF responses is presented on the right side of panel b. **c)** Microglia depletion or acute blockade of microglial P2Y12R decrease the maximum of evoked CBF responses compared to the control. n=7 control, n=7 depleted and n=6 PSB0739-injected mice, one-way ANOVA followed by Dunnett's multiple comparison test (*p=0.0191 control vs depleted, *p=0.0243 control vs PSB0739) (209).

4.2.2. Nitric oxide synthase blockade by L-NAME in the absence of microglia results in additional decrease in CBF response to whisker stimulation

Given the pivotal roles of NO in vasodilation, and specifically in neurovascular coupling (5, 75), we investigated whether NO could be involved in microglia-mediated CBF modulation. To this end, we studied the relationship between microglia depletion and nitric-oxide synthase (NOS) blockade by L-NAME. Surprisingly, we observed that both microglia depletion and L-NAME markedly reduced the CBF response to whisker stimulation compared to control mice, whereas L-NAME administration into microglia-depleted mice resulted in additional CBF decrease compared to microglia-depleted or L-NAME injected mice (Figure 14.). These findings suggest that in addition to microglial modulation of vasodilation in response to somatosensory stimulation, a microglia-independent NO-based component is also involved. Overall, these results show that microglia- and microglial P2Y12R-mediated actions are important to maintain normal blood flow responses to somatosensory stimulation in the cortical microcirculation, which is partially independent of NO.

DOI:10.14753/SE.2023.2742

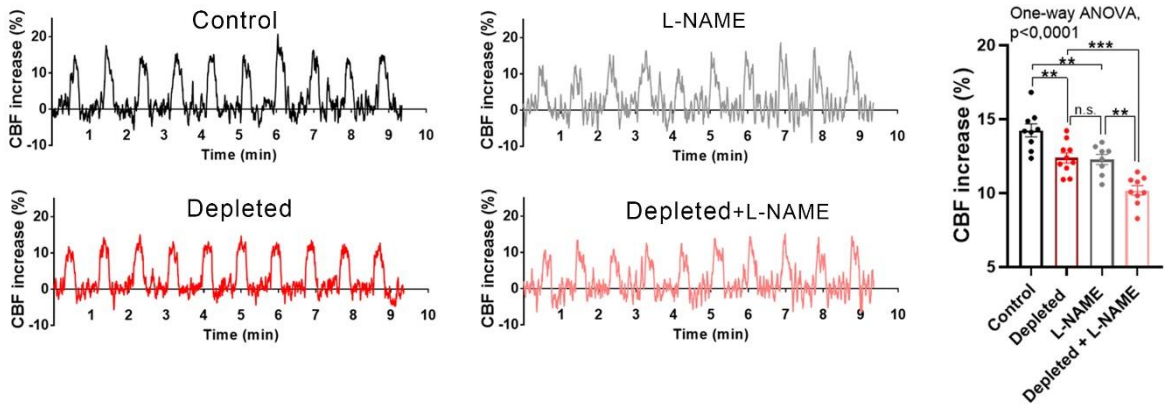

Figure 14. Nitric oxide synthase blockade by L-NAME in the absence of microglia leads to additional CBF decrease in response to whisker stimulation. Representative CBF traces and graph demonstrates changes in neurovascular coupling response in L-NAME-treated mice both in the presence and the absence of microglia. n=9 control, n=10 depleted, n=8 L-NAME treated, n=9 L-NAME treated depleted mice, ****p<0.0001, one-way ANOVA followed by Tukey's multiple comparison test (**p=0.005 control vs depleted, **p=0.0049 control versus L-NAME, **p=0.0026 L-NAME vs depleted + L-NAME, ***p=0.0008 depleted versus depleted + L-NAME) (209).

4.3. Increased neuronal activity in the barrel cortex induced by whisker stimulation does not explain altered CBF responses after microglia manipulation *in vivo*

To examine whether substantial shifts in neuronal responses to whisker stimulation could explain the effect of microglia manipulation on neurovascular coupling, we repeated whisker stimulation experiments while recording neuronal activity in the barrel cortex, either using chronically implanted tetrode electrodes or *in vivo* two-photon calcium imaging. We isolated n=42, n=41 and n=61 putative single units from 2 electrophysiological recordings of each control, microglia-depleted and P2Y12R KO mice, respectively (n = 5). Thus we could investigate the baseline firing rates in the stimulus-free periods as well as stimulus-induced firing responses of individual neurons. We observed markedly increased baseline firing rates of barrel cortex neurons in both microglia-depleted and P2Y12R KO mice compared to

control ones (Figure 15. a-d). We did not find significant differences in the extent of stimulus-evoked neuronal responses between experimental groups (Figure 15. e).

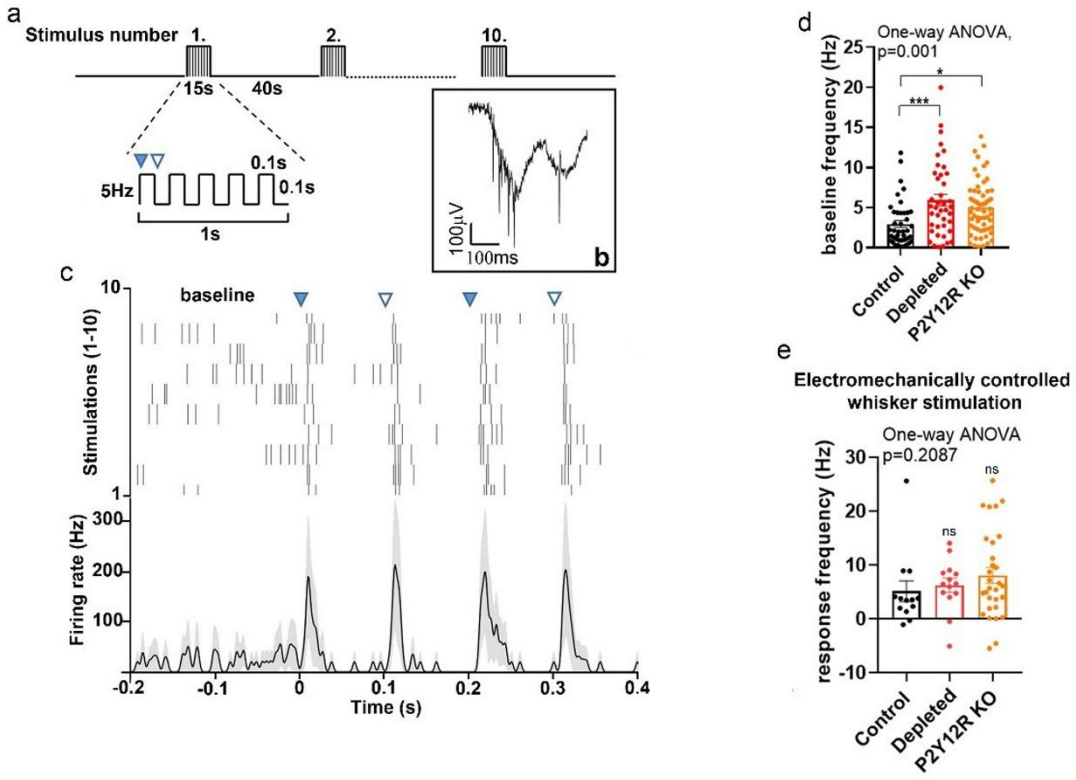

Figure 15. Electrophysiological measurements revealed that whisker stimulation-induced neuronal responses in the barrel cortex do not explain altered CBF responses after microglia manipulation. a) The schematic of the experimental protocol. Whiskers were stimulated electromechanically with 5 Hz, causing alternating passive deflections of the vibrissae in the anterior and posterior directions (filled and empty arrowheads, respectively) for 15s, followed by a 40s break, repeated 10 times. **b)** Raw tetrode data demonstrating extracellular spikes recorded from the barrel cortex. **c)** Representative plot and histogram about a single neuron activated by passive whisker deflections. Top, raster plot aligned to whisker stimulation onset (black ticks, individual action potentials). Bottom, peri-stimulus time histogram represents of the mean firing responses of the same neuron (shading, SEM). **d)** Baseline firing rates were markedly higher in depleted and P2Y12R KO mice compared to control ones. n=4 control, n=3 depleted and n=5 P2Y12R KO mice, **p=0.001, one-way ANOVA with Dunett's multiple comparisons test (***p<0.006 control vs depleted,

*p=0.0109 control vs P2Y12R KO). **e)** Stimulus-induced firing rate changes were comparable across controls and microglia-depleted mice using electromechanically controlled whisker stimulation. Data are shown as baseline corrected response frequency (for corresponding baseline frequencies, mean ± SEM), n=4 control, n=3 depleted and n=5 P2Y12R KO mice, p=0.2087 and p=0.6391, Kruskal-Wallis test with Dunn's multiple comparisons test (209).

To confirm our observations, we repeated whisker stimulation experiment using *in vivo* two-photon microscopy with stimulations performed two times with 40s breaks (Figure 16. a). For analysis we selected those barrel cortex neurons which specifically responded to whisker stimulation. Our results demonstrated that somatosensory stimulus-induced increases in the neuronal GCaMP6s signal in Thy1-GCaMP6s mice did not show significant differences between control and microglia-depleted mice (Figure 16. b). Thus, while the absence (PLX5622 depleted) or dysfunction (P2Y12R KO) of microglia may shift baseline neuronal activity as expected (140, 239), stimulus-evoked neuronal responses do not explain the marked differences in CBF changes observed after microglia manipulation.

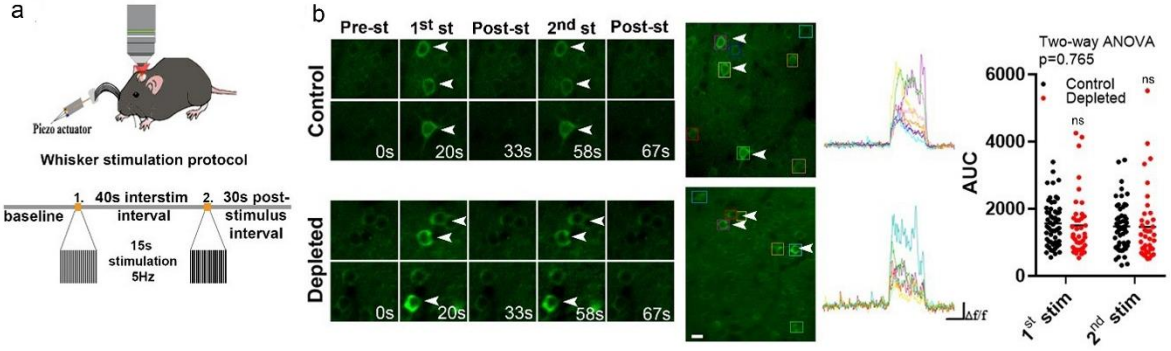

Figure 16. ***In vivo*** **two-photon imaging revealed that whisker stimulation-evoked neuronal responses in the barrel cortex do not explain altered CBF responses after microglia manipulation. a)** Schematic outlines of the whisker stimulation protocol used for *in vivo* two-photon $[Ca^{2+}]_i$ imaging in the barrel cortex of Thy1-GCaMP6s mice. **b)** Representative images demonstrate stimulus-evoked neuronal intracellular $[Ca^{2+}]$ responses with individual traces of neurons marked with rectangles during baseline imaging, 15s

stimulation and after stimulation. Graph shows AUC (area under the curve) values of neuronal GCaMP6s signal changes in response to the 1st and 2nd electromechanically controlled whisker stimulation in control and microglia-depleted mice. n=4 mice per group, n=56 neurons from control and n=40 neurons from depleted mice from two trials, p=0.765, two-way ANOVA with Sidak's multiple comparisons test. Scale bar: 20 μm. Data are presented as mean ± SEM (209).

4.4. Real-time chemogenetic activation of microglia leads to impaired neurovascular coupling response

4.4.1. Chemogenetic activation of microglia results in increased intracellular Ca^{2+} levels in vitro

To investigate the effect of real-time chemogenetic microglia manipulation on CBF changes, we generated a novel mouse line by crossing cre-dependent hM3Dq DREADD mice with CX3CR1-CreERT2 mice (99), named as MicroDREADD^{Dq} mice. Tamoxifen (TMX) administration resulted in specific recombination in 95.3% of microglia (Figure 17. a). At first we carried out *in vitro* experiments to investigate the responsiveness of microglia cells to DREADD agonists. To this end, we administered hM3Dq DREADD agonists 1μM clozapine-N-oxide (CNO) or 1μM Compound 21 (C21) (246) to tamoxifen-treated and untreated microglia cells derived from MicroDREADD^{Dq} mice. We found that CNO or C21 induced rapid increases in intracellular calcium levels in microglia derived from MicroDREADD^{Dq} mice, which was completely absent in TMX-untreated cells (Figure 17. b-g). Interestingly, we observed that microglia show reduced calcium responses to repeated C21 stimulations and decreased responsiveness to single administration of 10 μM ATP (Figure 17. c-g).

DOI:10.14753/SE.2023.2742

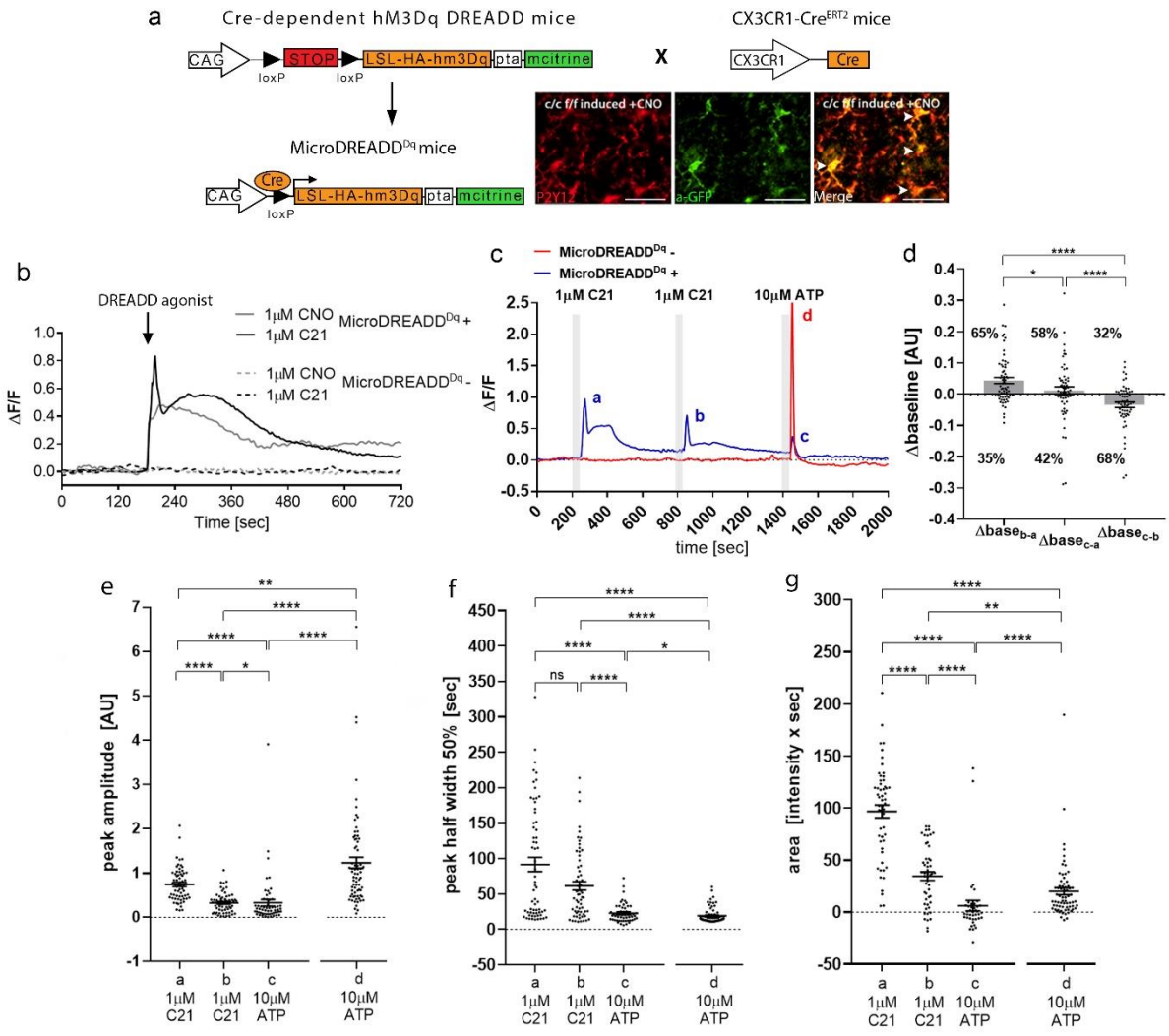

Figure 17. Microglial cells expressing DREADD (hM3Dq) respond to DREADD agonist C21 with a biphasic Ca^{2+} response and reduced ATP responsiveness. a) Shematic represents the generation of a novel chemogenetic mouse model. Tamoxifen (TMX)-induced recombination was confirmed by anti-P2Y12R and anti-GFP (mCitrine) double staining (white arrowheads) on brain slices, which enables chemogenetic activation of microglia by DREADD agonists such as CNO and C21. Scale bar: 50 µm. **b)** Representative ΔF/F calcium traces of cultured MicroDREADD^{Dq} microglia cells responding to CNO or C21 treatment. **c)** Representative calcium signals of cultured MicroDREADD^{Dq+} and MicroDREADD$^{Dq–}$ microglia cells repeatedly exposed to 1µM C21 and 10µM ATP for 1 min. **d)** Differences of average baseline values determined within 50 sec prior to the onset of the calcium responses.

e-g) Peak amplitudes (e), half width values (f) and peak areas (g) of *a*, *b*, *c* and *d* peaks labelled in the line graph d). n=64 for MicroDREADD^{Dq+}, n=73 for MicroDREADD^{Dq-}; Mann-Whitney test, ****p<0.0001; **p<0.01; *p<0.05 (d-g) (209).

4.4.2. Chemogenetic stimulation of microglia leads to reduced microglial process motility in vitro and altered microglial morphology in vivo

Next, we studied the effect of chemogenetic microglia activation on process motility and morphology. We observed that single chemogenetic activation led to the blockade of microglial process motility within a few minutes (Figure 18. a-b**)**, while microglia showed reduced calcium responses to repeated C21 stimulations (Figure 17. c-g). Besides, we found that repeated C21 stimulations significantly impaired Ca^{2+} responses of MicroDREADD^{Dq} microglia to 10μM ATP (Figure 17. c, and Figure 18. c-e), suggesting that chemogenetic priming of microglia disables the recruitment of microglial processes to ATP released in the NVU during NVC. Furthermore, chemogenetic stimulation also lead to altered microglial morphology and branch structure *in vivo* as shown by automated, unbiased analysis of microglial cell volume (CellVol), soma volume (SomaVol), branch volume (branchVol), ending nodes and branching nodes (Figure 18. f).

DOI:10.14753/SE.2023.2742

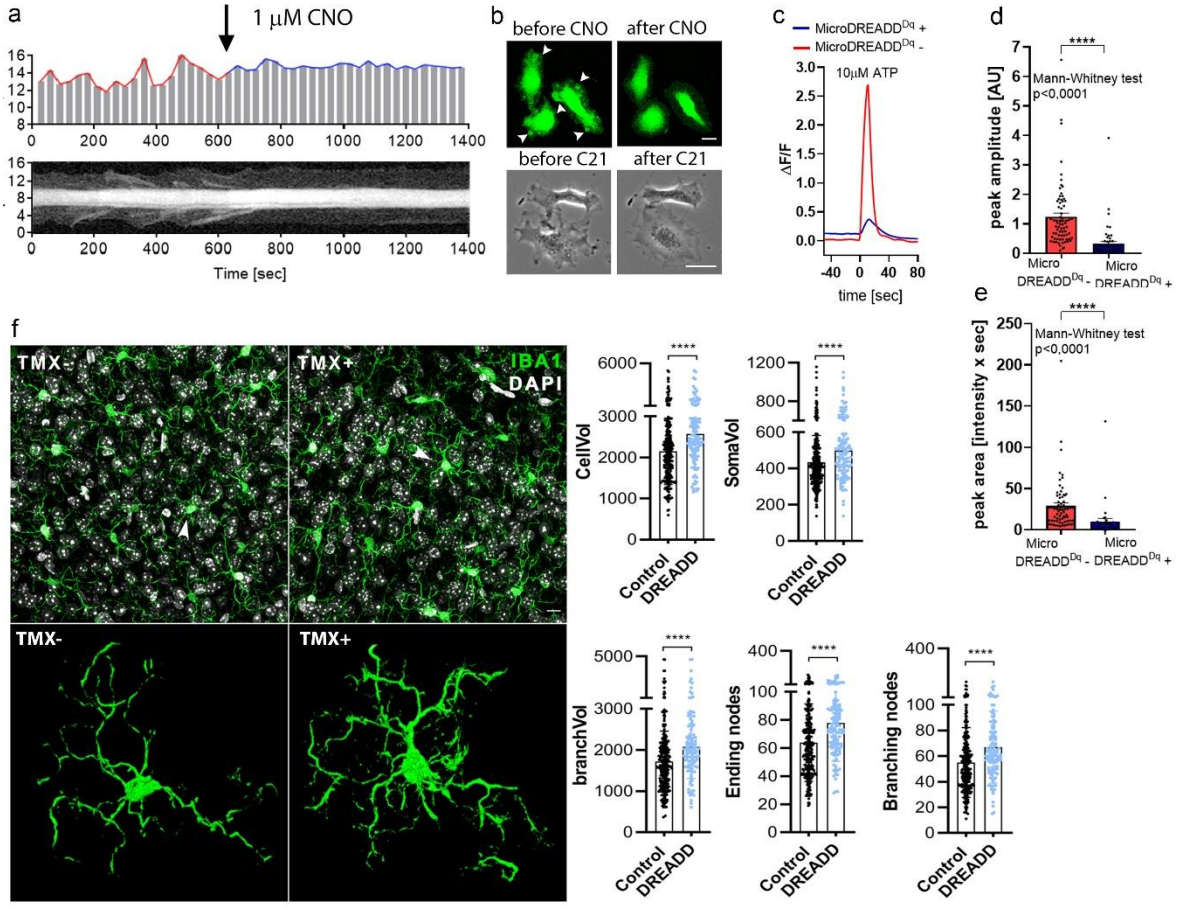

Figure 18. Chemogenetic modulation of microglial activity leads to decreased process motility *in vitro* altered microglial morphology *in vivo*. a-b) The kymogram (a) and fluorescent/phase contrast images (b) taken from time lapse sequences show that cell membrane ruffling is ended in response to DREADD agonists treatment and the cells acquire a flattened morphology. Scale bars: 5 μm on the upper panel, 10 μm on the lower panel. **c-e)** Analyses of calcium curves shows attenuated responsiveness to ATP in MicroDREADD^{Dq+} cells which previously responded to DREADD agonist C21. n=64 for MicroDREADD^{Dq+}, n=73 for MicroDREADD^{Dq-}, ****p<0.0001, Mann-Whitney test (d-e). **f)** Automated, unbiased analysis reveals significant morphological changes in MicroDREADD^{Dq+} microglia in TMX-treated mice 1 hour after intraperitoneal injection of CNO, compared to control mice in which hM3Dq DREADD expression was not induced with TMX. n=275 control (MicroDREADD^{Dq-}) and n=122 DREADD (MicroDREADD^{Dq+}) microglia from n=3-3 mice were analysed. Mann-Whitney test, ****p<0.0001 for cell volume (CellVol), soma volume

(SomaVol), branch volume (branchVol), ending nodes and branching nodes. Scale bar: 20 μm. Data are expressed as mean ± SEM (209).

4.4.3. Chemogenetic activation of microglia induces microglial intracellular Ca^{2+} fluctuations and transient retraction of perivascular microglia processes in vivo

Next, we investigated microglial calcium dynamics and the effect of chemogenetic activation of microglia *in vivo*. To this end, we crossed MicroDREADD^{Dq} mice with cre-dependent CGaMP5g-tdTomato mice (i.e. both constructs could be induced by tamoxifen using the same CX3CR1-CreERT2 driver line). Surprisingly, our *in vivo* two-photon imaging study revealed that microglial processes interacting with arterioles and microvessels in the cerebral cortex showed dynamic calcium fluctuations (Figure 19. a). Chemogenetic activation in MicroDREADD^{Dq} × CGaMP5g–tdTomato mice led to an increase in microglial somatic CGaMP5g signal within 15-30 min, resulting in temporary detachment and withdrawal of a population of perivascular microglial processes (Figure 19. a). In addition, we observed that 1 hour after chemogenetic activation, microglial process coverage of endothelial cells and smooth muscle cells are markedly increased, which could be likely a compensatory response, whereas process coverage of pericytes did not alter significantly as shown by analysis of immunofluorescent CLSM images (Figure 19. b).

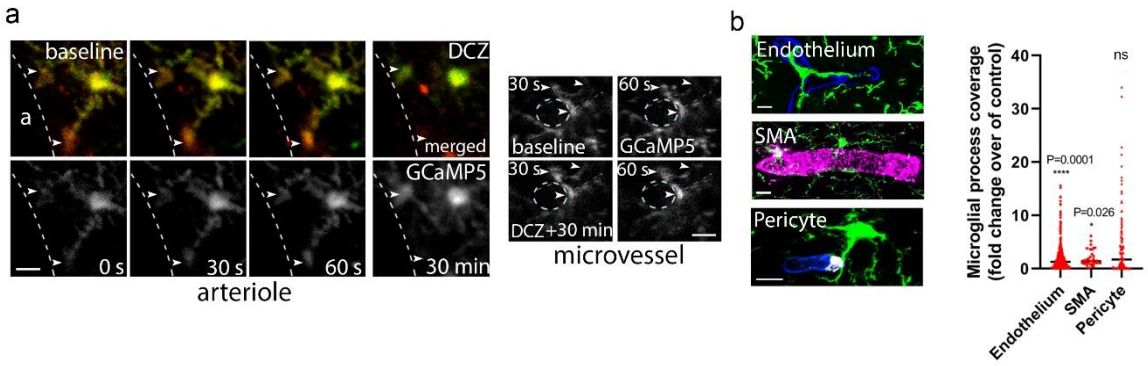

Figure 19. Chemogenetic modulation of microglial activity induces microglial intracellular Ca2+ fluctuations and transient retraction of perivascular microglia processes *in vivo*. a) Microglial processes contacting with blood vessels show dynamic

intracellular [Ca^{2+}] fluctuations (arrowheads) in the cerebral cortex of MicroDREADD^{Dq} x CGaMP5g-tdTomato mice *in vivo*. Microglial calcium responses were studied before (baseline) and 30 min after intraperitoneal injection of the DREADD agonist DCZ around arterioles (a, lumen of the arteriole is shown) and microvessels (n= 4 mice). Scale bar: 10 μm. **b)** 1 hour after chemogenetic activation of microglia, microglial process coverage (Iba1, green) of endothelial cells (lectin, blue), vascular smooth muscle cells (SMA, magenta) and pericytes (PDGFRb, white) were analyzed on perfusion fixed brain slices. Scale bar: 10 μm. n=263 blood vessels, n=66 SMA-positive vessels and n=291 pericytes were measured from n=3 mice, ****p=0.0001 endothelium vs control and *p=0.026 SMA vs control, Mann-Whitney test (209).

4.4.4. Chemogenetic modulation of microglial activity results in impaired neurovascular coupling in vivo

To study the effect of chemogenetic modulation of microglia on NVC, we measured CBF changes in response to whisker stimulation by LSCI 30 minutes after administration of CNO to MicroDREADD^{Dq} and control mice (Figure 20. a). Importantly, we found that chemogenetic activation of microglia lead to a similar degree of CBF reduction to whisker stimulation (Figure 20. a-b) as seen after microglia depletion (Figure 12. b, Figure 13. c, Figure 14.).

DOI:10.14753/SE.2023.2742

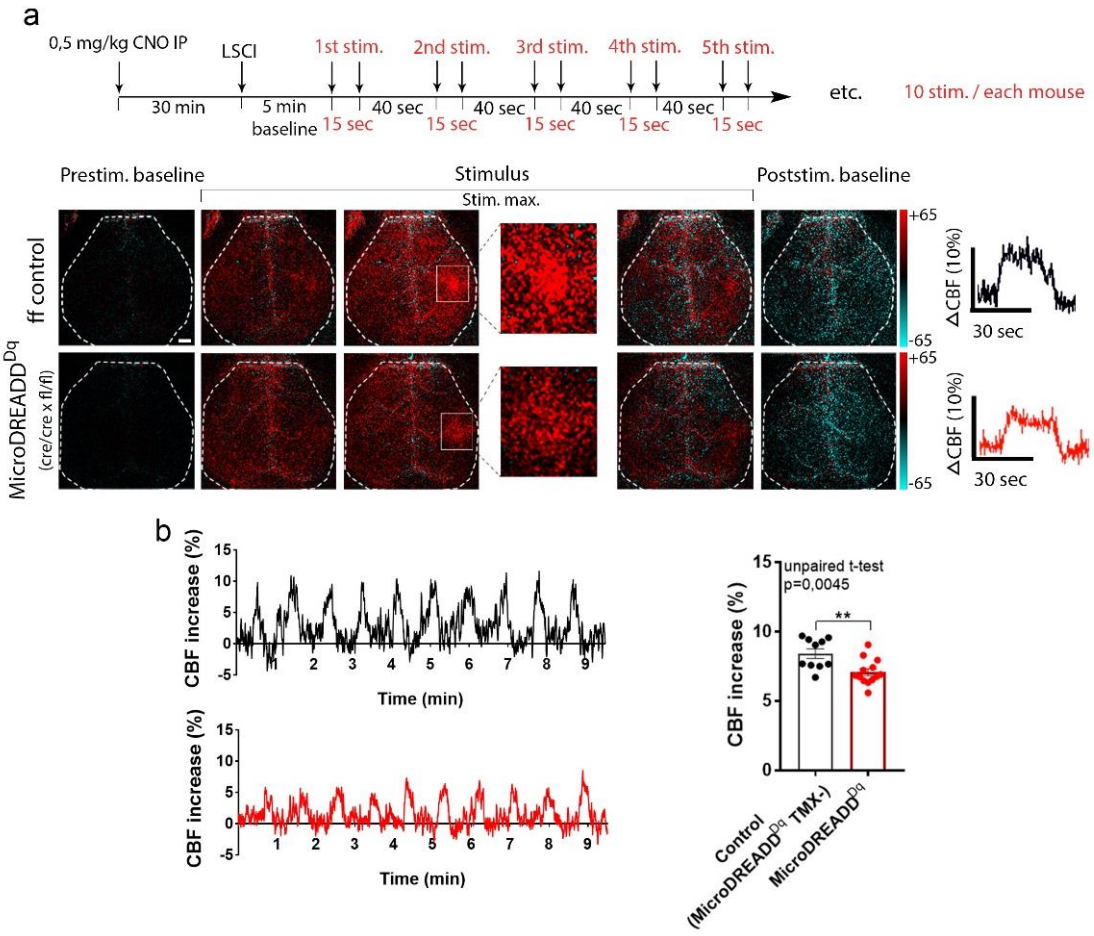

Figure 20. Chemogenetic activation of microglia leads to decreased CBF response to whisker stimulation. a) Schematic of experimental protocol. 6 weeks after TMX and 30 min after a single intraperitoneal CNO injection, CBF were measured during whisker stimulations in MicroDREADD^{Dq} and control mice by LSCI. Representative difference images demonstrate CBF changes relative to baseline in control and MicroDREADD^{Dq} mice (white rectangle shows the area of barrel cortex). Representative stimulus-evoked response curves are shown in the right of panel a. Scale bar: 1 mm. **b)** Representative traces of evoked CBF responses to electromechanically controlled whisker stimulation measured by LSCI. The maximum of evoked CBF responses show a significant decrease in MicroDREADD^{Dq} mice compared to control mice. n=10 control and n=13 MicroDREADD^{Dq} mice, **p=0.0045, unpaired t-test. Data are presented as mean ± SEM (209).

DOI:10.14753/SE.2023.2742

4.5. Microglia modulate hypercapnia-induced vasodilation via P2Y12R signaling

4.5.1. Hypercapnia triggers changes in microglial process morphology and dynamics measured by in vivo two-photon microscopy

To further study the mechanisms through which microglia modulate CBF, we performed hypercapnic challenge, an established vascular trigger inducing vasodilation globally in the brain independently of direct neuronal stimulation. Previous studies demonstrated that hypercapnia induces primarly endothelium-driven vasodilation including actions of astrocytes and other cells (66, 69, 247, 248). At first we studied microglial process morphology and dynamics changes in response to hypercapnia real-time using *in vivo* two photon microscopy. We observed that a population of dynamic microglial processes readily changed their morphology both at arterioles and microvessels in response to vasodilation induced by 2 minutes inhalation of 10% CO_2 under normoxic conditions (Figure 21. a-b). Besides, we found that around arterioles, microglial processes dynamically contact SR101-labeled perivascular astrocytic endfeet (Figure 21. c) and the number of contacting phylopodia at the end of microglial processes markedly increased in response to hypercapnic challenge (Figure 21. c). Next, we investigated microglial process dynamics in $CX3CR1^{CGaMP5g\text{-}tdTomato}$ mice with *in vivo* two-photon imaging and we found that perivascular microglia respond rapidly (within 1-2 min) to hypercapnia with calcium pulses, which was observed in both large processes and phylopodia (Figure 21. d). These results confirm the rapid effect of hypercapnia on microglial process morphology and dynamics.

DOI:10.14753/SE.2023.2742

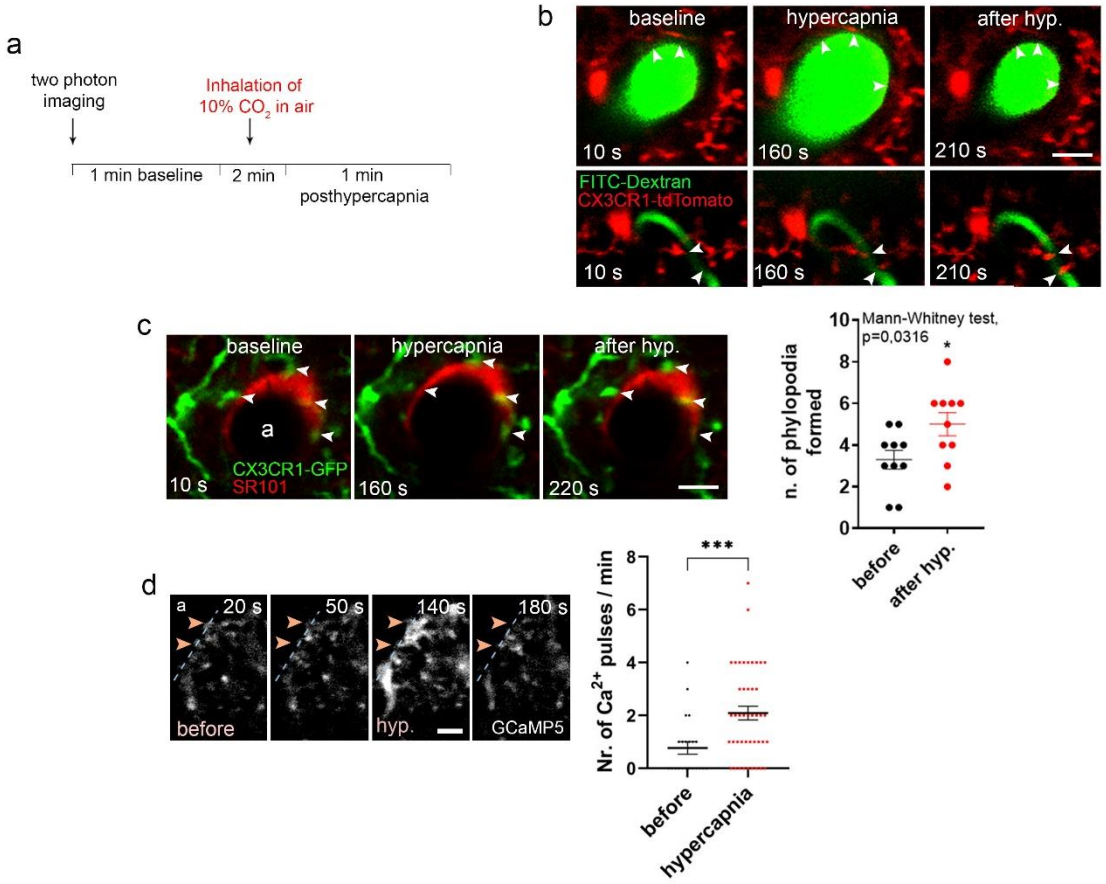

Figure 21. Hypercapnia induces changes in microglial process morphology and dynamics. a) Outline of hypercapnic challenge protocol for two-photon microscopy. After recording 60 seconds of baseline, vasodilation was induced by inhalation of 10% CO_2 in air for 120 seconds (61-180 s) under normoxic conditions, followed by 60 seconds of post-hypercapnia recording. **b)** *In vivo* two-photon resonant (32Hz) imaging of hypercapnia-induced vasodilation was performed in the somatosensory cortex of $CX3CR1^{tdTomato}$ mice. FITC-Dextran was injected intravenously to visualize vessels. The middle panel represents the maximal vasodilation evoked by hypercapnia. Arrowheads show contacting microglial processes around vessels. Scale bar: 20 µm. **c)** Hypercapnia-induced vasodilation was imaged using *in vivo* two-photon microscopy in $CX3CR1^{GFP/+}$ mice after intracortical injection of SR101 to label astrocytes. Graph shows that the number of phylopodia formed at the end of contacting microglial processes (arrowheads) significantly increased after hypercapnic challenge. n=5 mice, *p=0.0316, Mann-Whitney test. Scale bar: 20 µm. **d)**

DOI:10.14753/SE.2023.2742

Perivascular microglia respond rapidly to hypercapnic challenge with intracellular [Ca^{2+}] pulses in small (arrowheads) and large processes as measured in CX3CR1$^{CGaMP5g\text{-}tdTomato}$ mice. Individual processes were followed with *in vivo* two-photon resonant (31Hz) imaging. Scale bar: 10 μm. n=4 mice, ***p=0.001, Mann-Whitney test (209).

4.5.2. Hypercapnia-induced vasodilation is impaired in the absence of microglia in vivo

Next, we studied hypercapnia-induced vasodilation in the absence of microglia *in vivo*. Importantly, we found that hypercapnia-induced vasodilation is significantly impaired in meningeal and penetrating arteries in microglia-depleted mice assessed by *in vivo* two photon microscopy (Figure 22. a), which paralleled markedly decreased CBF response to hypercapnia as measured by LSCI (Figure 22. b-d). To exclude the potential effect of alpha2 adrenergic blockade via the cardiovascular system during ketamine-medetomidine anesthesia (249), we repeated hypercapnic challenge after the administration of atipamezole, an alpha2 receptor antagonist (250). We found that hypercapnia-induced CBF response was similarly impaired in microglia-depleted mice compared to control ones in the presence of atipamezole (Figure 22. e). To validate hypercapnia blood samples were taken from the femoral artery before and after hypercapnic challenge and blood gas tensions were measured. Besides, we investigated the effect of microglia depletion on blood gas tensions and pH. Importantly, we did not find significant difference in baseline and hypercapnia-induced arterial pCO2, pO2 levels and pH between microglia-depleted and control mice (Figure 22. f).

DOI:10.14753/SE.2023.2742

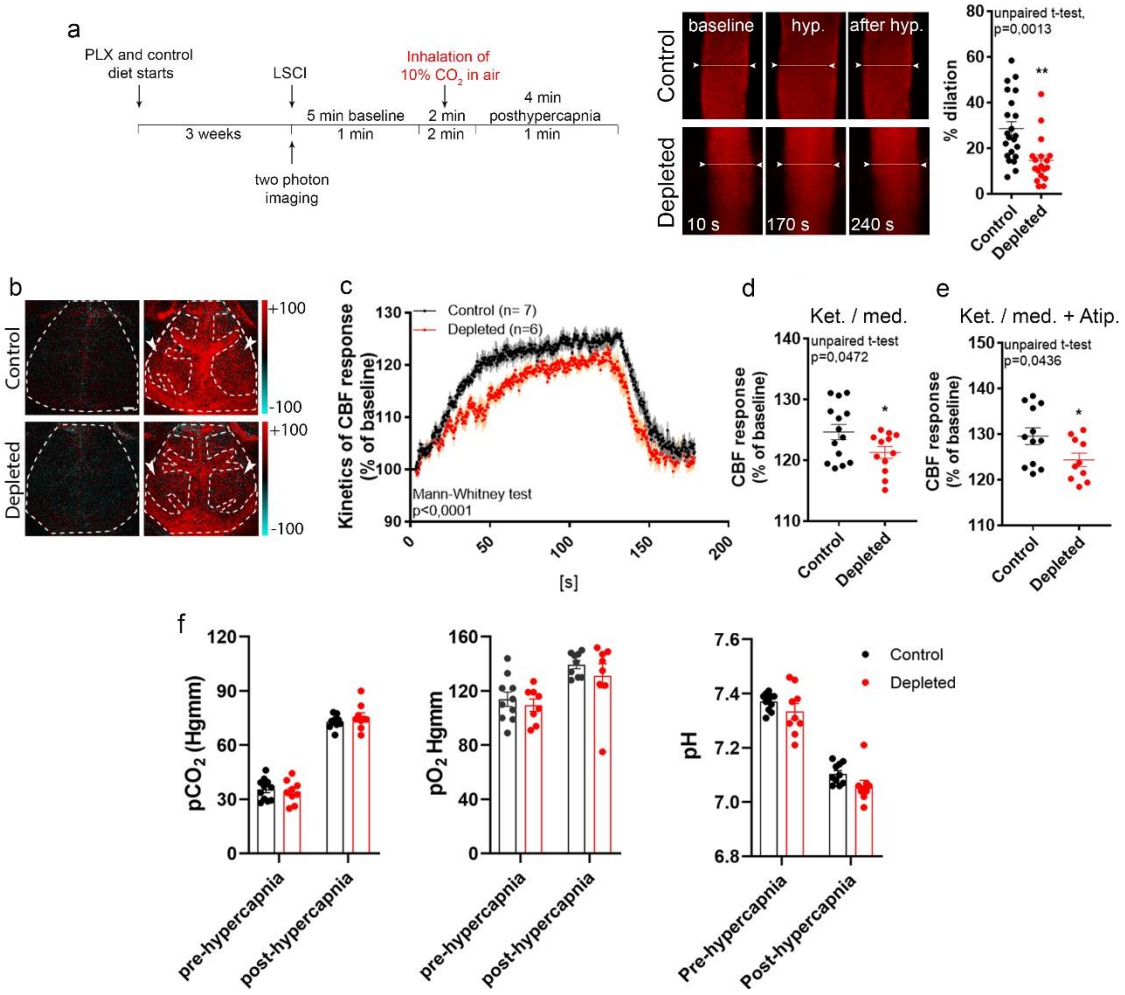

Figure 22. In the absence of microglia hypercapnia-evoked CBF response is significantly decreased. a) Outline of the hypercapnic challenge protocol for *in vivo* two-photon microscopy and LSCI. *In vivo* two-photon imaging demonstrates impaired vasodilation in response to hypercapnic challenge at the level of penetrating arteries in the absence of microglia. n=22 and n=18 vessels from 8 control and 6 depleted mice, **p=0.0013, unpaired t-test. **b)** Representative difference images show that in the absence of microglia hypercapnia-induced CBF response is significantly decreased compared to controls (arrowheads show ROIs). Scale bar: 1 mm. **c)** The average kinetics of hypercapnia-evoked CBF increases show difference in depleted-mice compared to control mice. n=14-12 ROIs from 7 control and 6 depleted mice, 2 ROIs/mouse (c,d), ****p<0.0001, Mann-Whitney test (c), *p=0.0472, unpaired t-test (d). **d)** CBF response to hypercapnic challenge

is significantly reduced in the absence of microglia under ketamine-medetomidine or **e)** ketamine-medetomidine anesthesia after intraperitoneal injection of atipamezole. n=12-10 ROIs from 6 control and 5 depleted mice, 2 ROIs/mouse, *p=0.0436, unpaired t-test (e). **f)** Arterial pCO_2, pO_2 and pH measurements under ketamine-medetomidine anesthesia after the administration of atipamezole performed before and after hypercapnia. Blood samples were taken from the femoral artery. No significant difference was found between control and microglia-depleted mice. n=10 control and n=8 depleted mice, two-way ANOVA followed by Sidak's multiple comparison test (209).

4.5.3. CBF response to hypercapnia is significantly decreased in P2Y12R KO mice

Next we examined whether microglial P2Y12R is implicated in hypercapnia-induced vasodilation. Interestingly, we observed markedly decreased CBF response to hypercapnia in P2Y12R KO mice compared to controls measured by LSCI (Figure 23. a), similarly to that seen in the absence of microglia (Figure 22. b-e). Besides, we found impaired hypercapnia-induced vasodilation in the absence of microglial P2Y12R (using $CX3CR1^{GFP/+}$ x P2Y12R KO mice) compared to control ($CX3CR1^{GFP/+}$) ones measured by *in vivo* two-photon microscopy (Figure 23. b). In addition, formation of perivascular phylopodia was also significantly reduced after hypercapnia in P2Y12R KO mice compared to that seen in controls (Figure 23. c), supporting the important role of microglial process interactions with the cerebral vasculature. Next, we studied neuronal activity during hypercapnia. We did not find significant differences between control, microglia-depleted and P2Y12R KO mice (Figure 23. d).

DOI:10.14753/SE.2023.2742

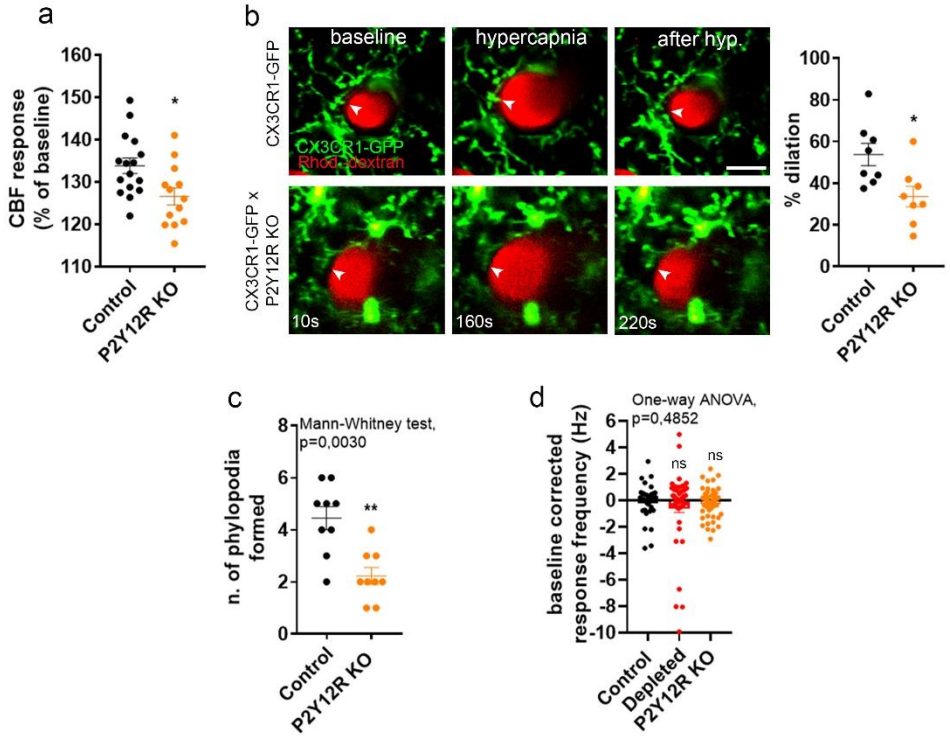

Figure 23. Hypercapnia-induced vasodilation is significantly decreased in P2Y12R KO mice. a) Hypercapnia-induced CBF response is significantly reduced in P2Y12R KO mice measured by LSCI. n=16 control, n=13 P2Y12R KO, *p=0.0131, unpaired t-test. **b)** *In vivo* two-photon imaging shows that elimination of P2Y12R impairs hypercapnia-induced vasodilation in double transgenic ($CX3CR1^{GFP/+}$ x P2Y12R KO) mice compared to P2Y12R-competent $CX3CR1^{GFP/+}$ mice. n=8-8 vessels from n=5 control and n=5 P2Y12R KO mice, *p=0.0104, Mann-Whitney test. Scale bar: 20 µm. **c)** The number of phylopodia formed at the end of perivascular microglial processes after hypercapnic challenge is markedly decreased in P2Y12R KO mice. n= 5 control and n=5 P2Y12R KO mice, **p=0.003, Mann-Whitney test. **d)** During hypercapnia neuronal activity did not differ markedly between control, microglia-depleted and P2Y12R KO mice. n=49 single units in control, n=44 in depleted and n=61 in P2Y12R KO group, p=0.4852, Kruskal-Wallis test with Dunn's multiple comparison (209).

Based on our previous findings, we studied the possible links between microglial P2Y12R and NO in hypercapnia-induced vasodilation. NO functions, including vasodilation are

mediated by cyclic GMP (cGMP), which is activated by NO (251). To achieve precise timing of hypercapnia, we prepared neocortical acute slices from mice and induced hypercapnia by bubbling 14.6% CO_2 under normoxic conditions for 15 min prior to measuring cGMP immunoreactivity on rapidly fixed brain slices. Importantly, we found that hypercapnia induced a robust increase of cGMP levels in CD13-positive cells, which marker is known to homogenously label VSMCs, ensheathing and thin-strand/mesh pericytes along the cerebrovascular tree (252) (Figure 24. a). Interestingly, hypercapnia-induced cGMP increases were markedly inhibited by the blockade of microglial P2Y12R with PSB0739 (Figure 24. a). To confirm that the NO-sGC-cGMP pathway caused the robust elevation of cGMP levels in response to hypercapnia, we applied SNP, a widely-used NO donor. The administration of SNP led to marked increases in identical anatomical structures, but it was not affected by P2Y12R blockade (Figure 24. b). Besides, we showed that hypercapnic challenge increased cGMP levels in CD13-positive profiles *in vivo* (Figure 24. c).

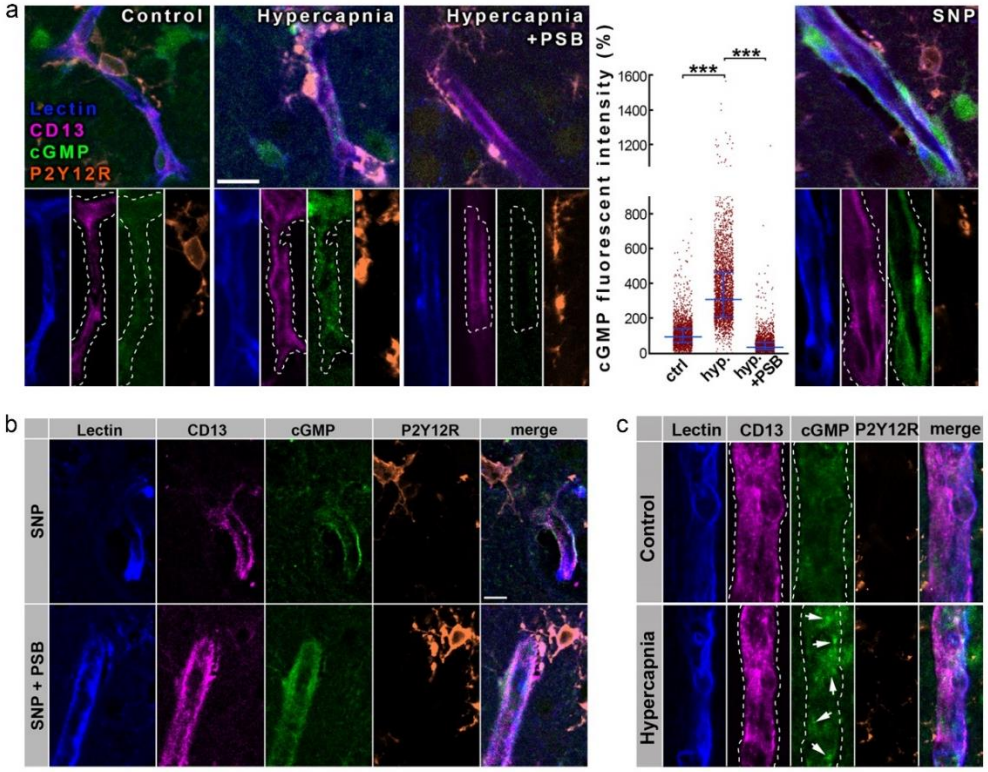

Figure 24. Selective blockade of microglial P2Y12R leads to decreased cGMP levels in response to hypercapnia *ex vivo*. a) Single image planes for CLSM imaging demonstrate small blood vessel segments from the 2-3rd layer of the neocortex in acute brain slices. Lectin

(blue) outlines the vessels, CD13 labels contractile NVU cells (pericytes and smooth muscle cells), microglial P2Y12R is orange, while cGMP signal is shown in green. cGMP levels were measured within areas (marked by white dashed line) masked based on CD13 staining. A low level of basal cGMP levels can be observed under control conditions, while hypercapnia induced a robust increase in vascular cGMP levels. Preincubation of the acute slices with the specific P2Y12R inhibitor PSB0739 abolished hypercapnia-evoked cGMP increase. As a control, the NO-donor SNP was applied which induced robust cGMP elevation. Scale bar is uniformly 15 μm. n=3 mice, ****p<0.0001, Kruskal-Wallis test. Data are expressed as median ± IQR. **b)** CLSM images show that PSB0739 treatment has no effect on SNP-induced cGMP. **c)** CLSM imaging shows small blood vessel segments from the 2-3rd layer of the neocortex in perfusion-fixed brain slices. Hypercapnic challenge was performed *in vivo* and maintained in anesthetized mice until sacrifice. Lectin (blue) outlines the vessels, CD13 labels contractile NVU cells (pericytes and smooth muscle cells), microglial P2Y12R is orange, while cGMP signal is green shown by white arrows (209).

4.6. Hypercapnia and hypoxia induce rapid stimulus-dependent release of different purinergic metabolites by NVU cells and microglia in the brain

4.6.1. Microglia modulate brain pH and produce adenosine in response to hypercapnia in vivo

To further study the mechanisms through which microglia modulate CBF, cortical blood perfusion was measured by laser Doppler and tissue pH was simultaneously assessed by pH-selective electrode during hypercapnia, as it's well-known that hypercapnia drives vasodilation in the brain mainly through reducing brain pH (57). Interestingly, we found significantly lower baseline brain pH in the absence of microglia, but the relative amplitude of the hypercapnia-induced negative pH shift was not different in control vs microglia-depleted mice (Figure 25. a-b), suggesting that microglia contribute to modulation of brain pH. Laser-Doppler flowmetry confirmed that hypercapnia-induced CBF increase is significantly smaller in the absence of microglia (Figure 25.c), as evidenced previously by *in vivo* LSCI and two-photon imaging. Next, we investigated whether hypercapnia-induced

DOI:10.14753/SE.2023.2742

negative pH shift leads to the production of specific purinergic metabolits (e.g. ATP, ADP, adenosine) in astrocytes and endothelial cells, which may drive microglial process recruitment, as suggested by clustering of microglial P2Y12R at endothelial contact sites near mitochondria (Figure 9. i-k) and by MicroDREADD^{Dq} experiments (Figure 18. c-e). Our *in vitro* experiments revealed that hypercapnic challenge decreased both extracellular and intracellular pH (Figure 25. d-e). Besides, hypercapnic challenge triggered rapid ATP and ADP release from cultured endothelial cells, whereas astrocytes produced mainly ATP and adenosine, while cultured microglia released ADP and adenosine in response to hypercapnia measured from culture medium by HPLC (Figure 25. f). Next we investigated hypercapnia-induced changes of adenosine levels *in vivo* after microglia depletion in the brain. We found that hypercapnia-induced adenosine levels were attenuated in the absence of microglia measured from brain tissue homogenates by HPLC (Figure 25. g). These results suggest that hypercapnia leads to rapid production of different purinergic metabolits and microglia release high levels of adenosine in response to hypercapnia, which is a potent vasodilator (64, 70).

DOI:10.14753/SE.2023.2742

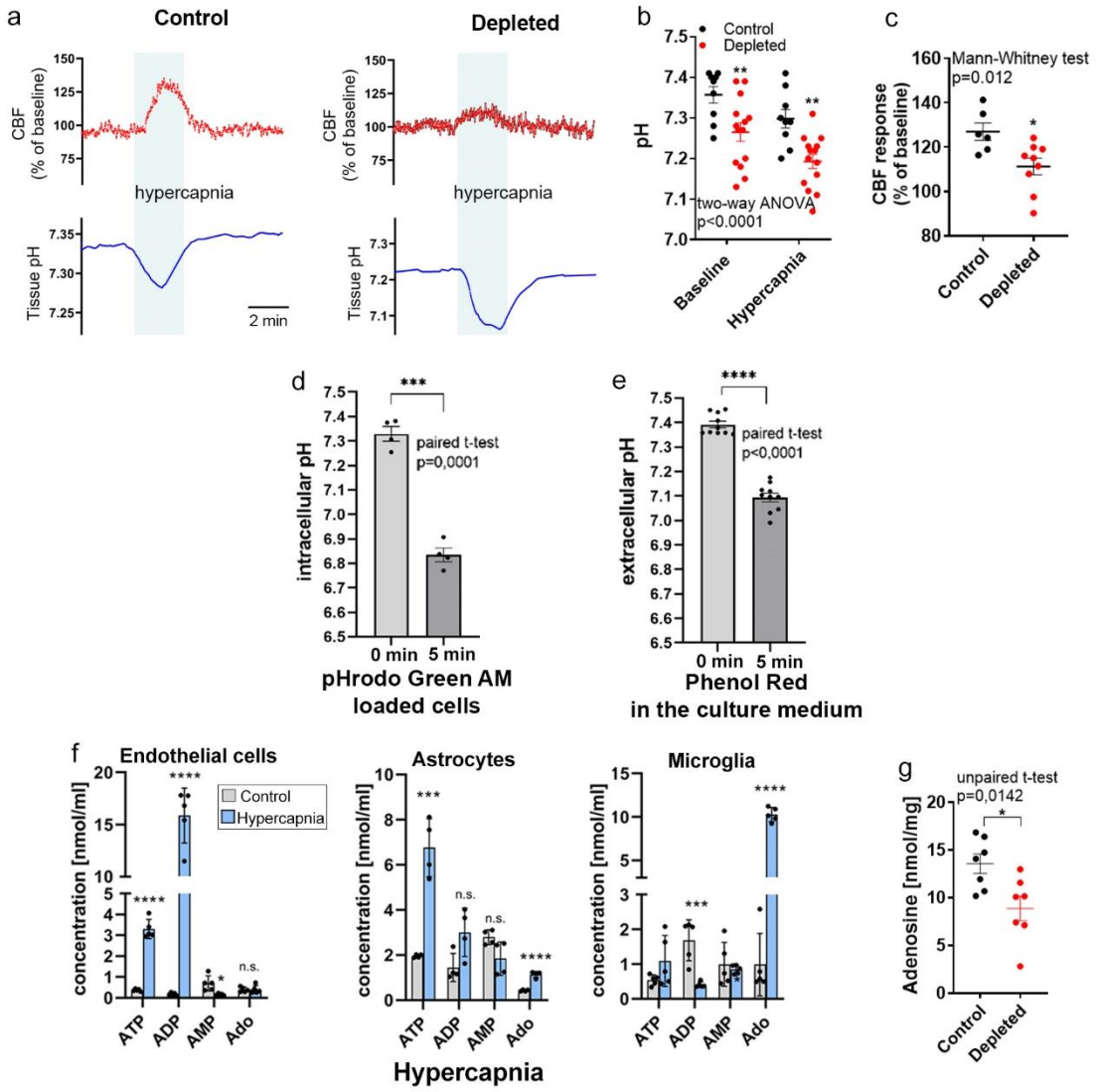

Figure 25. Microglia modulate brain pH and release adenosine in response to hypercapnia *in vivo.* a) CBF by laser Doppler flowmetry and tissue pH by pH-selective electrode were simultaneously measured during 2 minutes long hypercapnic challenge. Representative curves of CBF and pH changes in control and microglia-depleted mice are shown. **b)** Microglia-depleted mice show decreased extracellular brain pH. n=10 and n=16 measurements from 6 control and 9 depleted mice, ****p<0.0001, two-way ANOVA followed by Sidak's multiple comparison (**p=0.0093 control vs depleted baseline, **p=0.0028 control vs depleted hypercapnia). **c)** Hypercapnia-induced CBF response is significantly decreased in microglia-depleted mice similarly as it was seen during LSCI

measurements. n=6 control and 9 depleted mice, *p=0.012, Mann-Whitney test. **d-e)** Both intracellular (d) and extracellular (e) pH markedly decreases within a few minutes after exposing cells to 15% CO2/85% air gas mixture, as a model of hypercapnia. Extracellular pH was determined by Phenol Red absorbance measurements while intracellular pH was measured as changes in pHrodo Green AM dye fluorescence in glial cells. n=4 parallels per group, ***p=0,0001 0 min vs 5 min, paired t-test, (d); n=10 parallels per group, ****p<0,0001 0 min vs 5 min, paired t-test, (e). **f)** Hypercapnic challenge influences production of purinergic metabolites (ATP, ADP, AMP and Ado – adenosine) in primary endothelial- astrocyte- and microglia cultures as measured in cell culture medium by HPLC. Endothelial cells: ATP ****p<0.0001, ADP ****p<0.0001, AMP *p=0.01226 control vs hypercapnia; astrocytes: ATP ***p=0.00029, Ado ****p=0.000057 control vs hypercapnia; microglia: ADP ***p=0.00134, Ado ****p<0.0001 control vs hypercapnia, multiple t-test. **g)** In microglia-depleted mice adenosine levels are significantly decreased in the cerebral cortex in response to hypercapnic challenge compared to controls. Adenosine was measured in cortical brain tissue homogenates by HPLC. n=7 control and n=7 depleted mice, *p=0.0142, unpaired t-test (209).

4.6.2. Hypoxia induce rapid release of purinergic metabolites from NVU cells and microglia in vitro

Next, we studied the effect of hypoxia on the production of purinergic metabolites *in vitro*. Hypoxia was validated by using hypoxia green AM loaded cell cultures (Figure 26. a). We found that hypoxic challenge leads to production of ATP and AMP by cultured endothelial cell, while astrocytes and microglia released mainly ADP assessed by HPLC (Figure 26. b). These data suggest that hypoxia also lead to rapid production of different purinergic metabolites in endothelial cells, astrocytes and microglia.

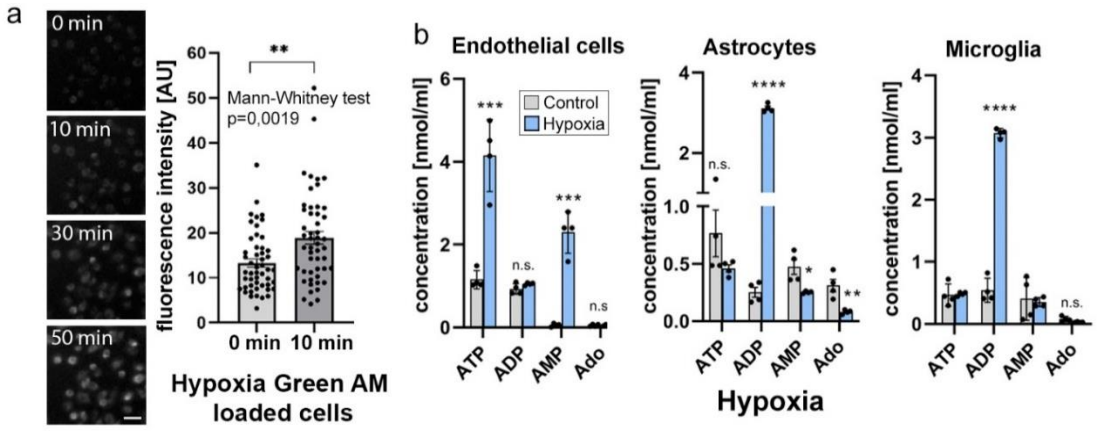

Figure 26. Hypoxia induce rapid release of different purinergic metabolites from NVU cells and microglia *in vitro.* a) Hypoxia Green AM loaded cells exhibit significant increase in fluorescent intensity within 10 minutes after placing microglia cultures to hypoxic environment (1% O2/5% CO2/94% N2). The reagent begins to fluoresce when oxygen level drops below 5%. n=50 parallels per group, **p=0.0019 0 min vs 10 min, Mann-Whitney test. Scale bar: 30 μm (a). Data are shown as mean ± SEM. **b)** Hypoxic challenge induces significant changes in levels of purinergic metabolites (ATP, ADP, AMP, Ado) in primary endothelial- astrocyte- and microglia cultures as measured in culture medium by HPLC. Endothelial cells: ATP ***p=0.00054, AMP ***p=0.00011 control vs hypercapnia; astrocytes: ADP ****p<0.0001, AMP *p=0.0148, Ado **p=0.0059 control vs hypercapnia; microglia: ADP ****p<0.0001 control vs hypercapnia, multiple t-test. Data are expressed as mean ± SEM (209).

4.7. Microglia sense and modulate cerebral blood flow changes during hypoperfusion induced by repeated common carotid artery occlusion (CCAo)

4.7.1. Microglia respond rapidly to reduced cerebral blood flow after repeated CCAo as indicated by increased microglial process motility and altered process morphology in vivo

Stimulus-specific release of purinergic mediators by different NVU cells suggested that microglial effects on CBF are likely to be important for the maintenance of sufficient cerebral blood perfusion, which is compromised in diverse vascular diseases including stroke, chronic

DOI:10.14753/SE.2023.2742

hypoperfusion or vascular dementia among others (5, 89, 253). To investigate the actions of hypoperfusion-primed microglia (254) on subsequent CBF changes, we developed a model by performing repeated transient unilateral common carotid artery occlusion (CCAo) and reperfusion 3 times (Figure 27. a-b). Redistribution of blood flow to the ipsilateral cortical circulation requires vasodilation (44), and unilateral CCAo does not induce cerebral ischemia (44, 255), which makes this model suitable for investigation of vascular adaptation responses during hypoperfusion in the absence of neuronal injury, which is influenced by microglia manipulation (176). Interestingly, *in vivo* two-photon imaging showed that microglial processes rapidly respond to CBF reduction, as shown by increased process motility of blood vessel-associated microglia immediately after CCAo (Figure 27. c). Besides, we observed that changes in microglial process morphology are maintained up to 24h after CCAo measured by high-resolution automated morphological analysis on perfusion-fixed brain tissues (Figure 27. d).

DOI:10.14753/SE.2023.2742

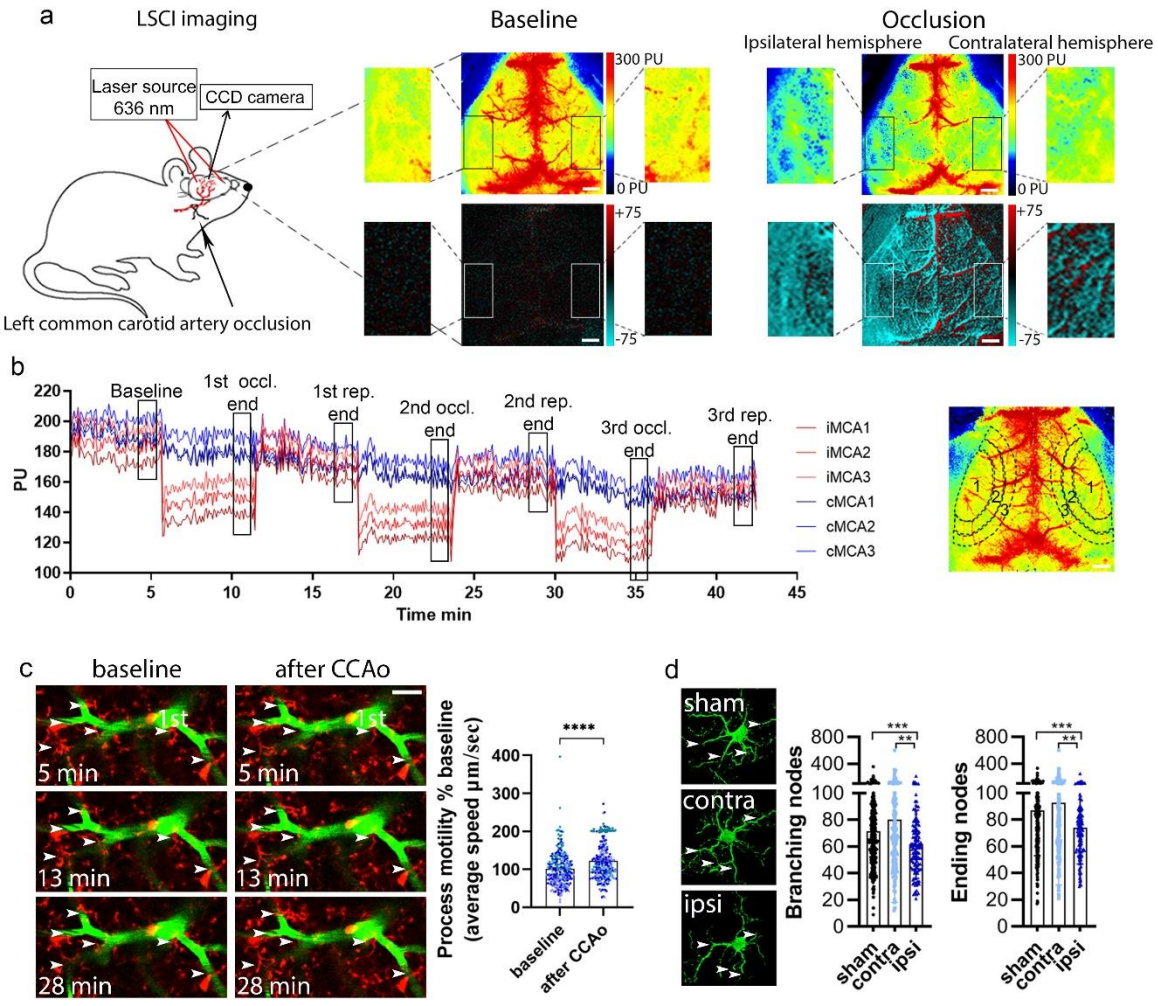

Figure 27. Microglia respond rapidly to decreased CBF after repeated CCAo as indicated by increased microglial process motility and altered process morphology *in vivo*. a) CBF was measured during transient left CCA occlusion through the intact skull bone. Representative perfusion (0 - 300 PU, on the top of panel a) and difference images (-75 - +75, on the bottom of panel) of baseline CBF and CBF changes during CCA occlusion. Scale bar: 1 mm. **b)** Representative curves demonstrate the typical kinetic of repeated (3x CCA) occlusions on the areas (MCA1-3 areas) which were investigated on both hemispheres. ROIs are outlined by white dashed lines on a representative perfusion image on the right. Black rectangles on the kinetic graph label the parts of perfusion curves, which were used for detailed analysis. Scale bar: 1 mm. **c)** Increased microglial process motility was observed to repeated (3x) CCAo in CX3CR1^{tdTomato} mice imaged by *in vivo* two-photon microscopy.

Arrowheads show contacting microglial processes. 1st denotes first-order capillary. n=6 mice, ****p<0.0001, Mann-Whitney test. Scale bar: 20 μm. **d)** Automated morphological analysis reveals decreased number of branching-, and ending nodes of microglial processes ipsilaterally in CX3CR1 $^{GFP/+}$ mice 24h after 3x CCAo compared to the contralateral side (contra) and sham mice in the cerebral cortex. Branching-ending nodes of n=386-388 sham, n=197 contralateral n=134 ipsilateral cells from n=3 sham and n=3 CCAo mice, Kruskal-Wallis test followed by Dunn's multiple comparisons test (branching nodes: ***p=0.0008 sham vs ipsi, **p=0.005 contra vs ipsi; ending nodes: ***p=0.0007 sham vs ipsi, **p=0.0083 contra vs ipsi) (209).

4.7.2. Selective elimination of microglia results in impaired adaptation to reduced cortical perfusion after repeated CCAo

Next, we investigated the effect of microglia depletion on adaptation to cortical hypoperfusion *in vivo* using LSCI (Figure 28. a). Importantly, we found significantly impaired adaptation to decreased cortical perfusion after CCAo in microglia-depleted mice compared to control ones (Figure 28. a-b). This was evidenced by lower baseline-corrected CBF values after 5min CCAo and subsequent reperfusion for 5min, which effect gradually increased as CCAo and reperfusion were repeated two more times (Figure 28. a-b and Figure 27. a-b). Interestingly, the absence of microglia also significantly impaired CBF recovery after repeated CCAo in the contralateral hemisphere (Figure 28. b), suggesting that microglial actions are involved in normalizing CBF responses during reperfusion. Impaired CBF recovery was also evident in both hemispheres between the 2nd and the 3rd reperfusions in microglia-depleted mice (Figure 28. b**)**.

DOI:10.14753/SE.2023.2742

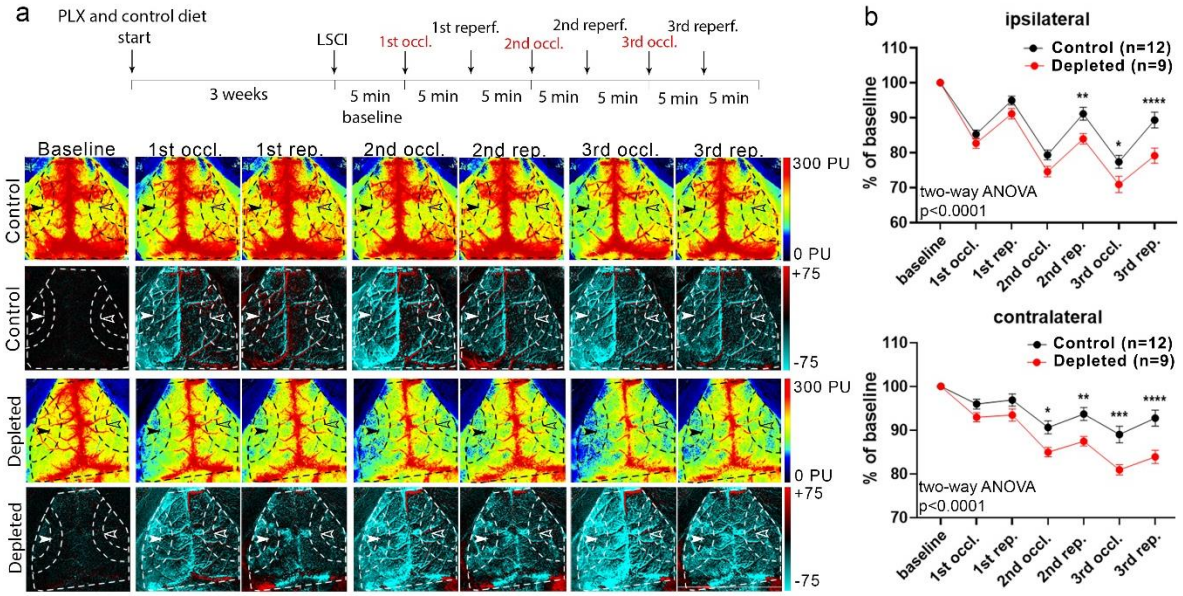

Figure 28. Adaptation to cortical hypoperfusion is impaired in the absence of microglia. **a)** Schematic of the experimental CCAo protocol. Representative perfusion (1st and 3rd rows), and difference LSCI images (2nd and 4th rows) demonstrate cortical perfusion changes in response to 3x unilateral CCAo in control and microglia-depleted mice. Dashed lines show the area of quantification in both the ipsilateral (white arrowheads) and contralateral (empty arrowheads) hemisphere. Venous sinuses were excluded from the analysis. Scale bar: 1 mm. **b)** CBF changes to 3x CCAo are expressed as the percentage of baseline. In the absence of microglia a significant CBF reduction is observed in both ipsilateral and contralateral hemispheres. n=9 control and n=12 depleted mice, ****p<0.0001, two-way ANOVA followed by Sidak's multiple comparison test (ipsilateral 2nd rep.: **p=0.0099, 3rd occl.: *p=0.0270, 3rd rep.: ****p<0.0001 control vs depleted; contralateral 2nd occl.: *p=0.0233, 2nd rep.: **p=0.0052, 3rd occl.: ***p=0.0001, 3rd rep.: ****p<0.0001 control vs depleted) (209).

Next, we investigated whether perivascular macrophages (PVMs) are involved in modulation of CBF during repeated CCAo. To this end, we selectively eliminated PVMs from the brain using ICV clodronate injection without affecting resident microglia (Figure 29. a-c). Clodronate is phagocytosed by PVMs, leading to their death by apoptosis. We did not find

DOI:10.14753/SE.2023.2742

significant difference in CBF changes after CCAo between control and PVM-depleted mice measured by LSCI (Figure 29. d), suggesting that microglia sense and influence CBF changes differently in this model of hypoperfusion than other brain macrophages.

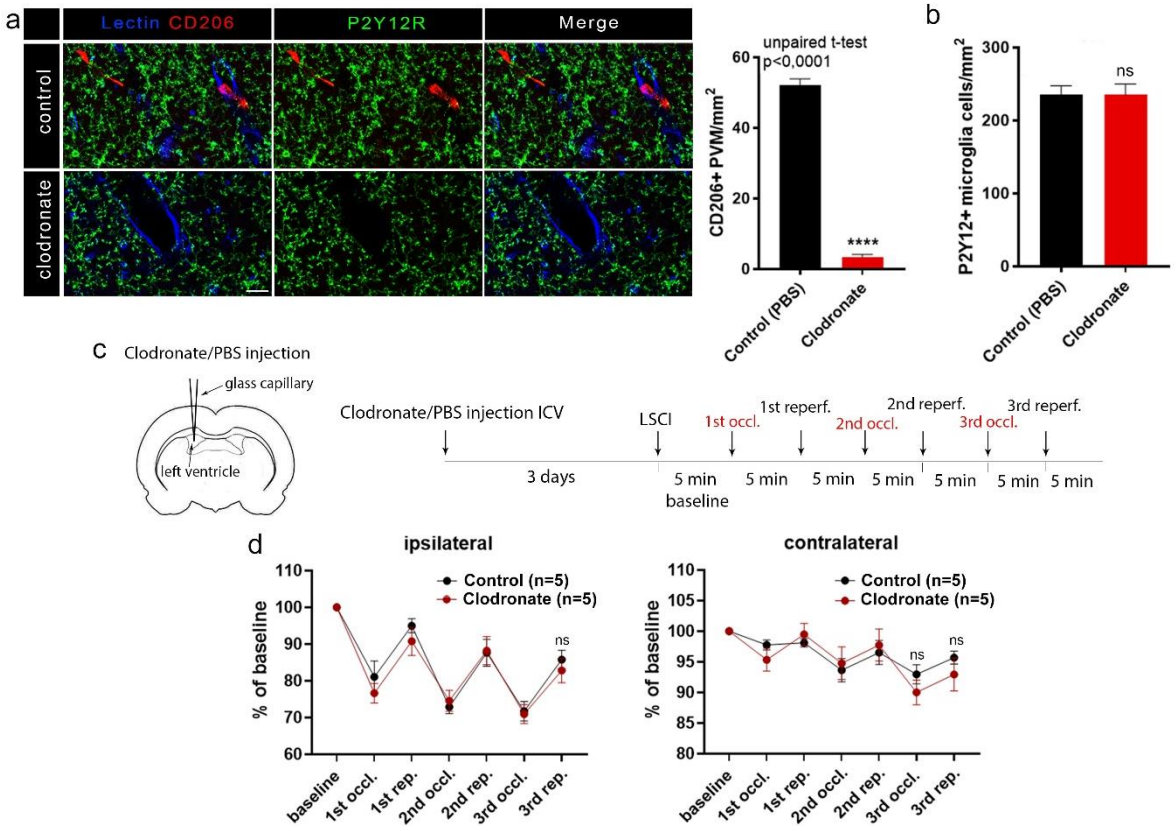

Figure 29. Perivascular macrophages are not involved in the modulation of cortical blood perfusion during repeated CCAo. a) Intracerebroventricular (ICV) clodronate injection lead to the elimination of CD206-positive perivascular macrophages (PVMs), but did not influence microglial cells (P2Y12R labeling, green). The endothelial marker, Tomato lectin (blue) was used to label blood vessels. Scale bar: 20 μm. Quantification of the number of PVMs after ICV clodronate liposomes or PBS injection. n=5-5 mice control vs. clodronate-injected, ****p<0.0001, unpaired t-test with Welch's correction. **b**) Graph shows quantification of the number of P2Y12R-positive microglia cells after ICV clodronate liposomes or PBS injection. n=5-5 mice control vs. clodronate injected, unpaired t-test with Welch's correction. **c)** Outline of the experimental protocol. PVMs were eliminated from the brain by ICV liposomal clodronate injection before LSCI measurements. **d)** CBF changes in

response to 3x CCAo in the absence of PVMs did not differ from that seen in control mice. n=5-5 mice control vs. clodronate injected, two-way ANOVA followed by Sidak's multiple comparison test. Data are expressed as mean ± SEM (209).

4.7.3. Microglial P2Y12R signaling is essential for normalizing CBF during adaptation to hypoperfusion after repeated CCAo

Our HPLC experiments revealed that NVU cells rapidly produce both ADP and ATP in response to hypercapnia and hypoxia. ATP is rapidly broken down by ectoATPases to ADP, which is the main ligand for microglial P2Y12R expressed by microglial processes (239) among other cells. Thus, we examined whether the genetic deletion or acute pharmacological blockade of microglial P2Y12R using PSB0739 injected into the cisterna magna (239) leads to altered CBF responses after repeated CCAo (Figure 30. a-c). Interestingly, we found that blood flow recovery was significantly impaired after both genetic and pharmacological P2Y12R blockade in both ipsilateral and contralateral hemispheres (Figure 30. b-c), similarly to that seen in microglia-depleted mice (Figure 28.). These results strongly indicate the important role of microglia and microglial P2Y12R in normalizing CBF in responses during adaptation to reduced cortical perfusion after CCAo.

DOI:10.14753/SE.2023.2742

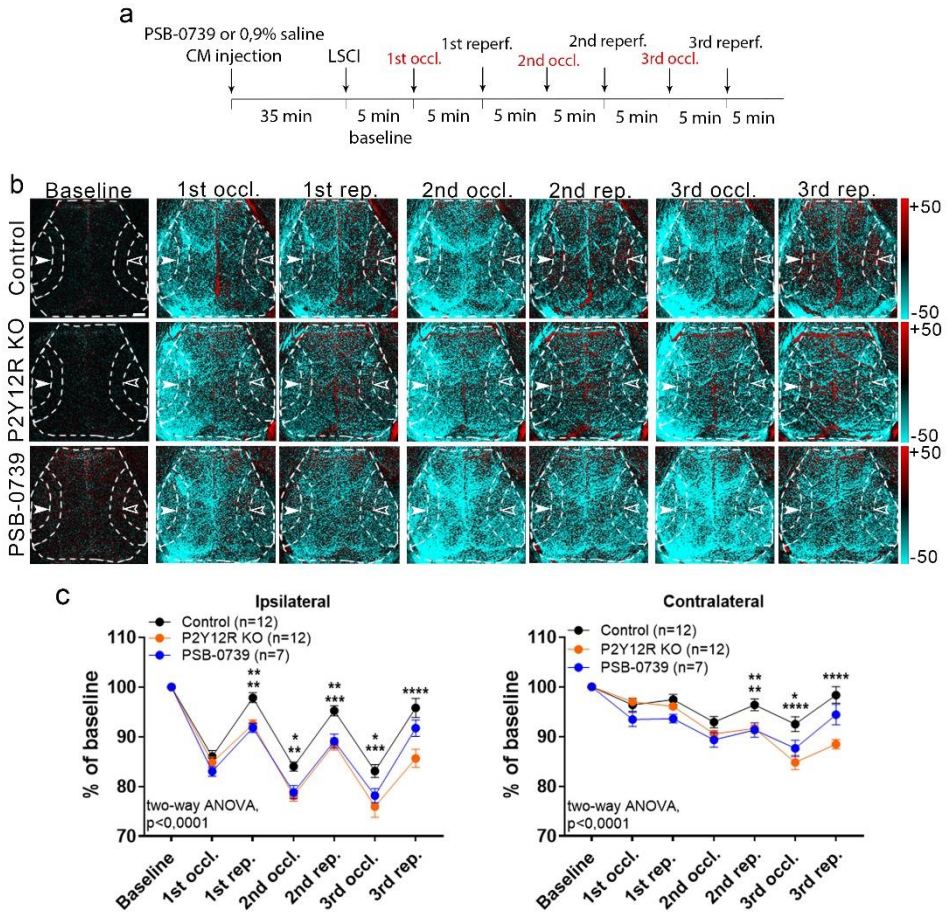

Figure 30. Microglial P2Y12R signaling is essential for normalizing CBF during adaptation to cortical hypoperfusion. a) Schematic of the 3x CCAo protocol. **b)** Representative difference images demonstrate impaired cortical perfusion in response to 3x CCAo in P2Y12R KO and PSB0739-injected mice compared to controls in both hemispheres. Dashed lines show the MCA2 area both in the ipsilateral (white arrowheads), and in the contralateral hemisphere (empty arrowheads) corresponding to the quantitative analysis shown in panel c. Scale bar: 1 mm. **c)** CBF changes during adaptation to repeated hypoperfusion are significantly impaired as seen both in the ipsilateral and contralateral hemispheres of P2Y12R KO mice and PSB0739-injected mice compared to control mice. n=12 control, n=12 P2Y12R KO, n=7 PSB0739-injected mice, ****p<0.0001, two-way ANOVA followed by Tukey's multiple comparison test (ipsilateral 1st rep.: **p=0.0042 control vs P2Y12R KO, **p=0.0057 control vs PSB-0739, 2nd occl.: **p=0.0013 control vs P2Y12R KO,*p=0.0214 control vs PSB-0739, 2nd rep.: ***p=0.0002 control vs P2Y12R

KO, **p=0.0049 control vs PSB-0739, 3rd occl: ***p=0.0001 control vs P2Y12R KO, *p=0.0302 control vs PSB-0739, 3rd rep.: ****p<0.0001 control vs P2Y12R KO; contralateral 2nd rep.: **p=0.004 control vs P2Y12R KO, **p=0.0096 control vs PSB-0739, 3rd occl.: ****p<0.0001 control vs P2Y12R KO, *p=0.0133 control vs PSB-0739. 3rd rep.: ****p<0.0001 control vs P2Y12R KO). Data are expressed as mean ± SEM (209).

4.8. Deletion of brain endothelial IL-1R1 improves early cortical perfusion deficits after cerebral ischemia

We have also studied the inflammatory mechanisms through which microglia may interfere with vascular responses. The pro-inflammatory cytokine IL-1 with its two isoforms, IL-1β and IL-1α, is a key contributor to neuroinflammation and ischemic brain injury. Both IL-1β and IL-1α are rapidly produced in response to cerebral ischemia in the brain and microglia are considered as an important source of these cytokines. IL-1 isoforms act on IL-1R1 (interleukin-1 type 1 receptor), which is expressed on neurons, endothelial cells (193, 256) and astrocytes among other cell types. Increasing evidence shows that blockade of IL-1-signaling using IL-1 receptor antagonist (IL-1Ra) is protective in different models of stroke and acute brain injury (257-259). However, the cellular mechanisms through which IL-1 acts are unclear. Thus, we investigated whether IL-1 signaling mediates cerebral perfusion changes following cerebral ischemia through endothelial IL-1R1. To this end, the middle cerebral artery occlusion (MCAO) model was applied to induce focal cerebral ischemia in mice and CBF changes were measured 30 min after the induction of reperfusion in three adjacent regions of the MCA area using LSCI (Figure 31. a). We found that deletion of endothelial IL-1R1 leads to a significantly smaller perfusion deficit in the ipsilateral hemisphere at the MCA2 and MCA3 areas compared to controls (Figure 31. b-c). Thus, these results collectively implicate microglia as key modulators of cerebral blood flow in health and disease, in which purinergic mechanisms and signaling by inflammatory cytokines are also involved.

DOI:10.14753/SE.2023.2742

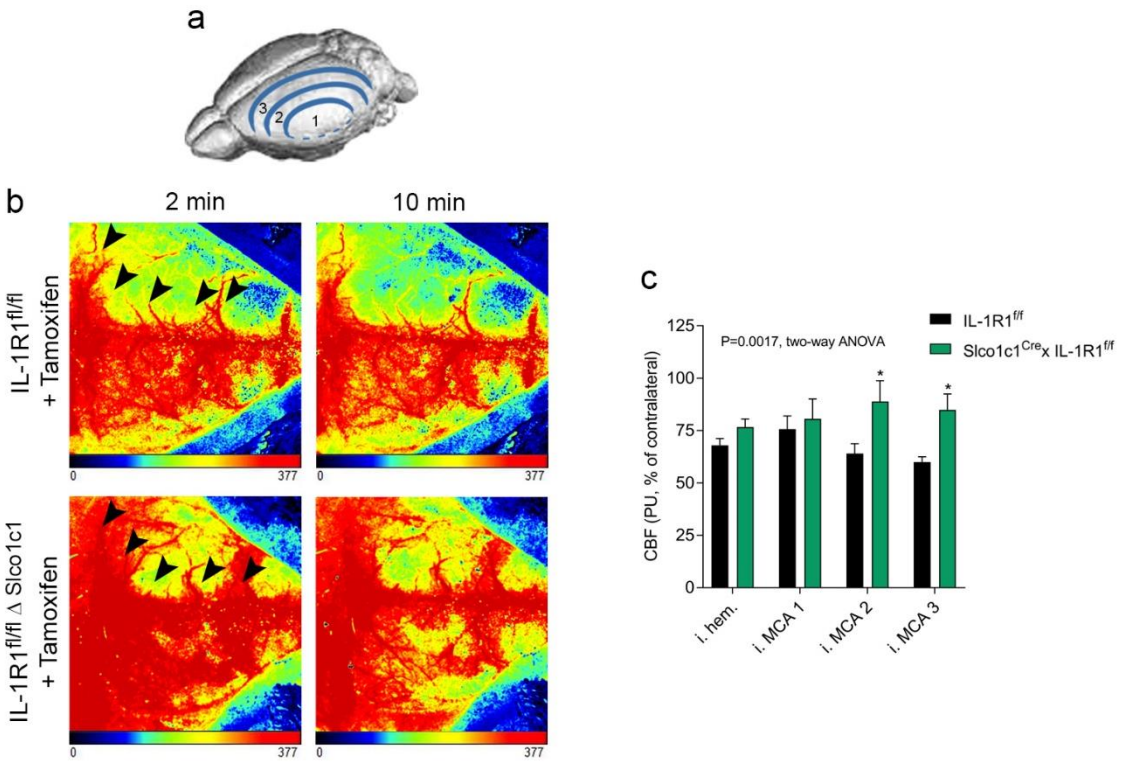

Figure 31. In the absence of endothelial IL-1R1 early perfusion deficits are reduced following cerebral ischemia. a) Cortical perfusion was measured by LSCI in three adjacent regions (MCA1-MCA3) centred around the primary MCA area. **b)** Representative LSCI images demonstrate that 30 min after the induction of reperfusion IL-1R1$^{fl/fl\ \Delta\ Slco1c1}$ mice show better blood flow recovery compared to IL-1R1$^{fl/fl}$ mice, which is most visible in areas MCA2 and 3 (arrowheads) during the 10 min measurement period. Note that cortical perfusion remains relatively uniform between the 2 min and 10 min representative time points. **c)** Quantitative analysis shows markedly higher cerebral perfusion in the ipsilateral hemisphere. n=5-5 mice, $p \leq 0.01$, two-way ANOVA (all ROIs included) with Tukey's post hoc multiple comparisons showing differences in the MCA2 and MCA3 zones ($p \leq 0.05$, $n = 5$). Data are expressed as means ± SEM (211).

DOI:10.14753/SE.2023.2742

5. Discussion

My studies have identified microglia as a novel cell type modulating cerebral blood flow, which involves complex purinergic mechanisms. Using three different experimental models, we demonstrate that the presence of functional microglia is essential to maintain optimal CBF responses to physiological neuronal activity (neurovascular coupling), hypercapnia and during cerebrovascular adaptation to reduced cortical perfusion after CCAo. These actions are dependent on microglial P2Y12R signaling, clearly discriminating microglial responses from those mediated by PVMs or other brain macrophages (108). Furthermore, we have identified the cerebrovascular endothelium as a major target for IL-1 actions after ischaemic stroke. Brain endothelial IL-1 actions have a robust and early impact on cortical perfusion after acute brain injury. Thus, microglia-dependent effects and IL-1 actions on the cerebrovascular endothelium emerge as key events that may shape cerebral perfusion and contribute to the inflammatory conditions which may influence outcome in diverse cerebrovascular pathologies, such as cortical hypoperfusion or stroke.

It has been long recognized that microglia physically interact with the cerebral vasculature. Previous findings have shown that dynamic microglial processes come into close proximity with blood vessels both in the intact and the injured brain, however the precise function of these interactions has remained vaguely defined (105, 175). Most research has focused on understanding these interactions in the developing brain and in the context of different brain diseases such as stroke, Alzheimer's disease and Multiple Sclerosis. During development, microglia are involved in angiogenesis, and it has been noticed that microglial processes closely associate with developing blood vessels and take part in the formation of vascular branching (105). Microglia are known to play an important role in regulation of vascular inflammation and BBB function, actively communicate with the endothelium, affect BBB permeability and leukocyte infiltration. Besides, microglia produce various inflammatory mediators, including IL-1β, TNF-α, NO, PGE2 or ROS, some of which are known as vasoactive mediators (5, 105). There is growing evidence for interactions between microglia and the cells of NVU including astrocytes, pericytes, endothelial cells and neurons, which cells are critical regulators of CBF. However, previous research focused on the significance

of these interactions during development and neuroinflammation (105, 185) and the potential contribution of microglia to CBF has been largely neglected to date.

First, we asked whether a direct contact between microglia and endothelial cells exists in the healthy adult neocortex, as microglial cell bodies are located in the brain parenchyma and the endothelial basal lamina is surrounded by a second, glial basement membrane (260). We found that microglia dynamically contact all segments of the cerebrovascular tree *in vivo* and form direct, purinergic contacts with endothelial cells, peri-arterial smooth muscle cells, pericytes and astrocytes in both mouse and the human brain. Interestingly, our electron tomography studies revealed an accumulation of P2Y12R on microglial processes contacting endothelial cells in the vicinity of endothelial mitochondria, where ATP release may recruit microglial processes to the vasculature in response to CBF changes (242). Similar interactions are seen at neuronal somata, where microglia form somatic junctions in the vicinity of mitochondria due to excessive ATP release (239), through which microglia sense neuronal mitochondrial activity and modulate neuronal responses via purinergic signaling. It has long been known that purinergic signaling plays an important role in regulating microglial activity, accumulating studies show the role of microglial purinergic receptors in brain inflammatory processes (261). Microglial processes are recruited to sites of ATP release via P2Y12Rs, which primarily sense ADP produced by ATP hydrolysis or cleavage by NTPDase1 expressed on the microglial membrane among other cells (129, 239, 241). Each hydrolysis product of ATP (i.e., ADP, AMP, and adenosine) possesses strong vasodilating properties. In addition, the importance of ATP signaling in the vasculature has been demonstrated under both homeostatic and pathological conditions (242). Our anatomical observations thus suggested that purinergic mediators, such as ATP or ADP may be released from NVU cells to recruit P2Y12R-positive microglial processes during vascular adaptation responses or perfusion changes, even under physiological conditions.

Previous studies revealed that purinergic signaling plays a central role in neurovascular coupling response in the brain (84). Neurovascular coupling is a dynamic functional change in CBF in response to local neuronal activity, which involves different cell types within the NVU, including astrocytes, vascular smooth muscle cells, pericytes and endothelial cells (5, 89). However, a role for microglia has not been previously established. Thus, to investigate

whether microglia could influence CBF responses to physiological neuronal activity, we turned to the widely used whisker stimulation model. During functional hyperaemia, dilation of arterioles propagates at high speed in a retrograde direction to upstream arteries, including branches of pial arteries, with both arteriolar and capillary dilation playing a role in increased O2 delivery (89). Our LSCI and fUS studies revealed significantly smaller CBF response to whisker stimulation in the barrel cortex in the absence of microglia, or microglial P2Y12R, which was not explained by altered neuronal responses in the barrel cortex as assessed by in vivo electrophysiology or two-photon calcium imaging. While neuronal activity during hypercapnia was not different between control, P2Y12R KO and microglia-depleted mice either, it remains to be investigated whether microglia-dependent effects may also influence CBF through changing baseline activity of neurons that control blood flow in the brain (89, 140, 239).

To test the specificity of the microglial actions observed, we developed a mouse model allowing selective chemogenetic targeting of microglia in real-time *in vivo*, which disrupts normal microglial process dynamics and renders depolarized cells less responsive to ambient ATP. Smaller CBF responses to whisker stimulation upon chemogenetically-induced microglial dysfunction suggest that sustained microglial sensing of purine metabolites and directed process recruitment are required to modulate functional hyperaemia in the cerebral microcirculation. These experiments also indicate that even temporary impairment in the dynamic communication between microglial processes and the vasculature could have marked impact on CBF and tentatively on other vascular responses, which has broad implications to any pathological conditions that are associated with altered microglial phenotypes.

We have also investigated the underlying mechanisms in microglia-mediated modulation of neurovascular coupling. A number of signaling pathways have been identified as participants in the process of neurovascular coupling (5). It is well established that astrocytes contribute to vasodilation during functional hyperaemia in the brain. In response to increased neuronal activity astrocytes produce various vasoactive molecules such as ATP, adenosine, NO, EETs and glutamate, all of which are able to modulate parenchymal arteriole vascular tone (37). Our high resolution anatomical studies revealed that P2Y12R-positive microglial processes

directly contact perivascular astrocytic endfeet and extend beyond endfeet to interact with endothelium. Thus, it is possible that microglial processes sense ATP or ADP released from astrocytic endfeet during functional hyperaemia and may influence the formation of vasodilating substances or directly release vasodilators at the interface between astrocytic endfeet and endothelium and contribute to modulation of CBF response. However, we can not exclude the possibility that there are other signaling pathways through which microglia may modulate CBF response to increased neuronal activity in the brain. To further investigate the possible mechanisms through which microglial P2Y12R may modulate vascular responses, we assessed the possible links with NO, a key mediator of vasodilation (5, 75, 251). The observation that the absence of microglia and NO blockade by L-NAME had an additive effect to reduce the coupling response upon somatosensory stimulation, strongly suggests that P2Y12R-positive microglia regulate the CBF response to somatosensory stimulation through signaling mechanisms that are, at least in part, additional to NO-mediated vasodilation. This may have broad physiological and pathological consequences given the complexity of CBF regulation in health and disease (5, 75, 89, 251).

We next tested whether microglia-mediated mechanisms influence vascular responses to hypercapnia. Hypercapnia induces vasodilation throughout the brain, which requires the development of extracellular acidosis and takes place via complex mechanisms that include endothelium-derived NO signaling, release of astrocytic prostaglandin E2, adenosine production and other processes, which eventually lead to relaxation of VSMCs and pericytes. (57, 66, 69, 247, 248). Importantly, while perivascular microglial processes rapidly responded to hypercapnia with calcium pulses and generation of new phylopodia, the absence of microglia markedly inhibited increases of CBF (as demonstrated independently by both LSCI and Laser Doppler Flowmetry) and vasodilation (as shown by *in vivo* two-photon imaging). This was independent of arterial blood pH, pO_2 and pCO_2 levels, which were not different in microglia-depleted mice. Surprisingly, we found that the absence of microglia reduced brain pH, while microglia rapidly produced adenosine in response to hypercapnia. Supporting this, recent findings showed that microglia represent a key source of adenosine in the brain, which modulates neuronal responses at synapses (140). Interestingly, our HPLC studies demonstrated that endothelial cells and astrocytes release different purinergic

metabolites in response to hypercapnia (ATP and ADP, and ATP and adenosine, respectively). While we found rapid alterations in microglia-endothelium and microglia-astrocyte interactions after hypercapnia, and hypercapnia-induced release of different purinergic metabolits (in particular, adenosine) in microglia cells. Although the mechanisms through which different purinergic mediators are released in the NVU remain to be explored, pannexin-1 (PANX1) channels are likely to be involved, which is also suggested by reduced hypercapnia-induced CBF responses in PANX1 KO mice (262). Hypercapnia drives vasodilation mainly via reduced extracellular pH, which is a major regulator of cerebrovascular reactivity and acts directly on cerebrovascular smooth muscle cells to cause relaxation, mediating the effects of increased CO2 levels (57). Microglial P2Y12 receptor-mediated Ca^{2+} signalling, migration and cytokine production are also pH-dependent (263, 264). Because adenosine is a potent vasodilator in the cerebral circulation (84), we suggest that lower brain pH in the absence of microglia may partially compensate for the loss of microglial vasoactive mediators with a net effect of reduced vasodilation during different vascular adaptation responses. It should be investigated in future studies whether microglial loss or dysfunction could induce compensatory actions in other NVU cells, such as promoting adenosine production by astrocytes (83).

Previous findings demonstrated that hypercapnia-evoked vasodilation is partly mediated by NO (58, 59). NO functions, including vasodilation are mediated by cyclic GMP (cGMP) synthesized through soluble guanylyl cyclase, a heme-containing enzyme, which is directly activated by NO (251). Rapid response of microglia to hypercapnia as demonstrated by calcium fluctuations and generation of perivascular phylopodia, which was P2Y12R-dependent *in vivo*, together with inhibition of hypercapnia-induced cGMP by P2Y12R blockade in CD13-positive, contractile elements (smooth muscle cells and pericytes) ex vivo, suggest that contacting microglial processes may interfere with vasodilation via tentatively different cell types and mediators, which may include NO and adenosine. It should be noted that hypercapnia also increased cGMP in CD13-positive profiles *in vivo*, but the extent of this response was heterogenous, most likely due to the difficulties with precise timing of tissue collection and the rapid hydrolysis of cGMP by phosphodiesterases, which we were able to block effectively in acute brain slices (265). It will also need to be investigated further

in future studies how microglial modulation of NO actions could interact with the production of adenosine or other vasoactive mediators by microglia and other cells in the NVU, which contribute to hypercapnic vasodilation in the brain. For instance, beside NO, prostaglandin pathways are implicated in hypercapnia-induced cerebral vasodilation, which is mediated by cyclic AMP (cAMP). Both cAMP and cGMP levels increase during hypercapnia and activate protein kinase G, thus relax VSMCs (266). It cannot be excluded that these signaling pathways interact during hypercapnic vasodilation. In addition, it has been also reported that astrocyte-derived prostaglandin E_2 play an important role in hypercapnia-evoked vasodilation (69). Microglia may be involved directly or indirectly in prostaglandin-dependent signaling pathways as well. Further investigation is needed to explore the possible mechanisms and interactions through which microglia may modulate hypercapnic vasodilation.

We next asked whether microglia sense and respond to cerebral hypoperfusion. The brain is the most energy-demanding organ in the body with no stores of glucose and high sensitivity to the lack of oxygen. Thus, maintaining stable CBF is critically important for normal CNS functionality. After ischemic stroke, reduced CBF levels may be maintained in the brain even if recanalisation takes place, which is termed the „no-reflow phenomenon". In addition, cerebral hypoperfusion often occurs even before symptom onset in common neurodegenerative diseases such as Alzheimer's and Parkinson's diseases (5). Hence it is important to explore and understand the underlying mechanisms, which emerge as major contributors to the development of several brain disorders. Cerebral blood flow is controlled by feed-forward and feed-back mechanisms that maintain or re-establish optimal oxygen and nutrient supply of neurons in case disturbances of the cardiovascular system occur (267). Adaptation to reduced cerebral perfusion requires vasodilation (268). Unilateral CCAo is an established model of cerebrovascular adaptation to the reduction of perfusion, which is mediated primarily by the activation of feed-back pathways through the collateral circulation (44), while it does not induce neuronal death or BBB injury in rodents (44, 255). Since the cell types in the NVU contacted by microglia regulate CBF (5, 75, 89), we argued that microglia primed by hypoperfusion during the first occlusion would interfere with subsequent vascular adaptation responses and hence elimination of microglia may alter CBF

after repeated CCAo. As supported by previous results showing that microglial process responses around microvessels change proportionally to the level of CBF reduction (254), we found that microglial processes rapidly respond to CCAo. Importantly, the absence of microglia and both genetic and pharmacological blockade of microglial P2Y12R resulted in impaired adaptation to reduced cortical perfusion during repeated CCAo, which strengthens their different roles compared to P2Y12R-negative PVMs (239, 240), as also confirmed by the lack of an effect of PVM depletion. Importantly, our HPLC studies demonstrated that endothelial cells and astrocytes release different purinergic metabolites in response to hypoxia and hypercapnia, both of which occur during hypoperfusion. While we found rapid alterations in microglia-endothelium and microglia-astrocyte interactions after CCAo and hypercapnia, hypoxia and hypercapnia also triggered different purinergic responses in microglia. Although the mechanisms through which different purinergic mediators are released in the NVU remain to be explored. Thus, cell- and stimulus-specific production of vasoactive metabolites may provide means for different vascular adaptation responses, during which microglia may alter CBF via actions on different cell types in the NVU or protect against mild hypoxia-induced vascular leakage (269). Our *in vivo* two-photon imaging data also indicate that individual microglial processes may perform functionally distinct tasks to influence vascular (and other) responses in given microdomains, which is largely supported by the high level of functional autonomy of calcium signaling in microglial processes (270).

Finally, we investigated the inflammatory mechanisms through which microglia may interfere with cerebrovascular responses. Microglia rapidly produce inflammatory cytokines such as IL-1 in response to different pathological stimuli including infections, acute brain injury, cerebral ischemia, hypoperfusion, which also takes place in chronic neurodegenerative diseases (271). Interestingly, we found that the absence of functional IL-1R1 signalling in brain endothelial cells profoundly determines cerebral perfusion within the first hours – a therapeutically critical time window after stroke - suggests that timely blockade of IL-1 actions could have diverse beneficial effects on blood flow recovery and the associated inflammatory response that collectively determine functional outcome. Importantly, these effects of IL-1 on brain endothelial cells are potentially modifiable without

the need for direct CNS actions of a drug, opening up the possibility of targeted anti-IL-1 therapies (e.g. neutralising antibodies) that would not typically show brain penetration (211). It remains unclear how changes in activity and the inflammatory mediators expressed by microglia alter microglia-mediated effects on CBF regulation. The effects of how inflammation shapes microglial phenotypes in the context of CBF regulation will need to be investigated in future studies.

Technical considerations

Because all experimental models have their limitations, we made efforts to use alternative approaches wherever it was possible during these complex studies. For example, prolonged (7 weeks long) treatment with PLX5622 has been found to affect the choroidal vasculature and alter angiogenic growth (171). However, the structural / cellular integrity of blood vessels was not found to be disturbed in the neocortex after 3 weeks of depletion in the present study, as also seen earlier (176, 243). This is also confirmed by our [99mTc]-HMPAO SPECT and [18F]-FDG PET measurements, which are widely used non-invasive methods to assess regional perfusion and glucose metabolism changes, respectively (213, 214). Another possible confounder could be that CX3CR1 (used as a promoter in the CX3CR1^{CreERT2} driver line to generate MicroDREADD^{Dq} mice) may also be expressed by other brain macrophages apart from microglia (37). It is theoretically possible that in addition to microglia, other brain myeloid cells such as meningeal macrophages or PVMs could have contributed to shaping vascular responses in the present study. Importantly, the contribution of microglia to CBF regulation has been confirmed with a number of independent strategies in all three experimental models, including pharmacological and genetic blockade of P2Y12R, which is specific for microglia in the CNS (239). Effective blockade of microglial P2Y12R by PSB0739 injected into the cisterna magna has also been characterized in detail in our previous study (239). Besides, anesthesia is known to influence basal CBF and the extent of CBF responses to different stimuli (272). To minimize this effect of anaesthesia, we applied the same mild ketamine-medetomidine sedation protocol during *in vivo* experiments for comparison and consistency with the exception of the repeated CCAo experiments, which requires deeper anesthesia due to surgery. We also plan to carry out non-invasive *in vivo*

experiments in awake mice, such as whisker stimulation (neurovascular coupling) in future studies. Besides, further studies are needed to investigate whether microglia are implicated in modulation of basal cerebrovascular tone (autoregulation) under physiological conditions. Our unpublished data indicate that the basal cerebrovascular tone is also influenced by microglia, which we have considered by referring to all CBF changes to baseline values of given animals.

Our findings demonstrate the role of microglia in shaping CBF in response to different stimuli in the cerebral cortex. It needs to be investigated, whether microglia-derived signaling pathways operate differently at different segments of the cerebrovascular tree in the cerebral cortex and whether these processes are mediated by different subtypes of microglia cells or not. In addition, our findings may not uniformly translate to other brain regions considering that the signaling mechanisms of CBF modulation may be diverse in different parts of the CNS. For instance it is well-known that signaling pathways of neurovascular coupling are partially different in various brain regions (273). Thus, further studies are needed to clarify the precise mechanisms through which microglia modulate CBF and through which cells of the NVU mediate these processes at different segments of the cerebrovascular tree and in different brain regions.

Clinical significance

We believe that the implication of these studies is far-reaching. Altered microglial activity and impaired CBF or neurovascular coupling precede symptom onset in common brain pathologies such as Alzheimer's disease, Lewy body dementia, idiopathic Parkinson's disease, chronic hypoperfusion, or amyloid angiopathy (5, 75, 89, 253). In addition, it has been demonstrated that chemoregulation is impaired in various brain pathologies including cerebral vasospasm after subarachnoid hemorrhage, ischemic stroke and brain trauma (63). Furthermore, it has been found that NO signaling pathway is crucial to maintain or restore normal physiological CBF after brain injury (274). Thus, dysfunction of microglia could contribute to disease pathophysiology by modulating CBF via endothelial cells or other cells in the NVU. Interestingly, homozygous missense mutations of TREM2 (a microglial receptor) are linked with increased risk of dementia, while Trem2 p.T66M knock-in mice

DOI:10.14753/SE.2023.2742

display an age-dependent reduction in microglial activity, cerebral blood flow and brain glucose metabolism (275). In patients with risk factors for stroke, carotid stenosis, aneurysm, hypertension, chronic vascular inflammation or TIA, altered microglial activity may impact on clinical outcome merely via modulating cerebral perfusion or adaptation to reduced perfusion. As such, microglia could also contribute to ischemic preconditioning, vasospasm after subarachnoid haemorrhage or the „no reflow phenomenon" after cerebral ischemia (276), while microglial surveillance is likely to be disturbed during hypoxia or ischemia, as evidenced in the developing brain (254, 277).

DOI:10.14753/SE.2023.2742

6. Conclusions

Microglia, the resident immune cells of the CNS, play an important role in regulation of central inflammatory processes and BBB functions. It has been evidenced, that microglial dysfunction contribute to development of common brain diseases which are associated with impaired CBF and NVC that often precede symptom onset in neurodegenerative diseases (5, 89). Microglia are highly active in the healthy brain, motile microglial processes dynamically interact with the cells of the CNS and the cerebral vasculature and rapidly respond to changes in their enviroment mediated mainly by purinergic metabolites. Most previous research has focused on investigating microglia-neuron contacts, while the function of microglia-vascular interactions remained vaguely defined. We have discovered that individual microglial cells contact neurons and blood vessels simultaneously in the healthy brain, thus are ideally positioned to sense and influence neurovascular responses. Our anatomical data show that microglia dynamically contact different levels of the vascular tree *in vivo* and form direct purinergic contacts with the cells of the NVU including endothelial cells, astrocytes, pericytes and VSMCs in both the mouse and the human brain, which shape CBF. We found that through these interactions microglia modulate CBF during neurovascular coupling, hypercapnia-induced vasodilation and cerebrovascular adaptation to hypoperfusion. Our results reveal that microglia respond to purinergic signaling in the NVU and to produce adenosine and likely other vasoactive mediators. We demonstrate that the release of purinergic metabolites in response to different vascular stimuli is dependent on the cell type and also on the stimulus used. Microglia may be able to sense different perfusion-related changes in the NVU and interact with different cell types in a compartment-specific manner. Blockade of functional IL-1R1 signalling in brain endothelial cells profoundly determines cerebral perfusion within the first hours suggests that blockade of IL-1 actions could have benefical effects on CBF recovery after stroke. Our findings demonstrate that microglia should be considered as an important modulatory cell type involved in physiological and pathological alterations of cerebral blood flow and understanding their actions may facilitate the discovery of novel treatment opportunities in common neurological disorders.

DOI:10.14753/SE.2023.2742

7. Summary

Microglia, the main immunocompetent cells of the brain, regulate neuronal function in health and disease. Previous studies showed that microglia communicate with the cerebral vasculature during development and in CNS diseases, but their contribution to CBF regulation has remained elusive under both physiological and pathological conditions. Impairment in blood supply of the brain is considered to be a key contributor to development of various brain pathologies such as ischemic stroke and neurodegenerative brain diseases. Understanding the mechanisms which modulate CBF under physiological conditions and the processes that contribute to the progression of brain diseases is essential to develop appropriate therapies. Here, we identify microglia as important modulators of CBF both under physiological conditions and during hypoperfusion. We show that microglia establish direct, dynamic purinergic contacts with cells in the neurovascular unit that shape CBF in both mice and humans. We reveal that the absence of microglia or blockade of microglial P2Y12R substantially impairs neurovascular coupling in mice in the barrel cortex after whisker stimulation. In addition, chemogenetically induced microglial dysfunction results in similarly impaired neurovascular coupling associated with reduced ATP sensitivity. We also reveal that hypercapnia induces rapid microglial calcium changes, P2Y12R-mediated formation of perivascular phylopodia, and microglial adenosine production, while depletion of microglia reduces brain pH and impairs hypercapnia-induced vasodilation. Furthermore, microglial actions modulate vascular cyclic GMP levels but are partially independent of nitric oxide. Using a well-established common carotid artery occlusion model which we have further developed to achieve repeated occlusions, we demonstrate that microglial dysfunction markedly impairs P2Y12R-mediated cerebrovascular adaptation to occlusion, resulting in hypoperfusion in the cerebral cortex. Finally, we show that conditional deletion of IL-1R1 in brain endothelial cells lead to improved CBF after cerebral ischemia in mice. Overall, our data reveal a previously unrecognized role for microglia in CBF modulation and for endothelial IL-1R1 in ischemic stroke. These results may facilitate the development of novel diagnostic tools and treatment opportunities in common cerebrovascular diseases.

DOI:10.14753/SE.2023.2742

8. Összefoglalás

A mikroglia a központi idegrendszer rezidens immunsejtje, amely fontos szerepet tölt be a centrális gyulladásos folyamatok szabályozásában. Megváltozott működése a gyakori idegrendszeri betegségek, mint a stroke és a krónikus neurodegeneratív betegségek kialakulásában is szerepet játszik. Ezen betegségek hátterében gyakran megfigyelhető a neurovaszkuláris egység funkcionális károsodása. A közelmúlt kutatásai rávilágítottak, hogy a mikroglia nemcsak az idegsejtek működését monitorozza, hanem az agyi erek állapotát is felügyeli, azonban a mikroglia-vaszkuláris interakciók funkciója eddig nagyrészt tisztázatlan maradt. Kutatásunk során feltártuk, hogy a mikroglia kiemelkedően fontos szerepet tölt be az agyi véráramlás modulálásában. Megmutattuk, hogy a mikroglia mind egerekben, mind az emberi agyban közvetlen, dinamikus purinerg kapcsolatokat alakít ki a neurovaszkuláris egység sejtjeivel, mely kapcsolatokon keresztül képes modulálni az agyi perfúziót. A mikroglia szelektív eliminációja vagy a mikrogliális P2Y12 receptor gátlása a neurovaszkuláris csatolás károsodását okozza. Kimutattuk, hogy kemogenetikus stimuláció hatására a mikroglia nyúlványok motilitása és az ATP-re adott válaszkészsége csökken, ami együtt jár a neurovaszkuláris csatolás diszfunkciójával. Továbbá hiperkapnia-indukálta vazodilatáció közben gyors intracelluláris kálcium változásokat figyeltünk meg a mikroglia sejtekben, valamint jelentős mértékű mikrogliális filopódium képződést az erek körül. A mikroglia depléciója vagy a mikrogliális P2Y12 receptor gátlása csökkent hiperkapnia-indukálta vazodilatációt eredményezett. A mikrogliának fontos szerepe van a hiperkapnia-indukálta vazodilatáció modulálásában, ami részben adenozin révén, részben cGMP jelátviteli útvonalon keresztül történik. Megmutattuk, hogy a mikroglia modulálja az agyi pH-t. Továbbá egy általunk kifejlesztett, iszkémiát nem okozó, arteria carotis communis (CCA) okklúziós modellt alkalmazva megmutattuk, hogy a mikroglia fontos szerepet tölt be a hipoperfúzióhoz történő adaptációban. Végül kimutattuk, hogy az endoteliális IL-1R1 jelátviteli útvonal blokkolása jelentős mértékben javítja az agyi perfúziót iszkémiát követően. A mikroglia által irányított agyi véráramlás modulálási mechanizmusok megértése és feltárása kiemelkedően fontos lehet az agyi keringési zavarokkal társuló idegrendszeri betegségek hatékony kezeléséhez.

9. References

1. Kety SS. The general metabolism of the brain in vivo. In: Richter D (editor), Metabolism of the nervous system. Pergamon Press, London, 1957: 221-237.
2. Sokoloff L. (1960) Quantitative measurements of cerebral blood flow in man. Methods Med Res, 8: 253-261.
3. Moskowitz MA, Lo EH, Iadecola C. (2010) The science of stroke: mechanisms in search of treatments. Neuron, 67: 181-198.
4. World Health Organization. WHO Fact sheets. The top 10 causes of death [Internet]. 2020 [updated 2020 December 9; cited 2022 July 12.]. Available from: https://www.who.int/news-room/fact-sheets/detail/the-top-10-causes-of-death.
5. Iadecola C. (2017) The Neurovascular Unit Coming of Age: A Journey through Neurovascular Coupling in Health and Disease. Neuron, 96: 17-42.
6. Zlokovic BV. (2005) Neurovascular mechanisms of Alzheimer's neurodegeneration. Trends Neurosci, 28: 202-208.
7. Begley DJ, Brightman MW. (2003) Structural and functional aspects of the blood-brain barrier. Prog Drug Res, 61: 39-78.
8. Agarwal N, Carare RO. (2020) Cerebral Vessels: An Overview of Anatomy, Physiology, and Role in the Drainage of Fluids and Solutes. Front Neurol, 11: 611485.
9. Berthiaume AA, Hartmann DA, Majesky MW, Bhat NR, Shih AY. (2018) Pericyte Structural Remodeling in Cerebrovascular Health and Homeostasis. Front Aging Neurosci, 10: 210.
10. Cipolla MJ. The Cerebral Circulation. Morgan & Claypool Life Sciences, San Rafael (CA), 2009: 1-59. Copyright © 2010 by Morgan & Claypool Life Sciences.
11. Schröder H, Moser N, Huggenberger S. The Mouse Circle of Willis. In: Schröder H, Moser N, Huggenberger S (editors), Neuroanatomy of the Mouse: An Introduction. Springer, Cham, 2020: 333-340.
12. Manual M. Supplying the Brain With Blood [Internet]. 2022 [updated 2022; cited 2022 July 13]. Available from:

https://www.msdmanuals.com/home/multimedia/figure/supplying-the-brain-with-blood.

13. Lecturio. Cerebrovascular System: Anatomy, Arterial supply [Internet]. 2022 [updated 2022 April 07; cited 2022 July 13]. Available from: https://www.lecturio.com/concepts/cerebrovascular-system/#lecturio-toc__Arterial%20Supply.
14. Biorender. Mouse circulatory system (circle of willis, on brain) [Internet]. 2022 [updated 2022; cited 2022 July 13]. Available from: https://biorender.com/icon/species/rodents/mouse-circle-of-willis-on-brain/.
15. Willis T. Cerebri anatome: cui accessit Nervorum descriptio et usus. Martyn & Allestry, London, 1664: 1-184.
16. Kramer SP. (1912) ON THE FUNCTION OF THE CIRCLE OF WILLIS. J Exp Med, 15: 348-364.
17. Chandra A, Li W, Stone C, Geng X, Ding Y. (2017) The cerebral circulation and cerebrovascular disease I: Anatomy. Brain Circulation, 3: 45-56.
18. Biorender. Mouse lateral brain (with arteries) [Internet]. 2022 [updated 2022; cited 2022 July 13]. Available from: https://biorender.com/icon/species/rodents/mouse-brain-lateral-with-arteries-2/.
19. Biorender. Mouse brain (dorsal, with arteries) [Internet]. 2022 [updated 2022; cited 2022 July 13]. Available from: https://biorender.com/icon/species/rodents/mouse-brain-dorsal-with-arteries/.
20. Iqbal S. (2013) A comprehensive study of the anatomical variations of the circle of willis in adult human brains. J Clin Diagn Res, 7: 2423-2427.
21. Schaller B. (2004) Physiology of cerebral venous blood flow: from experimental data in animals to normal function in humans. Brain Res Brain Res Rev, 46: 243-260.
22. Kilic T, Akakin A. (2008) Anatomy of cerebral veins and sinuses. Front Neurol Neurosci, 23: 4-15.
23. Weis S. SM, Dunzinger A., Voglmayr E., Aichholzer M., Kleiser R., Strasser P. Venous Drainage of the Brain. In: Pfeffier B (editor), Imaging Brain Diseases. Springer, Vienna, 2019: 221-224.

24. Moll S, Waldron B. (2014) Cerebral and sinus vein thrombosis. Circulation, 130: e68-70.
25. Low RJ, Gu Y, Tank DW. (2014) Cellular resolution optical access to brain regions in fissures: imaging medial prefrontal cortex and grid cells in entorhinal cortex. Proc Natl Acad Sci U S A, 111: 18739-18744.
26. Owens T, Bechmann I, Engelhardt B. (2008) Perivascular spaces and the two steps to neuroinflammation. J Neuropathol Exp Neurol, 67: 1113-1121.
27. Thomsen MS, Routhe LJ, Moos T. (2017) The vascular basement membrane in the healthy and pathological brain. J Cereb Blood Flow Metab, 37: 3300-3317.
28. Engelhardt B, Vajkoczy P, Weller RO. (2017) The movers and shapers in immune privilege of the CNS. Nat Immunol, 18: 123-131.
29. Vanlandewijck M, He L, Mae MA, Andrae J, Ando K, Del Gaudio F, Nahar K, Lebouvier T, Lavina B, Gouveia L, Sun Y, Raschperger E, Rasanen M, Zarb Y, Mochizuki N, Keller A, Lendahl U, Betsholtz C. (2018) A molecular atlas of cell types and zonation in the brain vasculature. Nature, 554: 475-480.
30. Zi-Sen Z, He-Nan Z, Shuang-Shuang H, Ming-Ying X, Tao L, Liang-Ming L. (2020) Research advances in pericyte function and their roles in diseases. Chin J Traumatol, 23: 89-95.
31. Erdener SE, Dalkara T. (2019) Small Vessels Are a Big Problem in Neurodegeneration and Neuroprotection. Front Neurol, 10: 889.
32. Claassen J, Thijssen DHJ, Panerai RB, Faraci FM. (2021) Regulation of cerebral blood flow in humans: physiology and clinical implications of autoregulation. Physiol Rev, 101: 1487-1559.
33. Gould IG, Tsai P, Kleinfeld D, Linninger A. (2017) The capillary bed offers the largest hemodynamic resistance to the cortical blood supply. J Cereb Blood Flow Metab, 37: 52-68.
34. Frisbee BHaJ. Cerebral Vascular Tone Regulation: Integration and Impact of Disease. In: Kaneez FS, Seyed SSS, Nazar LB (editors), Basic and Clinical Understanding of Microcirculation. IntechOpen, London, 2020: 3-9.

35. Klabunde RE. Vascular function. In: Taylor C (editor), Cardiovascular Physiology Concepts. Wolters Kluwer, Philadelphia, 2021: 98-112.
36. Ashby JW, Mack JJ. (2021) Endothelial Control of Cerebral Blood Flow. Am J Pathol, 191: 1906-1916.
37. Filosa JA, Morrison HW, Iddings JA, Du W, Kim KJ. (2016) Beyond neurovascular coupling, role of astrocytes in the regulation of vascular tone. Neuroscience, 323: 96-109.
38. Hamel E. (2006) Perivascular nerves and the regulation of cerebrovascular tone. J Appl Physiol, 100: 1059-1064.
39. Mishra A. (2017) Binaural blood flow control by astrocytes: listening to synapses and the vasculature. J Physiol, 595: 1885-1902.
40. Hoiland RL, Fisher JA, Ainslie PN. (2019) Regulation of the Cerebral Circulation by Arterial Carbon Dioxide. Compr Physiol, 9: 1101-1154.
41. Payne S. Physiological Basis. In: Payne S (editor), Cerebral Autoregulation: Control of Blood Flow in the Brain. Springer, Cham, 2016: 1-18.
42. ter Laan M, van Dijk JM, Elting JW, Staal MJ, Absalom AR. (2013) Sympathetic regulation of cerebral blood flow in humans: a review. Br J Anaesth, 111: 361-367.
43. Sharp FR, Bernaudin M. (2004) HIF1 and oxygen sensing in the brain. Nat Rev Neurosci, 5: 437-448.
44. Polycarpou A, Hricisak L, Iring A, Safar D, Ruisanchez E, Horvath B, Sandor P, Benyo Z. (2016) Adaptation of the cerebrocortical circulation to carotid artery occlusion involves blood flow redistribution between cortical regions and is independent of eNOS. Am J Physiol-Heart C, 311: H972-H80.
45. Bergfeld GR, Forrester T. (1992) Release of ATP from human erythrocytes in response to a brief period of hypoxia and hypercapnia. Cardiovasc Res, 26: 40-47.
46. Ellsworth ML, Ellis CG, Goldman D, Stephenson AH, Dietrich HH, Sprague RS. (2009) Erythrocytes: oxygen sensors and modulators of vascular tone. Physiology (Bethesda), 24: 107-116.
47. Vestergaard MB, Lindberg U, Aachmann-Andersen NJ, Lisbjerg K, Christensen SJ, Law I, Rasmussen P, Olsen NV, Larsson HBW. (2016) Acute hypoxia increases the cerebral

metabolic rate - a magnetic resonance imaging study. J Cereb Blood Flow Metab, 36: 1046-1058.

48. Berger C, von Kummer R. (1998) Does NO regulate the cerebral blood flow response in hypoxia? Acta Neurol Scand, 97: 118-125.
49. Takuwa H, Matsuura T, Bakalova R, Obata T, Kanno I. (2010) Contribution of nitric oxide to cerebral blood flow regulation under hypoxia in rats. J Physiol Sci, 60: 399-406.
50. Phillis JW. (2004) Adenosine and adenine nucleotides as regulators of cerebral blood flow: roles of acidosis, cell swelling, and KATP channels. Crit Rev Neurobiol, 16: 237-270.
51. Hoffman WE, Albrecht RF, Miletich DJ. (1984) The role of adenosine in CBF increases during hypoxia in young vs aged rats. Stroke, 15: 124-129.
52. Reivich M. (1964) Arterial Pco2 and Cerebral Hemodynamics. Am J Physiol, 206: 25-35.
53. Kety SS, Schmidt CF. (1948) The Effects of Altered Arterial Tensions of Carbon Dioxide and Oxygen on Cerebral Blood Flow and Cerebral Oxygen Consumption of Normal Young Men. J Clin Invest, 27: 484-492.
54. Wei EP, Kontos HA, Patterson JL, Jr. (1980) Dependence of pial arteriolar response to hypercapnia on vessel size. Am J Physiol, 238: 697-703.
55. Kidoguchi K, Tamaki M, Mizobe T, Koyama J, Kondoh T, Kohmura E, Sakurai T, Yokono K, Umetani K. (2006) In vivo X-ray angiography in the mouse brain using synchrotron radiation. Stroke, 37: 1856-1861.
56. Lassen NA. (1968) Brain extracellular pH: the main factor controlling cerebral blood flow. Scand J Clin Lab Invest, 22: 247-251.
57. Yoon S, Zuccarello M, Rapoport R. (2012) pCO2 and pH regulation of cerebral blood flow. Frontiers in Physiology, 3: 365.
58. Wang Q, Paulson OB, Lassen NA. (1992) Effect of nitric oxide blockade by NG-nitro-L-arginine on cerebral blood flow response to changes in carbon dioxide tension. J Cereb Blood Flow Metab, 12: 947-953.
59. Iadecola C, Zhang F. (1996) Permissive and obligatory roles of NO in cerebrovascular responses to hypercapnia and acetylcholine. Am J Physiol, 271: R990-1001.

60. Niwa K, Lindauer U, Villringer A, Dirnagl U. (1993) Blockade of nitric oxide synthesis in rats strongly attenuates the CBF response to extracellular acidosis. J Cereb Blood Flow Metab, 13: 535-539.
61. Faraci FM, Brian JE, Jr. (1994) Nitric oxide and the cerebral circulation. Stroke, 25: 692-703.
62. Iadecola C. (1992) Does nitric oxide mediate the increases in cerebral blood flow elicited by hypercapnia? Proc Natl Acad Sci U S A, 89: 3913-3916.
63. Fathi AR, Yang C, Bakhtian KD, Qi M, Lonser RR, Pluta RM. (2011) Carbon dioxide influence on nitric oxide production in endothelial cells and astrocytes: cellular mechanisms. Brain Res, 1386: 50-57.
64. Archer SL, Huang JM, Hampl V, Nelson DP, Shultz PJ, Weir EK. (1994) Nitric oxide and cGMP cause vasorelaxation by activation of a charybdotoxin-sensitive K channel by cGMP-dependent protein kinase. Proc Natl Acad Sci U S A, 91: 7583-7587.
65. Irikura K, Maynard KI, Lee WS, Moskowitz MA. (1994) L-NNA decreases cortical hyperemia and brain cGMP levels following CO2 inhalation in Sprague-Dawley rats. Am J Physiol, 267: H837-843.
66. Faraci FM, Taugher RJ, Lynch C, Fan R, Gupta S, Wemmie JA. (2019) Acid-Sensing Ion Channels: Novel Mediators of Cerebral Vascular Responses. Circ Res, 125: 907-920.
67. Niwa K, Haensel C, Ross ME, Iadecola C. (2001) Cyclooxygenase-1 participates in selected vasodilator responses of the cerebral circulation. Circ Res, 88: 600-608.
68. Vane JR, Bakhle YS, Botting RM. (1998) CYCLOOXYGENASES 1 AND 2. Annual Review of Pharmacology and Toxicology, 38: 97-120.
69. Howarth C, Sutherland B, Choi HB, Martin C, Lind BL, Khennouf L, LeDue JM, Pakan JM, Ko RW, Ellis-Davies G, Lauritzen M, Sibson NR, Buchan AM, MacVicar BA. (2017) A Critical Role for Astrocytes in Hypercapnic Vasodilation in Brain. J Neurosci, 37: 2403-2414.
70. Phillis JW, DeLong RE. (1987) An involvement of adenosine in cerebral blood flow regulation during hypercapnia. Gen Pharmacol, 18: 133-139.

71. Roy CS, Sherrington CS. (1890) On the Regulation of the Blood-supply of the Brain. J Physiol, 11: 85-158.17.
72. Lassen NA, Ingvar DH, Skinhoj E. (1978) Brain function and blood flow. Sci Am, 239: 62-71.
73. Shetty PK, Galeffi F, Turner DA. (2012) Cellular Links between Neuronal Activity and Energy Homeostasis. Front Pharmacol, 3: 43.
74. Silva AC, Lee SP, Iadecola C, Kim SG. (2000) Early temporal characteristics of cerebral blood flow and deoxyhemoglobin changes during somatosensory stimulation. J Cereb Blood Flow Metab, 20: 201-206.
75. Attwell D, Buchan AM, Charpak S, Lauritzen M, Macvicar BA, Newman EA. (2010) Glial and neuronal control of brain blood flow. Nature, 468: 232-243.
76. Ko KR, Ngai AC, Winn HR. (1990) Role of adenosine in regulation of regional cerebral blood flow in sensory cortex. Am J Physiol, 259: H1703-1708.
77. Freeman RD, Li B. (2016) Neural-metabolic coupling in the central visual pathway. Philos Trans R Soc Lond B Biol Sci, 371: 20150357.
78. Phillis JW. (1989) Adenosine in the control of the cerebral circulation. Cerebrovasc Brain Metab Rev, 1: 26-54.
79. Cauli B, Hamel E. (2010) Revisiting the role of neurons in neurovascular coupling. Front Neuroenergetics, 2: 9.
80. Zonta M, Angulo MC, Gobbo S, Rosengarten B, Hossmann KA, Pozzan T, Carmignoto G. (2003) Neuron-to-astrocyte signaling is central to the dynamic control of brain microcirculation. Nat Neurosci, 6: 43-50.
81. Filosa JA, Bonev AD, Straub SV, Meredith AL, Wilkerson MK, Aldrich RW, Nelson MT. (2006) Local potassium signaling couples neuronal activity to vasodilation in the brain. Nat Neurosci, 9: 1397-1403.
82. Metea MR, Newman EA. (2006) Glial cells dilate and constrict blood vessels: a mechanism of neurovascular coupling. J Neurosci, 26: 2862-2870.
83. MacVicar BA, Newman EA. (2015) Astrocyte regulation of blood flow in the brain. Cold Spring Harb Perspect Biol, 7: a020388.

84. Pelligrino DA, Vetri F, Xu HL. (2011) Purinergic mechanisms in gliovascular coupling. Semin Cell Dev Biol, 22: 229-236.
85. Longden TA, Hill-Eubanks DC, Nelson MT. (2016) Ion channel networks in the control of cerebral blood flow. J Cereb Blood Flow Metab, 36: 492-512.
86. Abdulaal WH, Walker CR, Costello R, Redondo-Castro E, Mufazalov IA, Papaemmanouil A, Rothwell NJ, Allan SM, Waisman A, Pinteaux E, Muller W. (2016) Characterization of a conditional interleukin-1 receptor 1 mouse mutant using the Cre/LoxP system. Eur J Immunol, 46: 912-918.
87. Grant RI, Hartmann DA, Underly RG, Berthiaume AA, Bhat NR, Shih AY. (2019) Organizational hierarchy and structural diversity of microvascular pericytes in adult mouse cortex. J Cereb Blood Flow Metab, 39: 411-425.
88. Hall CN, Reynell C, Gesslein B, Hamilton NB, Mishra A, Sutherland BA, O'Farrell FM, Buchan AM, Lauritzen M, Attwell D. (2014) Capillary pericytes regulate cerebral blood flow in health and disease. Nature, 508: 55-60.
89. Kisler K, Nelson AR, Rege SV, Ramanathan A, Wang Y, Ahuja A, Lazic D, Tsai PS, Zhao Z, Zhou Y, Boas DA, Sakadzic S, Zlokovic BV. (2017) Pericyte degeneration leads to neurovascular uncoupling and limits oxygen supply to brain. Nat Neurosci, 20: 406-416.
90. Hartmann DA, Berthiaume AA, Grant RI, Harrill SA, Koski T, Tieu T, McDowell KP, Faino AV, Kelly AL, Shih AY. (2021) Brain capillary pericytes exert a substantial but slow influence on blood flow. Nat Neurosci, 24: 633-645.
91. Iadecola C, Yang G, Ebner TJ, Chen G. (1997) Local and propagated vascular responses evoked by focal synaptic activity in cerebellar cortex. J Neurophysiol, 78: 651-659.
92. Bagher P, Segal SS. (2011) Regulation of blood flow in the microcirculation: role of conducted vasodilation. Acta Physiol (Oxf), 202: 271-284.
93. Figueroa XF, Duling BR. (2009) Gap junctions in the control of vascular function. Antioxid Redox Signal, 11: 251-66.
94. de Wit C, Griffith TM. (2010) Connexins and gap junctions in the EDHF phenomenon and conducted vasomotor responses. Pflugers Arch, 459: 897-914.

95. Tallini YN, Brekke JF, Shui B, Doran R, Hwang SM, Nakai J, Salama G, Segal SS, Kotlikoff MI. (2007) Propagated endothelial Ca2+ waves and arteriolar dilation in vivo: measurements in Cx40BAC GCaMP2 transgenic mice. Circ Res, 101: 1300-1309.
96. Chen BR, Kozberg MG, Bouchard MB, Shaik MA, Hillman EM. (2014) A critical role for the vascular endothelium in functional neurovascular coupling in the brain. J Am Heart Assoc, 3: e000787.
97. Butovsky O, Jedrychowski MP, Moore CS, Cialic R, Lanser AJ, Gabriely G, Koeglsperger T, Dake B, Wu PM, Doykan CE, Fanek Z, Liu L, Chen Z, Rothstein JD, Ransohoff RM, Gygi SP, Antel JP, Weiner HL. (2014) Identification of a unique TGF-beta-dependent molecular and functional signature in microglia. Nat Neurosci, 17: 131-143.
98. Kierdorf K, Masuda T, Jordao MJC, Prinz M. (2019) Macrophages at CNS interfaces: ontogeny and function in health and disease. Nat Rev Neurosci, 20: 547-562.
99. Ginhoux F, Greter M, Leboeuf M, Nandi S, See P, Gokhan S, Mehler MF, Conway SJ, Ng LG, Stanley ER, Samokhvalov IM, Merad M. (2010) Fate mapping analysis reveals that adult microglia derive from primitive macrophages. Science, 330: 841-845.
100. Schulz C, Gomez Perdiguero E, Chorro L, Szabo-Rogers H, Cagnard N, Kierdorf K, Prinz M, Wu B, Jacobsen SE, Pollard JW, Frampton J, Liu KJ, Geissmann F. (2012) A lineage of myeloid cells independent of Myb and hematopoietic stem cells. Science, 336: 86-90.
101. Kierdorf K, Erny D, Goldmann T, Sander V, Schulz C, Perdiguero EG, Wieghofer P, Heinrich A, Riemke P, Holscher C, Muller DN, Luckow B, Brocker T, Debowski K, Fritz G, Opdenakker G, Diefenbach A, Biber K, Heikenwalder M, Geissmann F, Rosenbauer F, Prinz M. (2013) Microglia emerge from erythromyeloid precursors via Pu.1- and Irf8-dependent pathways. Nat Neurosci, 16: 273-280.
102. Ajami B, Bennett JL, Krieger C, Tetzlaff W, Rossi FM. (2007) Local self-renewal can sustain CNS microglia maintenance and function throughout adult life. Nat Neurosci, 10: 1538-1543.
103. Tay TL, Mai D, Dautzenberg J, Fernandez-Klett F, Lin G, Sagar, Datta M, Drougard A, Stempfl T, Ardura-Fabregat A, Staszewski O, Margineanu A, Sporbert A, Steinmetz

LM, Pospisilik JA, Jung S, Priller J, Grun D, Ronneberger O, Prinz M. (2017) A new fate mapping system reveals context-dependent random or clonal expansion of microglia. Nat Neurosci, 20: 793-803.

104. Fuger P, Hefendehl JK, Veeraraghavalu K, Wendeln AC, Schlosser C, Obermuller U, Wegenast-Braun BM, Neher JJ, Martus P, Kohsaka S, Thunemann M, Feil R, Sisodia SS, Skodras A, Jucker M. (2017) Microglia turnover with aging and in an Alzheimer's model via long-term in vivo single-cell imaging. Nat Neurosci, 20: 1371-1376.
105. Huang Y, Xu Z, Xiong S, Sun F, Qin G, Hu G, Wang J, Zhao L, Liang YX, Wu T, Lu Z, Humayun MS, So KF, Pan Y, Li N, Yuan TF, Rao Y, Peng B. (2018) Repopulated microglia are solely derived from the proliferation of residual microglia after acute depletion. Nat Neurosci, 21: 530-540.
106. Askew K, Li K, Olmos-Alonso A, Garcia-Moreno F, Liang Y, Richardson P, Tipton T, Chapman MA, Riecken K, Beccari S, Sierra A, Molnar Z, Cragg MS, Garaschuk O, Perry VH, Gomez-Nicola D. (2017) Coupled Proliferation and Apoptosis Maintain the Rapid Turnover of Microglia in the Adult Brain. Cell Rep, 18: 391-405.
107. Goldmann T, Wieghofer P, Jordão MJC, Prutek F, Hagemeyer N, Frenzel K, Amann LS, Staszewski O, Kierdorf K, Krueger M, Locatelli G, Hochgerner H, Zeiser R, Epelman S, Geissmann F, Priller J, Rossi FMV, Bechmann I, Kerschensteiner M, Linnarsson S, Jung S, Prinz M. (2016) Origin, fate and dynamics of macrophages at central nervous system interfaces. Nature Immunology, 17: 797-805.
108. Kierdorf K, Prinz M. (2017) Microglia in steady state. J Clin Invest, 127: 3201-3209.
109. Van Hove H, Martens L, Scheyltjens I, De Vlaminck K, Pombo Antunes AR, De Prijck S, Vandamme N, De Schepper S, Van Isterdael G, Scott CL, Aerts J, Berx G, Boeckxstaens GE, Vandenbroucke RE, Vereecke L, Moechars D, Guilliams M, Van Ginderachter JA, Saeys Y, Movahedi K. (2019) A single-cell atlas of mouse brain macrophages reveals unique transcriptional identities shaped by ontogeny and tissue environment. Nat Neurosci, 22: 1021-1035.
110. Katusic ZS, Austin SA. (2016) Neurovascular Protective Function of Endothelial Nitric Oxide- Recent Advances. Circ J, 80: 1499-1503.

111. Verney C, Monier A, Fallet-Bianco C, Gressens P. (2010) Early microglial colonization of the human forebrain and possible involvement in periventricular white-matter injury of preterm infants. J Anat, 217: 436-448.
112. Kriegstein A, Alvarez-Buylla A. (2009) The glial nature of embryonic and adult neural stem cells. Annu Rev Neurosci, 32: 149-184.
113. Gomez-Nicola D, Fransen NL, Suzzi S, Perry VH. (2013) Regulation of microglial proliferation during chronic neurodegeneration. J Neurosci, 33: 2481-2493.
114. Erblich B, Zhu L, Etgen AM, Dobrenis K, Pollard JW. (2011) Absence of colony stimulation factor-1 receptor results in loss of microglia, disrupted brain development and olfactory deficits. PLoS One, 6: e26317.
115. Nandi S, Gokhan S, Dai XM, Wei S, Enikolopov G, Lin H, Mehler MF, Stanley ER. (2012) The CSF-1 receptor ligands IL-34 and CSF-1 exhibit distinct developmental brain expression patterns and regulate neural progenitor cell maintenance and maturation. Dev Biol, 367: 100-113.
116. Oosterhof N, Chang IJ, Karimiani EG, Kuil LE, Jensen DM, Daza R, Young E, Astle L, van der Linde HC, Shivaram GM, Demmers J, Latimer CS, Keene CD, Loter E, Maroofian R, van Ham TJ, Hevner RF, Bennett JT. (2019) Homozygous Mutations in CSF1R Cause a Pediatric-Onset Leukoencephalopathy and Can Result in Congenital Absence of Microglia. Am J Hum Genet, 104: 936-947.
117. Walton NM, Sutter BM, Laywell ED, Levkoff LH, Kearns SM, Marshall GP, 2nd, Scheffler B, Steindler DA. (2006) Microglia instruct subventricular zone neurogenesis. Glia, 54: 815-825.
118. Cunningham CL, Martinez-Cerdeno V, Noctor SC. (2013) Microglia regulate the number of neural precursor cells in the developing cerebral cortex. J Neurosci, 33: 4216-4233.
119. Pont-Lezica L, Beumer W, Colasse S, Drexhage H, Versnel M, Bessis A. (2014) Microglia shape corpus callosum axon tract fasciculation: functional impact of prenatal inflammation. Eur J Neurosci, 39: 1551-1557.

120. Squarzoni P, Oller G, Hoeffel G, Pont-Lezica L, Rostaing P, Low D, Bessis A, Ginhoux F, Garel S. (2014) Microglia modulate wiring of the embryonic forebrain. Cell Rep, 8: 1271-1279.
121. Miyamoto A, Wake H, Ishikawa AW, Eto K, Shibata K, Murakoshi H, Koizumi S, Moorhouse AJ, Yoshimura Y, Nabekura J. (2016) Microglia contact induces synapse formation in developing somatosensory cortex. Nat Commun, 7: 12540.
122. Paolicelli RC, Bolasco G, Pagani F, Maggi L, Scianni M, Panzanelli P, Giustetto M, Ferreira TA, Guiducci E, Dumas L, Ragozzino D, Gross CT. (2011) Synaptic pruning by microglia is necessary for normal brain development. Science, 333: 1456-1458.
123. Schafer DP, Lehrman EK, Kautzman AG, Koyama R, Mardinly AR, Yamasaki R, Ransohoff RM, Greenberg ME, Barres BA, Stevens B. (2012) Microglia sculpt postnatal neural circuits in an activity and complement-dependent manner. Neuron, 74: 691-705.
124. Ueno M, Fujita Y, Tanaka T, Nakamura Y, Kikuta J, Ishii M, Yamashita T. (2013) Layer V cortical neurons require microglial support for survival during postnatal development. Nat Neurosci, 16: 543-551.
125. Frost JL, Schafer DP. (2016) Microglia: Architects of the Developing Nervous System. Trends Cell Biol, 26: 587-597.
126. Nimmerjahn A, Kirchhoff F, Helmchen F. (2005) Resting microglial cells are highly dynamic surveillants of brain parenchyma in vivo. Science, 308: 1314-1318.
127. Eyo UB, Mo M, Yi MH, Murugan M, Liu J, Yarlagadda R, Margolis DJ, Xu P, Wu LJ. (2018) P2Y12R-Dependent Translocation Mechanisms Gate the Changing Microglial Landscape. Cell Rep, 23: 959-966.
128. Stowell RD, Wong EL, Batchelor HN, Mendes MS, Lamantia CE, Whitelaw BS, Majewska AK. (2018) Cerebellar microglia are dynamically unique and survey Purkinje neurons in vivo. Dev Neurobiol, 78: 627-644.
129. Davalos D, Grutzendler J, Yang G, Kim JV, Zuo Y, Jung S, Littman DR, Dustin ML, Gan WB. (2005) ATP mediates rapid microglial response to local brain injury in vivo. Nat Neurosci, 8: 752-758.
130. Posfai B, Cserep C, Orsolits B, Denes A. (2019) New Insights into Microglia-Neuron Interactions: A Neuron's Perspective. Neuroscience, 405: 103-117.

131. Deng W, Aimone JB, Gage FH. (2010) New neurons and new memories: how does adult hippocampal neurogenesis affect learning and memory? Nature Reviews Neuroscience, 11: 339-350.
132. Sierra A, Encinas JM, Deudero JJP, Chancey JH, Enikolopov G, Overstreet-Wadiche LS, Tsirka SE, Maletic-Savatic M. (2010) Microglia shape adult hippocampal neurogenesis through apoptosis-coupled phagocytosis. Cell Stem Cell, 7: 483-495.
133. Stefani J, Tschesnokowa O, Parrilla M, Robaye B, Boeynaems J-M, Acker-Palmer A, Zimmermann H, Gampe K. (2018) Disruption of the Microglial ADP Receptor P2Y13 Enhances Adult Hippocampal Neurogenesis. Frontiers in Cellular Neuroscience, 12: 134.
134. Maggi L, Scianni M, Branchi I, D'Andrea I, Lauro C, Limatola C. (2011) CX3CR1 Deficiency Alters Hippocampal-Dependent Plasticity Phenomena Blunting the Effects of Enriched Environment. Frontiers in Cellular Neuroscience, 5: 22.
135. Bachstetter AD, Morganti JM, Jernberg J, Schlunk A, Mitchell SH, Brewster KW, Hudson CE, Cole MJ, Harrison JK, Bickford PC, Gemma C. (2011) Fractalkine and CX 3 CR1 regulate hippocampal neurogenesis in adult and aged rats. Neurobiol Aging, 32: 2030-2044.
136. Tremblay ME, Lowery RL, Majewska AK. (2010) Microglial interactions with synapses are modulated by visual experience. PLoS Biol, 8: e1000527.
137. Brioschi S, d'Errico P, Amann LS, Janova H, Wojcik SM, Meyer-Luehmann M, Rajendran L, Wieghofer P, Paolicelli RC, Biber K. (2020) Detection of Synaptic Proteins in Microglia by Flow Cytometry. Front Mol Neurosci, 13: 149.
138. Cornell J, Salinas S, Huang HY, Zhou M. (2022) Microglia regulation of synaptic plasticity and learning and memory. Neural Regen Res, 17: 705-716.
139. Anderson SR, Zhang J, Steele MR, Romero CO, Kautzman AG, Schafer DP, Vetter ML. (2019) Complement Targets Newborn Retinal Ganglion Cells for Phagocytic Elimination by Microglia. J Neurosci, 39: 2025-2040.
140. Badimon A, Strasburger HJ, Ayata P, Chen X, Nair A, Ikegami A, Hwang P, Chan AT, Graves SM, Uweru JO, Ledderose C, Kutlu MG, Wheeler MA, Kahan A, Ishikawa M, Wang YC, Loh YE, Jiang JX, Surmeier DJ, Robson SC, Junger WG, Sebra R, Calipari

ES, Kenny PJ, Eyo UB, Colonna M, Quintana FJ, Wake H, Gradinaru V, Schaefer A. (2020) Negative feedback control of neuronal activity by microglia. Nature, 586: 417-423.

141. Gunner G, Cheadle L, Johnson KM, Ayata P, Badimon A, Mondo E, Nagy MA, Liu L, Bemiller SM, Kim KW, Lira SA, Lamb BT, Tapper AR, Ransohoff RM, Greenberg ME, Schaefer A, Schafer DP. (2019) Sensory lesioning induces microglial synapse elimination via ADAM10 and fractalkine signaling. Nat Neurosci, 22: 1075-1088.
142. Filipello F, Morini R, Corradini I, Zerbi V, Canzi A, Michalski B, Erreni M, Markicevic M, Starvaggi-Cucuzza C, Otero K, Piccio L, Cignarella F, Perrucci F, Tamborini M, Genua M, Rajendran L, Menna E, Vetrano S, Fahnestock M, Paolicelli RC, Matteoli M. (2018) The Microglial Innate Immune Receptor TREM2 Is Required for Synapse Elimination and Normal Brain Connectivity. Immunity, 48: 979-991.e8.
143. Lyons A, Minogue AM, Jones RS, Fitzpatrick O, Noonan J, Campbell VA, Lynch MA. (2017) Analysis of the Impact of CD200 on Phagocytosis. Mol Neurobiol, 54: 5730-5739.
144. Lehrman EK, Wilton DK, Litvina EY, Welsh CA, Chang ST, Frouin A, Walker AJ, Heller MD, Umemori H, Chen C, Stevens B. (2018) CD47 Protects Synapses from Excess Microglia-Mediated Pruning during Development. Neuron, 100: 120-134.e6.
145. Rogers JT, Morganti JM, Bachstetter AD, Hudson CE, Peters MM, Grimmig BA, Weeber EJ, Bickford PC, Gemma C. (2011) CX3CR1 deficiency leads to impairment of hippocampal cognitive function and synaptic plasticity. J Neurosci, 31: 16241-16250.
146. Sipe GO, Lowery RL, Tremblay ME, Kelly EA, Lamantia CE, Majewska AK. (2016) Microglial P2Y12 is necessary for synaptic plasticity in mouse visual cortex. Nat Commun, 7: 10905.
147. Feng D, Huang A, Yan W, Chen D. (2019) CD200 dysfunction in neuron contributes to synaptic deficits and cognitive impairment. Biochem Biophys Res Commun, 516: 1053-1059.
148. Sun H, He X, Tao X, Hou T, Chen M, He M, Liao H. (2020) The CD200/CD200R signaling pathway contributes to spontaneous functional recovery by enhancing synaptic plasticity after stroke. J Neuroinflammation, 17: 171.

149. Stellwagen D, Malenka RC. (2006) Synaptic scaling mediated by glial TNF-alpha. Nature, 440: 1054-1059.
150. Chen K, Zhang L, Tan M, Lai CS, Li A, Ren C, So KF. (2017) Treadmill exercise suppressed stress-induced dendritic spine elimination in mouse barrel cortex and improved working memory via BDNF/TrkB pathway. Transl Psychiatry, 7: e1069.
151. Saw G, Krishna K, Gupta N, Soong TW, Mallilankaraman K, Sajikumar S, Dheen ST. (2020) Epigenetic regulation of microglial phosphatidylinositol 3-kinase pathway involved in long-term potentiation and synaptic plasticity in rats. Glia, 68: 656-669.
152. Nguyen PT, Dorman LC, Pan S, Vainchtein ID, Han RT, Nakao-Inoue H, Taloma SE, Barron JJ, Molofsky AB, Kheirbek MA, Molofsky AV. (2020) Microglial Remodeling of the Extracellular Matrix Promotes Synapse Plasticity. Cell, 182: 388-403.e15.
153. Stowell RD, Sipe GO, Dawes RP, Batchelor HN, Lordy KA, Whitelaw BS, Stoessel MB, Bidlack JM, Brown E, Sur M, Majewska AK. (2019) Noradrenergic signaling in the wakeful state inhibits microglial surveillance and synaptic plasticity in the mouse visual cortex. Nat Neurosci, 22: 1782-1792.
154. Sarrazin JL, Bonneville F, Martin-Blondel G. (2012) Brain infections. Diagn Interv Imaging, 93: 473-490.
155. Wohleb ES. (2016) Neuron-Microglia Interactions in Mental Health Disorders: "For Better, and For Worse". Front Immunol, 7: 544.
156. Joe EH, Choi DJ, An J, Eun JH, Jou I, Park S. (2018) Astrocytes, Microglia, and Parkinson's Disease. Exp Neurobiol, 27: 77-87.
157. Perea JR, Llorens-Martin M, Avila J, Bolos M. (2018) The Role of Microglia in the Spread of Tau: Relevance for Tauopathies. Front Cell Neurosci, 12: 172.
158. Stephenson J, Nutma E, van der Valk P, Amor S. (2018) Inflammation in CNS neurodegenerative diseases. Immunology, 154 : 204-219.
159. Mitchell RH, Goldstein BI. (2014) Inflammation in children and adolescents with neuropsychiatric disorders: a systematic review. J Am Acad Child Adolesc Psychiatry, 53: 274-296.
160. Hohlfeld R, Kerschensteiner M, Meinl E. (2007) Dual role of inflammation in CNS disease. Neurology, 68: S58-S63.

161. Lucas S-M, Rothwell NJ, Gibson RM. (2006) The role of inflammation in CNS injury and disease. British Journal of Pharmacology, 147: S232-S240.
162. Block ML, Zecca L, Hong JS. (2007) Microglia-mediated neurotoxicity: uncovering the molecular mechanisms. Nat Rev Neurosci, 8: 57-69.
163. Glezer I, Simard AR, Rivest S. (2017) Neuroprotective role of the innate immune system by microglia. Neuroscience, 147: 867-883.
164. Kabba JA, Xu Y, Christian H, Ruan W, Chenai K, Xiang Y, Zhang L, Saavedra JM, Pang T. (2018) Microglia: Housekeeper of the Central Nervous System. Cell Mol Neurobiol, 38: 53-71.
165. Koss K, Churchward MA, Tsui C, Todd KG. (2019) In Vitro Priming and Hyper-Activation of Brain Microglia: an Assessment of Phenotypes. Mol Neurobiol, 56: 6409-6425.
166. Amici SA, Dong J, Guerau-de-Arellano M. (2017) Molecular Mechanisms Modulating the Phenotype of Macrophages and Microglia. Front Immunol, 8: 1520.
167. Norden DM, Muccigrosso MM, Godbout JP. (2015) Microglial priming and enhanced reactivity to secondary insult in aging, and traumatic CNS injury, and neurodegenerative disease. Neuropharmacology, 96: 29-41.
168. Cowan M, Petri WA, Jr. (2018) Microglia: Immune Regulators of Neurodevelopment. Front Immunol, 9: 2576.
169. Ozaki K, Kato D, Ikegami A, Hashimoto A, Sugio S, Guo Z, Shibushita M, Tatematsu T, Haruwaka K, Moorhouse AJ, Yamada H, Wake H. (2020) Maternal immune activation induces sustained changes in fetal microglia motility. Sci Rep, 10: 21378.
170. Wright-Jin EC, Gutmann DH. (2019) Microglia as Dynamic Cellular Mediators of Brain Function. Trends Mol Med, 25: 967-979.
171. Gerrits E, Heng Y, Boddeke E, Eggen BJL. (2020) Transcriptional profiling of microglia; current state of the art and future perspectives. Glia, 68: 740-755.
172. Olah M, Menon V, Habib N, Taga MF, Ma Y, Yung CJ, Cimpean M, Khairallah A, Coronas-Samano G, Sankowski R, Grun D, Kroshilina AA, Dionne D, Sarkis RA, Cosgrove GR, Helgager J, Golden JA, Pennell PB, Prinz M, Vonsattel JPG, Teich AF, Schneider JA, Bennett DA, Regev A, Elyaman W, Bradshaw EM, De Jager PL. (2020)

Single cell RNA sequencing of human microglia uncovers a subset associated with Alzheimer's disease. Nat Commun, 11: 6129.

173. Novikova G, Kapoor M, Tcw J, Abud EM, Efthymiou AG, Chen SX, Cheng H, Fullard JF, Bendl J, Liu Y, Roussos P, Bjorkegren JL, Liu Y, Poon WW, Hao K, Marcora E, Goate AM. (2021) Integration of Alzheimer's disease genetics and myeloid genomics identifies disease risk regulatory elements and genes. Nat Commun, 12: 1610.
174. Arnold T, Betsholtz C. (2013) The importance of microglia in the development of the vasculature in the central nervous system. Vasc Cell, 5: 4.
175. Dudvarski S N, Teodorczyk M, Ploen R, Zipp F, Schmidt MHH. (2016) Microglia-blood vessel interactions: a double-edged sword in brain pathologies. Acta Neuropathol, 131: 347-363.
176. Szalay G, Martinecz B, Lénárt N, Környei Z, Orsolits B, Judák L, Császár E, Fekete R, West BL, Katona G, Rózsa B, Dénes Á. (2016) Microglia protect against brain injury and their selective elimination dysregulates neuronal network activity after stroke. Nat Commun, 7: 11499.
177. Rymo SF, Gerhardt H, Wolfhagen Sand F, Lang R, Uv A, Betsholtz C. (2011) A two-way communication between microglial cells and angiogenic sprouts regulates angiogenesis in aortic ring cultures. PLoS One, 6: e15846.
178. Grossmann R, Stence N, Carr J, Fuller L, Waite M, Dailey ME. (2002) Juxtavascular microglia migrate along brain microvessels following activation during early postnatal development. Glia, 37: 229-240.
179. Mondo E, Becker SC, Kautzman AG, Schifferer M, Baer CE, Chen J, Huang EJ, Simons M, Schafer DP. (2020) A Developmental Analysis of Juxtavascular Microglia Dynamics and Interactions with the Vasculature. J Neurosci, 40: 6503-6521.
180. Checchin D, Sennlaub F, Levavasseur E, Leduc M, Chemtob S. (2006) Potential role of microglia in retinal blood vessel formation. Invest Ophthalmol Vis Sci, 47: 3595-3602.
181. Kubota Y, Takubo K, Shimizu T, Ohno H, Kishi K, Shibuya M, Saya H, Suda T. (2009) M-CSF inhibition selectively targets pathological angiogenesis and lymphangiogenesis. J Exp Med, 206: 1089-1102.

182. Fantin A, Vieira JM, Gestri G, Denti L, Schwarz Q, Prykhozhij S, Peri F, Wilson SW, Ruhrberg C. (2010) Tissue macrophages act as cellular chaperones for vascular anastomosis downstream of VEGF-mediated endothelial tip cell induction. Blood, 116: 829-840.
183. Carmeliet P, Ferreira V, Breier G, Pollefeyt S, Kieckens L, Gertsenstein M, Fahrig M, Vandenhoeck A, Harpal K, Eberhardt C, Declercq C, Pawling J, Moons L, Collen D, Risau W, Nagy A. (1996) Abnormal blood vessel development and lethality in embryos lacking a single VEGF allele. Nature, 380: 435-439.
184. Shalaby F, Rossant J, Yamaguchi TP, Gertsenstein M, Wu XF, Breitman ML, Schuh AC. (1995) Failure of blood-island formation and vasculogenesis in Flk-1-deficient mice. Nature, 376: 62-66.
185. Thurgur H, Pinteaux E. (2019) Microglia in the Neurovascular Unit: Blood-Brain Barrier-microglia Interactions After Central Nervous System Disorders. Neuroscience, 405: 55-67.
186. Davalos D, Ryu JK, Merlini M, Baeten KM, Le Moan N, Petersen MA, Deerinck TJ, Smirnoff DS, Bedard C, Hakozaki H, Gonias Murray S, Ling JB, Lassmann H, Degen JL, Ellisman MH, Akassoglou K. (2012) Fibrinogen-induced perivascular microglial clustering is required for the development of axonal damage in neuroinflammation. Nat Commun, 3: 1227.
187. Jolivel V, Bicker F, Biname F, Ploen R, Keller S, Gollan R, Jurek B, Birkenstock J, Poisa-Beiro L, Bruttger J, Opitz V, Thal SC, Waisman A, Bauerle T, Schafer MK, Zipp F, Schmidt MHH. (2015) Perivascular microglia promote blood vessel disintegration in the ischemic penumbra. Acta Neuropathol, 129: 279-295.
188. Lou N, Takano T, Pei Y, Xavier AL, Goldman SA, Nedergaard M. Purinergic receptor P2RY12-dependent microglial closure of the injured blood-brain barrier. Proc Natl Acad Sci U S A, 113: 1074-1079.
189. Jian L. K, Rosenberg GA. (2005) Matrix metalloproteinases and free radicals in cerebral ischemia. Free Radic Biol Med, 39: 71-80.
190. Yang YM, Shang DS, Zhao WD, Fang WG, Chen YH. (2013) Microglial TNF-alpha-dependent elevation of MHC class I expression on brain endothelium induced by

amyloid-beta promotes T cell transendothelial migration. Neurochem Res, 38: 2295-2304.

191. Denes A, Pinteaux E, Rothwell NJ, Allan SM. (2011) Interleukin-1 and stroke: biomarker, harbinger of damage, and therapeutic target. Cerebrovasc Dis, 32: 517-527.
192. Matsumoto J, Takata F, Machida T, Takahashi H, Soejima Y, Funakoshi M, Futagami K, Yamauchi A, Dohgu S, Kataoka Y. (2014) Tumor necrosis factor-alpha-stimulated brain pericytes possess a unique cytokine and chemokine release profile and enhance microglial activation. Neurosci Lett, 578: 133-138.
193. Summers L, Kangwantas K, Rodriguez-Grande B, Denes A, Penny J, Kielty C, Pinteaux E. (2013) Activation of brain endothelial cells by interleukin-1 is regulated by the extracellular matrix after acute brain injury. Mol Cell Neurosci, 57: 93-103.
194. Fiala M, Looney DJ, Stins M, Way DD, Zhang L, Gan X, Chiappelli F, Schweitzer ES, Shapshak P, Weinand M, Graves MC, Witte M, Kim KS. (1997) TNF-alpha opens a paracellular route for HIV-1 invasion across the blood-brain barrier. Mol Med, 3: 553-564.
195. Nishioku T, Matsumoto J, Dohgu S, Sumi N, Miyao K, Takata F, Shuto H, Yamauchi A, Kataoka Y. (2010) Tumor necrosis factor-alpha mediates the blood-brain barrier dysfunction induced by activated microglia in mouse brain microvascular endothelial cells. J Pharmacol Sci, 112: 251-254.
196. Asahina M, Yoshiyama Y, Hattori T. (2001) Expression of matrix metalloproteinase-9 and urinary-type plasminogen activator in Alzheimer's disease brain. Clin Neuropathol, 20: 60-63.
197. Nijaguna MB, Patil V, Urbach S, Shwetha SD, Sravani K, Hegde AS, Chandramouli BA, Arivazhagan A, Marin P, Santosh V, Somasundaram K. (2015) Glioblastoma-derived Macrophage Colony-stimulating Factor (MCSF) Induces Microglial Release of Insulin-like Growth Factor-binding Protein 1 (IGFBP1) to Promote Angiogenesis. J Biol Chem, 290: 23401-23415.
198. Salmeron K, Aihara T, Redondo-Castro E, Pinteaux E, Bix G. (2016) IL-1alpha induces angiogenesis in brain endothelial cells in vitro: implications for brain angiogenesis after acute injury. J Neurochem, 136: 573-580.

199. Lee JY, Choi HY, Yune TY. (2015) MMP-3 secreted from endothelial cells of blood vessels after spinal cord injury activates microglia, leading to oligodendrocyte cell death. Neurobiol Dis, 82: 141-151.
200. Tarozzo G, Campanella M, Ghiani M, Bulfone A, Beltramo M. (2002) Expression of fractalkine and its receptor, CX3CR1, in response to ischaemia-reperfusion brain injury in the rat. Eur J Neurosci, 15: 1663-1668.
201. Pankratova S, Bjornsdottir H, Christensen C, Zhang L, Li S, Dmytriyeva O, Bock E, Berezin V. (2016) Immunomodulator CD200 Promotes Neurotrophic Activity by Interacting with and Activating the Fibroblast Growth Factor Receptor. Mol Neurobiol, 53: 584-594.
202. Ryu JK, Cho T, Choi HB, Wang YT, McLarnon JG. (2009) Microglial VEGF receptor response is an integral chemotactic component in Alzheimer's disease pathology. J Neurosci, 29: 3-13.
203. Milner R, Crocker SJ, Hung S, Wang X, Frausto RF, del Zoppo GJ. (2007) Fibronectin- and vitronectin-induced microglial activation and matrix metalloproteinase-9 expression is mediated by integrins alpha5beta1 and alphavbeta5. J Immunol, 178: 8158-8167.
204. Dana H, Chen TW, Hu A, Shields BC, Guo C, Looger LL, Kim DS, Svoboda K. (2014) Thy1-GCaMP6 transgenic mice for neuronal population imaging in vivo. PLoS One, 9: e108697.
205. Yona S, Kim KW, Wolf Y, Mildner A, Varol D, Breker M, Strauss-Ayali D, Viukov S, Guilliams M, Misharin A, Hume DA, Perlman H, Malissen B, Zelzer E, Jung S. (2013) Fate mapping reveals origins and dynamics of monocytes and tissue macrophages under homeostasis. Immunity, 38: 79-91.
206. Zhu H, Aryal DK, Olsen RH, Urban DJ, Swearingen A, Forbes S, Roth BL, Hochgeschwender U. (2016) Cre-dependent DREADD (Designer Receptors Exclusively Activated by Designer Drugs) mice. Genesis, 54: 439-446.
207. Gee JM, Smith NA, Fernandez FR, Economo MN, Brunert D, Rothermel M, Morris SC, Talbot A, Palumbos S, Ichida JM, Shepherd JD, West PJ, Wachowiak M, Capecchi MR, Wilcox KS, White JA, Tvrdik P. (2014) Imaging activity in neurons and glia with a

Polr2a-based and cre-dependent GCaMP5G-IRES-tdTomato reporter mouse. Neuron, 83: 1058-1072.

208. Alexander GM, Rogan SC, Abbas AI, Armbruster BN, Pei Y, Allen JA, Nonneman RJ, Hartmann J, Moy SS, Nicolelis MA, McNamara JO, Roth BL. (2009) Remote control of neuronal activity in transgenic mice expressing evolved G protein-coupled receptors. Neuron, 63: 27-39.
209. Császár E, Lénárt N, Cserép C, Környei Z, Fekete R, Pósfai B, Balázsfi D, Hangya B, Schwarcz AD, Szabadits E, Szöllősi D, Szigeti K, Máthé D, West BL, Sviatkó K, Bras AR, Mariani JC, Kliewer A, Lenkei Z, Hricisák L, Benyó Z, Baranyi M, Sperlágh B, Menyhárt Á, Farkas E, Dénes Á. (2022) Microglia modulate blood flow, neurovascular coupling, and hypoperfusion via purinergic actions. J Exp Med, 219: e20211071.
210. Ridder DA, Lang MF, Salinin S, Roderer JP, Struss M, Maser-Gluth C, Schwaninger M. (2011) TAK1 in brain endothelial cells mediates fever and lethargy. Journal of Experimental Medicine, 208: 2615-2623.
211. Wong R, Lénárt N, Hill L, Toms L, Coutts G, Martinecz B, Császár E, Nyiri G, Papaemmanouil A, Waisman A, Müller W, Schwaninger M, Rothwell N, Francis S, Pinteaux E, Denés A, Allan SM. (2019) Interleukin-1 mediates ischaemic brain injury via distinct actions on endothelial cells and cholinergic neurons. Brain Behav Immun, 76: 126-138.
212. Lecrux C, Sandoe CH, Neupane S, Kropf P, Toussay X, Tong XK, Lacalle-Aurioles M, Shmuel A, Hamel E. (2017) Impact of Altered Cholinergic Tones on the Neurovascular Coupling Response to Whisker Stimulation. J Neurosci, 37: 1518-1531.
213. Tai YF, Piccini P. (2004) Applications of positron emission tomography (PET) in neurology. J Neurol Neurosurg Psychiatry, 75: 669-676.
214. Apostolova I, Wunder A, Dirnagl U, Michel R, Stemmer N, Lukas M, Derlin T, Gregor-Mamoudou B, Goldschmidt J, Brenner W, Buchert R. (2012) Brain perfusion SPECT in the mouse: normal pattern according to gender and age. Neuroimage, 63: 1807-1817.
215. Tiran E, Ferrier J, Deffieux T, Gennisson JL, Pezet S, Lenkei Z, Tanter M. (2017) Transcranial Functional Ultrasound Imaging in Freely Moving Awake Mice and Anesthetized Young Rats without Contrast Agent. Ultrasound Med Biol, 43: 1679-1689.

216. Demene C, Deffieux T, Pernot M, Osmanski BF, Biran V, Gennisson JL, Sieu LA, Bergel A, Franqui S, Correas JM, Cohen I, Baud O, Tanter M. (2015) Spatiotemporal Clutter Filtering of Ultrafast Ultrasound Data Highly Increases Doppler and fUltrasound Sensitivity. Ieee T Med Imaging, 34: 2271-2285.
217. Ferrier J, Tiran E, Deffieux T, Tanter M, Lenkei Z. (2020) Functional imaging evidence for task-induced deactivation and disconnection of a major default mode network hub in the mouse brain. P Natl Acad Sci USA, 117: 15270-15280.
218. Rabut C, Ferrier J, Bertolo A, Osmanski B, Mousset X, Pezet S, Deffieux T, Lenkei Z, Tanter M. (2020) Pharmaco-fUS: Quantification of pharmacologically-induced dynamic changes in brain perfusion and connectivity by functional ultrasound imaging in awake mice. Neuroimage, 222: 117231.
219. Kvitsiani D, Ranade S, Hangya B, Taniguchi H, Huang JZ, Kepecs A. (2013) Distinct behavioural and network correlates of two interneuron types in prefrontal cortex. Nature, 498: 363-366.
220. Siegle JH, Lopez AC, Patel YA, Abramov K, Ohayon S, Voigts J. (2017) Open Ephys: an open-source, plugin-based platform for multichannel electrophysiology. J Neural Eng, 14: 045003.
221. Schmitzer-Torbert N, Jackson J, Henze D, Harris K, Redish AD. (2005) Quantitative measures of cluster quality for use in extracellular recordings. Neuroscience, 131: 1-11.
222. Garthwaite J, Garthwaite G, Palmer RM, Moncada S. (1989) NMDA receptor activation induces nitric oxide synthesis from arginine in rat brain slices. Eur J Pharmacol, 172: 413-416.
223. Voipio J, Kaila K. (1993) Interstitial PCO2 and pH in rat hippocampal slices measured by means of a novel fast CO2/H(+)-sensitive microelectrode based on a PVC-gelled membrane. Pflugers Arch, 423: 193-201.
224. Faraco G, Sugiyama Y, Lane D, Garcia-Bonilla L, Chang H, Santisteban MM, Racchumi G, Murphy M, Van Rooijen N, Anrather J, Iadecola C. (2016) Perivascular macrophages mediate the neurovascular and cognitive dysfunction associated with hypertension. J Clin Invest, 126: 4674-4689.

225. Wong R, Gibson CL, Kendall DA, Bath PM. (2014) Evaluating the translational potential of progesterone treatment following transient cerebral ischaemia in male mice. BMC Neurosci, 15: 131.
226. Dunn AK. (2012) Laser speckle contrast imaging of cerebral blood flow. Ann Biomed Eng, 40: 367-377.
227. Eriksson S, Nilsson J, Sturesson C. (2014) Non-invasive imaging of microcirculation: a technology review. Med Devices (Auckl), 7: 445-452.
228. Deli MA, Abraham CS, Niwa M, Falus A. (2003) N,N-diethyl-2-[4-(phenylmethyl)phenoxy]ethanamine increases the permeability of primary mouse cerebral endothelial cell monolayers. Inflamm Res, 52 Suppl 1: S39-40.
229. Lenart N, Walter FR, Bocsik A, Santha P, Toth ME, Harazin A, Toth AE, Vizler C, Torok Z, Pilbat AM, Vigh L, Puskas LG, Santha M, Deli MA. (2015) Cultured cells of the blood-brain barrier from apolipoprotein B-100 transgenic mice: effects of oxidized low-density lipoprotein treatment. Fluids Barriers CNS, 12: 17.
230. Perriere N, Demeuse P, Garcia E, Regina A, Debray M, Andreux JP, Couvreur P, Scherrmann JM, Temsamani J, Couraud PO, Deli MA, Roux F. (2005) Puromycin-based purification of rat brain capillary endothelial cell cultures. Effect on the expression of blood-brain barrier-specific properties. J Neurochem, 93: 279-289.
231. Perriere N, Yousif S, Cazaubon S, Chaverot N, Bourasset F, Cisternino S, Decleves X, Hori S, Terasaki T, Deli M, Scherrmann JM, Temsamani J, Roux F, Couraud PO. (2007) A functional in vitro model of rat blood-brain barrier for molecular analysis of efflux transporters. Brain Res, 1150: 1-13.
232. Környei Z, Szlavik V, Szabo B, Gocza E, Czirok A, Madarasz E. (2005) Humoral and contact interactions in astroglia/stem cell co-cultures in the course of glia-induced neurogenesis. Glia, 49: 430-444.
233. Saura J, Tusell JM, Serratosa J. (2003) High-yield isolation of murine microglia by mild trypsinization. Glia, 44: 183-189.
234. Michl J, Park KC, Swietach P. (2019) Evidence-based guidelines for controlling pH in mammalian live-cell culture systems. Communications biology, 2: 144.

235. Lowry OH, Rosebrough NJ, Farr AL, Randall RJ. (1951) Protein measurement with the Folin phenol reagent. J Biol Chem, 193: 265-275.
236. Baranyi M, Milusheva E, Vizi ES, Sperlagh B. (2006) Chromatographic analysis of dopamine metabolism in a Parkinsonian model. J Chromatogr A, 1120: 13-20.
237. Kremer JR, Mastronarde DN, McIntosh JR. (1996) Computer visualization of three-dimensional image data using IMOD. J Struct Biol, 116: 71-76.
238. Heindl S, Gesierich B, Benakis C, Llovera G, Duering M, Liesz A. (2018) Automated Morphological Analysis of Microglia After Stroke. Front Cell Neurosci, 12: 106.
239. Cserép C, Pósfai B, Lénárt N, Fekete R, László ZI, Lele Z, Orsolits B, Molnár G, Heindl S, Schwarcz AD, Ujvári K, Környei Z, Tóth K, Szabadits E, Sperlágh B, Baranyi M, Csiba L, Hortobágyi T, Maglóczky Z, Martinecz B, Szabó G, Erdélyi F, Szipőcs R, Tamkun MM, Gesierich B, Duering M, Katona I, Liesz A, Tamás G, Dénes Á. (2020) Microglia monitor and protect neuronal function through specialized somatic purinergic junctions. Science, 367: 528-537.
240. Fekete R, Cserép C, Lénárt N, Tóth K, Orsolits B, Martinecz B, Méhes E, Szabó B, Németh V, Gönci B, Sperlágh B, Boldogkői Z, Kittel Á, Baranyi M, Ferenczi S, Kovács K, Szalay G, Rózsa B, Webb C, Kovacs GG, Hortobágyi T, West BL, Környei Z, Dénes Á. (2018) Microglia control the spread of neurotropic virus infection via P2Y12 signalling and recruit monocytes through P2Y12-independent mechanisms. Acta Neuropathologica, 136: 461-482.
241. Haynes SE, Hollopeter G, Yang G, Kurpius D, Dailey ME, Gan WB, Julius D. (2006) The P2Y12 receptor regulates microglial activation by extracellular nucleotides. Nat Neurosci, 9: 1512-1519.
242. Lohman AW, Billaud M, Isakson BE. (2012) Mechanisms of ATP release and signalling in the blood vessel wall. Cardiovasc Res, 95: 269-280.
243. Elmore MRP, Najafi AR, Koike MA, Dagher NN, Spangenberg EE, Rice RA, Kitazawa M, Matusow B, Nguyen H, West BL, Green KN. (2014) Colony-Stimulating Factor 1 Receptor Signaling Is Necessary for Microglia Viability, Unmasking a Microglia Progenitor Cell in the Adult Brain. Neuron, 82: 380-397.

244. Tarantini S, Valcarcel-Ares NM, Yabluchanskiy A, Fulop GA, Hertelendy P, Gautam T, Farkas E, Perz A, Rabinovitch PS, Sonntag WE, Csiszar A, Ungvari Z. (2018) Treatment with the mitochondrial-targeted antioxidant peptide SS-31 rescues neurovascular coupling responses and cerebrovascular endothelial function and improves cognition in aged mice. Aging Cell, 17: e12731.
245. Mace E, Montaldo G, Cohen I, Baulac M, Fink M, Tanter M. (2011) Functional ultrasound imaging of the brain. Nat Methods, 8: 662-664.
246. Thompson KJ, Khajehali E, Bradley SJ, Navarrete JS, Huang XP, Slocum S, Jin J, Liu J, Xiong Y, Olsen RHJ, Diberto JF, Boyt KM, Pina MM, Pati D, Molloy C, Bundgaard C, Sexton PM, Kash TL, Krashes MJ, Christopoulos A, Roth BL, Tobin AB. (2018) DREADD Agonist 21 Is an Effective Agonist for Muscarinic-Based DREADDs in Vitro and in Vivo. Acs Pharmacol Transl, 1: 61-72.
247. Meng L, Gelb AW. (2015) Regulation of cerebral autoregulation by carbon dioxide. Anesthesiology, 122: 196-205.
248. Hamilton NB, Attwell D, Hall CN. (2010) Pericyte-mediated regulation of capillary diameter: a component of neurovascular coupling in health and disease. Front Neuroenergetics 2: 5.
249. Janssen BJ, De Celle T, Debets JJ, Brouns AE, Callahan MF, Smith TL. (2004) Effects of anesthetics on systemic hemodynamics in mice. Am J Physiol Heart Circ Physiol, 287: H1618-1624.
250. Pal E, Hricisak L, Lekai A, Nagy D, Fulop A, Erben RG, Varbiro S, Sandor P, Benyo Z. (2020) Ablation of Vitamin D Signaling Compromises Cerebrovascular Adaptation to Carotid Artery Occlusion in Mice. Cells, 9: 1457.
251. Toda N, Ayajiki K, Okamura T. (2009) Cerebral blood flow regulation by nitric oxide: recent advances. Pharmacol Rev, 61: 62-97.
252. Smyth LCD, Rustenhoven J, Scotter EL, Schweder P, Faull RLM, Park TIH, Dragunow M. (2018) Markers for human brain pericytes and smooth muscle cells. J Chem Neuroanat, 92: 48-60.

253. Wolters FJ, Zonneveld HI, Hofman A, van der Lugt A, Koudstaal PJ, Vernooij MW, Ikram MA. (2017) Cerebral Perfusion and the Risk of Dementia: A Population-Based Study. Circulation, 136: 719-728.
254. Masuda T, Croom D, Hida H, Kirov SA. (2011) Capillary blood flow around microglial somata determines dynamics of microglial processes in ischemic conditions. Glia, 59: 1744-1753.
255. Nishijima Y, Akamatsu Y, Yang SY, Lee CC, Baran U, Song SZ, Wang RK, Tominaga T, Liu JL. (2016) Impaired Collateral Flow Compensation During Chronic Cerebral Hypoperfusion in the Type 2 Diabetic Mice. Stroke, 47: 3014-3021.
256. Konsman JP, Vigues S, Mackerlova L, Bristow A, Blomqvist A. (2004) Rat brain vascular distribution of interleukin-1 type-1 receptor immunoreactivity: relationship to patterns of inducible cyclooxygenase expression by peripheral inflammatory stimuli. J Comp Neurol, 472: 113-129.
257. Banwell V, Sena ES, Macleod MR. (2009) Systematic review and stratified meta-analysis of the efficacy of interleukin-1 receptor antagonist in animal models of stroke. J Stroke Cerebrovasc Dis, 18: 269-276.
258. Maysami S, Wong R, Pradillo JM, Denes A, Dhungana H, Malm T, Koistinaho J, Orset C, Rahman M, Rubio M, Schwaninger M, Vivien D, Bath PM, Rothwell NJ, Allan SM. (2016) A cross-laboratory preclinical study on the effectiveness of interleukin-1 receptor antagonist in stroke. J Cereb Blood Flow Metab, 36: 596-605.
259. Relton JK, Rothwell NJ. (1992) Interleukin-1 receptor antagonist inhibits ischaemic and excitotoxic neuronal damage in the rat. Brain Res Bull, 29: 243-246.
260. Engelhardt B, Sorokin L. (2009) The blood-brain and the blood-cerebrospinal fluid barriers: function and dysfunction. Semin Immunopathol, 31: 497-511.
261. Gómez M. A, Besson VC, Lerouet D. (2021) Microglia and Neuroinflammation: What Place for P2RY12? Int J Mol Sci, 22: 1636.
262. Bisht K, Okojie KA, Sharma K, Lentferink DH, Sun YY, Chen HR, Uweru JO, Amancherla S, Calcuttawala Z, Campos-Salazar AB, Corliss B, Jabbour L, Benderoth J, Friestad B, Mills WA, Isakson BE, Tremblay ME, Kuan CY, Eyo UB. (2021) Capillary-

associated microglia regulate vascular structure and function through PANX1-P2RY12 coupling in mice. Nature Communications, 12: 5289.

263. Jin Y, Sato K, Tobo A, Mogi C, Tobo M, Murata N, Ishii S, Im DS, Okajima F. (2014) Inhibition of interleukin-1 beta production by extracellular acidification through the TDAG8/cAMP pathway in mouse microglia. Journal of Neurochemistry, 129: 683-695.
264. Langfelder A, Okonji E, Deca D, Wei WC, Glitsch MD. (2015) Extracellular acidosis impairs P2Y receptor-mediated Ca2+ signalling and migration of microglia. Cell Calcium, 57: 247-256.
265. Szabadits E, Cserép C, Szőnyi A, Fukazawa Y, Shigemoto R, Watanabe M, Itohara S, Freund TF, Nyiri G. (2011) NMDA Receptors in Hippocampal GABAergic Synapses and Their Role in Nitric Oxide Signaling. Journal of Neuroscience, 31: 5893-5904.
266. Heinert G, Nye PC, Paterson DJ. (1999) Nitric oxide and prostaglandin pathways interact in the regulation of hypercapnic cerebral vasodilatation. Acta Physiol Scand, 166: 183-193.
267. Colonna M, Butovsky O. (2017) Microglia Function in the Central Nervous System During Health and Neurodegeneration. Annu Rev Immunol, 35: 441-468.
268. Zaharchuk G, Mandeville JB, Bogdanov AA, Jr., Weissleder R, Rosen BR, Marota JJ. (1999) Cerebrovascular dynamics of autoregulation and hypoperfusion. An MRI study of CBF and changes in total and microvascular cerebral blood volume during hemorrhagic hypotension. Stroke, 30: 2197-2205.
269. Halder SK, Milner R. (2019) A critical role for microglia in maintaining vascular integrity in the hypoxic spinal cord. Proc Natl Acad Sci U S A, 116: 26029-26037.
270. Umpierre AD, Bystrom LL, Ying Y, Liu YU, Worrell G, Wu LJ. (2020) Microglial calcium signaling is attuned to neuronal activity in awake mice. eLife, 9 :e56502.
271. Basu A, Krady JK, Levison SW. (2004) Interleukin-1: A master regulator of neuroinflammation. J Neurosci Res, 78: 151-156.
272. Slupe AM, Kirsch JR. (2018) Effects of anesthesia on cerebral blood flow, metabolism, and neuroprotection. J Cereb Blood Flow Metab, 38: 2192-2208.
273. Bernier LP, Brunner C, Cottarelli A, Balbi M. (2021) Location Matters: Navigating Regional Heterogeneity of the Neurovascular Unit. Front Cell Neurosci, 15: 696540.

274. Garry PS, Ezra M, Rowland MJ, Westbrook J, Pattinson KT. (2015) The role of the nitric oxide pathway in brain injury and its treatment--from bench to bedside. Exp Neurol, 263: 235-243.
275. Kleinberger G, Brendel M, Mracsko E, Wefers B, Groeneweg L, Xiang XY, Focke C, Deussing M, Suarez-Calvet M, Mazaheri F, Parhizkar S, Pettkus N, Wurst W, Feederle R, Bartenstein P, Mueggler T, Arzberger T, Knuesel I, Rominger A, Haass C. (2017) The FTD-like syndrome causing TREM2 T66M mutation impairs microglia function, brain perfusion, and glucose metabolism. Embo J, 36: 1837-1853.
276. Kloner RA, King KS, Harrington MG. (2018) No-reflow phenomenon in the heart and brain. Am J Physiol-Heart C, 315: H550-H562.
277. Eyo U, Dailey ME. (2012) Effects of oxygen-glucose deprivation on microglial mobility and viability in developing mouse hippocampal tissues. Glia, 60: 1747-1760.

DOI:10.14753/SE.2023.2742

10. Bibliography of the candidate's publications

Publications related to this thesis:

Császár E*, Lénárt N*, Cserép C, Környei Z, Fekete R, Pósfai B, Balázsfi D, Hangya B, Schwarcz AD, Szabadits E, Szöllősi D, Szigeti K, Máthé D, West BL, Sviatkó K, Bras AR, Mariani JC, Kliewer A, Lenkei Z, Hricisák L, Benyó Z, Baranyi M, Sperlágh B, Menyhárt Á, Farkas E, Dénes Á. (2022) Microglia modulate blood flow, neurovascular coupling, and hypoperfusion via purinergic actions. J Exp Med, 219: e20211071.
IF: 14,307

Wong R, Lénárt N, Hill L, Toms L, Coutts G, Martinecz B, **Császár E**, Nyiri G, Papaemmanouil A, Waisman A, Müller W, Schwaninger M, Rothwell N, Francis S, Pinteaux E, Denés A, Allan SM. (2019) Interleukin-1 mediates ischaemic brain injury via distinct actions on endothelial cells and cholinergic neurons. Brain Behav Immun, 76: 126-138.
IF: 6,633

Other publications:

Varga DP, Menyhárt Á, Pósfai B, **Császár E**, Lénárt N, Cserép C, Orsolits B, Martinecz B, Szlepák T, Bari F, Farkas E, Dénes Á. (2020) Microglia alter the threshold of spreading depolarization and related potassium uptake in the mouse brain. J Cereb Blood Flow Metab, 40: S67-S80
IF: 5,68

Orsini F, Fumagalli S, **Császár E**, Tóth K, De Blasio D, Zangari R, Lénárt N, Dénes Á, De Simoni MG. (2018) Mannose-Binding Lectin Drives Platelet Inflammatory Phenotype and Vascular Damage After Cerebral Ischemia in Mice via IL (Interleukin)-1alpha. Arterioscler Thromb Vasc Biol, 38: 2678-2690.
IF: 8,31

DOI:10.14753/SE.2023.2742

Szalay G, Martinecz B, Lénárt N, Környei Z, Orsolits B, Judák L, **Császár E**, Fekete R, West BL, Katona G, Rózsa B, Dénes Á. (2016) Microglia protect against brain injury and their selective elimination dysregulates neuronal network activity after stroke. Nat Commun, 7: 11499.

IF: 14,91

DOI:10.14753/SE.2023.2742

11. Acknowledgements

First of all, I would like to express my sincere gratitude to my supervisor Ádám Dénes for his invaluable supervision, endless support and patience during my PhD study. I could not have imagined a better and friendlier supervisor.

I am also very grateful to Nikolett Lénárt, who supported me under any circumstances and helped me a lot in whatever she could.

I would also like to thank the help all of my colleagues in the laboratory and all of the collaborators, whom without this complex and precious study could not have been completed.

I am especially grateful to my mother and grandmother for all of the sacrifices that they have made on my behalf.

Last, but not least, I would like to thank my boyfriend, Csaba Ferenczi, and my friends for always being there for me in my hard times as well and having enough patient for me even when I was extremely grumpy and stressful and pushing me to finish this thesis.